Angle-dependent magnetoresistance in epitaxially strain-engineered thin films

Burema, Arjan

IMPORTANT NOTE: You are advised to consult the publisher's version (publisher's PDF) if you wish to cite from it. Please check the document version below.

Document Version
Publisher's PDF, also known as Version of record

Publication date:
2021

[Link to publication in University of Groningen/UMCG research database](#)

Angle-dependent magnetoresistance in epitaxially strain-engineered thin films

Arjan Auke Burema

Book cover: The cover displays a set of oscillating lines changing color from blue to red. In the context of this thesis it is an artist impression of the changing angle-dependent magnetoresistance with temperature as shown in chapter 5 of this thesis. The image and its rights were purchased from Shutterstock.

Angle-dependent magnetoresistance in epitaxially strain-engineered thin films

PhD thesis

to obtain the degree of PhD at the
University of Groningen
on the authority of the
Rector Magnificus Prof. C. Wijmenga
and in accordance with
the decision by the College of Deans.

This thesis will be defended in public on

Friday 26 November 2021 at 9.00 hours

by

Arjan Auke Burema

born on 17 March 1994
in Hoogeveen

Supervisors
 Prof. T. Banerjee
 Prof. M.V. Mostovoy

Assessment Committee
 Prof. J. Santamaria Sánchez-Barriga
 Prof. A.J.H.M. Rijnders
 Prof. B.J. van Wees

Contents

Chapter 1

Introduction

1.1 Magnetic materials and thin films

Magnetic materials have something magical about them, the attractive and repulsive force between two magnets is on one hand almost tangible yet on the other hand elusive. Mentions of magnets and magnetism dates back well over 2000 years[1–3]. Practical applications remained limited, with references suggesting describing the use of floating lodestone as a compass dating back to the 2nd century BC[3–5].

Nearly 2 millennia later, in 1600, William Gilbert published a book "De Magnete, Magneticisque Corporibus, et de Magno Magnete Tellure"[6] (On the Magnet and Magnetic Bodies, and the Great Magnet the Earth) describing the first systematic experiments with magnets leading to the conclusion that the earth itself was a big magnet with an iron core.

The next big discovery would be the discovery of a connection between current and magnetism in 1820[7, 8], by Hans Ørstat (Oersted). In his electromagnetic experiment, Ørstat sent a current through a wire and observed a deflection of a compass needle standing near the wire. The discovery of the connection between magnetism and electricity kickstarted a technological and scientific revolution. Roughly 40 years later, the theoretical understanding of the coupling between current and magnetism was given by James C. Maxwell[9, 10] leading to the present-day quantum mechanical understanding of magnetism[11].

Nowadays, various applications ranging from inductive cooking to data storage utilize the connection between magnetism and current. Improving existing devices or developing technical solutions, is a continuous quest driven by human curiosity, as well as a desire to improve the quality of life.

A prominent field that saw tremendous growth in the past two decades is spintronics. It has shown potential by developing novel devices such as magnetic random access memory, magnetoresistive read/write heads, and various other novel sensors. This resulted in an increased interest in the coupling between magnetism, or more fundamentally spin and current. One of the aims, in the field of spintronics,

is to develop spin-based electronics (spintronics). Such spintronic devices aim to be an alternative for current electronic devices, promising to be faster or more energy-efficient.

The most important magnetotransport phenomena playing a role in the development of these devices are the colossal magnetoresistance, giant magnetoresistance, tunneling magnetoresistance, and anisotropic magnetoresistance, showing the importance of understanding and influencing magnetism in an applicable manner.

In particular, the discovery of colossal magnetoresistance in perovskite manganites[12, 13], led to scientific interest to investigate the coupled magnetic and electronic transport properties of manganites[14]. The phenomenon, in essence, is a decrease in resistance when a magnetic field is applied.

To influence magnetotransport properties, like the colossal magnetoresistance[13, 15, 16], the effect of altering composition/ stoichometry[17–19], film thickness[20–23], strain[24–27], and interface effects[28, 29] can be studied. Tuning physical parameters can result in an increased magnitude of the magnetoresistance effect, or result in a lower current/voltage required to observe a specific effect, which can lead to various improvements, e.g. decrease power use/size or increase sensitivity.

1.2 Skyrmions

Our aim in this big picture was to find skyrmions, in complex oxide materials like $La_{1-x}Sr_xMnO_3$ or $SrFeO_3$. Due to a skyrmion's small size and (in theory) low energy consumption, they are good candidates for improving future data storage[30, 31] or developing spintronic devices, like a skyrmion racetrack memory[32, 33].

A skyrmion is a topologically protected noncolinear magnetic nanometer sized quasi-particle, or simpler put, the smallest (stable) magnetic domain possible with an opposite orientation as its surrounding. On top of this, the magnetic domain has an odd topological winding number, resulting in an energy barrier for destroying the skyrmion. The winding of the noncollinear spins results in a topological protection, making skyrmions stable quasi-particles under the right conditions. Figure 1.1 shows the spin orientation in a skyrmion. Notice the single spin in the middle pointing down and the continuous (counterclockwise) rotation of the spins. The spins make full 360° rotation when traversing the skyrmion from edge to edge, this full rotation is the topological protection, as in a physical system it requires energy to break the continuous chain of rotating spins and align all spins parallel.
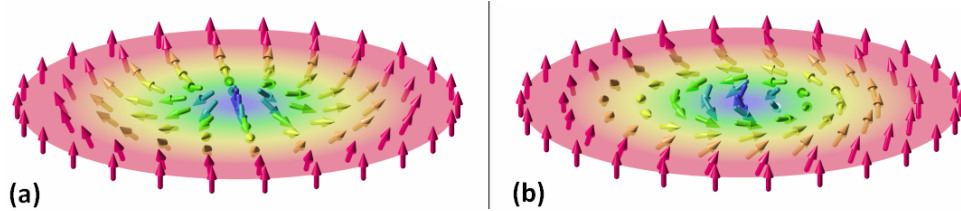
Figure 1.1: *Spins of a ferromagnetic layer forming a (a) Néel skyrmion (b) Bloch skyrmion. Taken from Karin Everschor-Sitte and Matthias Sitte[34] under the creative commons BY-SA 3.0 license.*

Magnetic skyrmions are, among others, found in materials which exhibit spiral magnetism due to chiral symmetry breaking in the crystal structure[35–37], the Dzyaloshinskii–Moriya interaction (DMI)[38–42], or competing exchange interactions[39, 43–46]. In thin films, there is already a natural broken inversion symmetry in the out-of-plane direction (z-axis), giving a natural advantage compared to bulk materials to study, create and manipulate magnetic skyrmions.

Due to this natural advantage, very thin films up to several monolayers are extensively studied by surface sensitive methods like Lorentz transmission microscopy (LTEM)[47], magneto-optic Kerr effect (MOKE) microscopy[48, 49] and spin polarized scanning tunneling microscopy (sp-STM)[40–42]. These experiments give insight into the balance of energy terms needed for the creation, annihilation, and stabilization of skyrmions. This also led to the famous blowing magnetic bubbles movie based on MOKE images in 2015[48].

Based on the existing work at the time, venturing out to find skyrmions in different (thicker) thin film materials was a method to improve the understanding of skyrmions and/or the materials. A complicating factor of thicker films is the presence of magnetic stray fields at the interface, both interface DMI and stray fields play a role in the stabilization and creation of skyrmions[38].

Obvious candidates, in our field of expertise, are complex oxides as they contain a wide range of desirable material properties and can be doped[44], stacked with other complex oxides[39, 50], or strained to observe skyrmions. Of the complex oxide family, we picked $La_{0.67}Sr_{0.33}MnO_3$ (LSMO), as we believe that tailoring the right magnetic environment will result in the observation of skyrmions in thin films of $La_{0.67}Sr_{0.33}MnO_3$. As for thin films, the observation of skyrmions is often in materials with a magnetic out-of-plane anisotropy[38], therefore our goal is to create and observe a magnetic out-of-plane anisotropy in $La_{0.67}Sr_{0.33}MnO_3$.

To observe the out-of-plane and inplane anisotropy, we used pure magnetic

methods and magnetotransport which is based on the negative magnetoresistance. The latter utilizes the knowledge that spins are aligned easier along a magnetic easy axis, resulting in a lower resistance. Hence, when we measure the resistance, while a magnetic field is rotated around the sample, the lowest resistance will indicate a preferential magnetization direction, see figure 1.2. Besides the angle dependent magnetoresitance effect between current and magnetism, our crystalline samples also have an angle dependent effect between the crystallographic orientation and magnetic field. See section 2.3.1 for a more in-depth discussion.
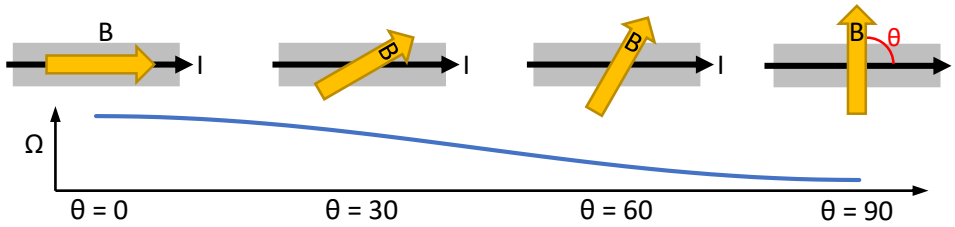
Figure 1.2: *Manganite crystal (grey) with rotating magnetic field starting in the in-plane direction (left) and ending out-of-plane direction (right). Below the figures, the angle θ between the current and the magnetic field as well as the resistance is indicated, as observed for compressively strained $La_{0.67}Sr_{0.33}MnO_3$ at low temperatures.*

In this thesis, we have investigated thin films of $La_{0.67}Sr_{0.33}MnO_3$ on two different substrates $LaAlO_3$ and $SrTiO_3$. By tuning parameters like strain, thickness, temperature, and applied magnetic field we investigated the anisotropy changes in $La_{0.67}Sr_{0.33}MnO_3$ with the described angle-dependent magnetotransport method. As described this out-of-plane anisotropy is desired for the creation and observation of skyrmions. Creating skyrmions without the presence of a heavy metal layer to induce spin-orbit coupling or utilizing other texturing to achieve stable skyrmions, has been challenging in a thin film. Some reports have found signs of skyrmions or magnetic bubbles in thin films like strained $SrRuO_3$[51] or PdIr[40].Since the Curie temperatures of such magnetic materials are not high enough to create stable skyrmions at room temperature, we chose to work with LSMO that does have a bulk Curie temperature above room temperature.

Using pulsed laser deposition, we grew compressively strained thin films of LSMO on $LaAlO_3$ with different thicknesses, to explore the optimum thickness for observing magnetocrystalline effects in the magnetotransport. After determining the optimum thickness, we varied the applied strain to observe the effect on the out-of-plane anisotropy in LSMO.

The films with the strongest out-of-plane anisotropy were used to measure the Hall effect by sweeping the magnetic field. We expected to observe signs of non-collinear textures like skyrmions or magnetic bubbles, by measuring the topological Hall effect, unfortunately, due to the film's high resistivity, no clear topological Hall effect signal was observed. For future measurements, growing a thicker film of LSMO on a substrate with smaller inplane lattice parameters e.g. $YAlO_3$ or $SrLaAlO_3$ would be a good starting option. This is because the increased compressive strain would allow for a thicker film with similar out-of-plane strain as used in our experiments. Balancing strain and thickness is vital to obtain a LSMO film which is both metallic and has an out-of-plane anisotropy. Combining these two properties in a thin film would hopefully show a topological Hall effect, signaling the presence of noncollinear textures like skyrmions.

1.3 Valorization

LSMO

LSMO has already been studied for a long time in the field of spintronics, due to the discovery of several magnetoresistance effects[52–58]. LSMO is well known for its applications in magnetic tunnel junctions with TMR values of 83% in the first report by Lu *et al.*[59] in 1996. Due to its display of magnetic properties above room temperature, LSMO is predicted to be a good candidate for low noise magnetoresistance sensors[60]. Tuning growth parameters, like background gas pressure or substrate temperature, allows us to alter material parameters like thickness, oxygen deficiency, strain, and crystallinity of the thin films to influence the magnetotransport properties. Besides the existing magnetoresistance devices[61–66], low energy and low noise AMR sensors are potential applications of LSMO[60].

LSMO is also used as a ferromagnetic injection layer in organic spin valves[67] and spin-OLEDs[68], showing the widespread use of LSMO in a basic scientific research setting. Based on the plentiful applications utilizing LSMO in one way or another, I do not doubt that LSMO research will continue to remain relevant in our increasingly Internet of Things based world.

A limiting factor for large-scale production is the growth of high-quality crystalline thin films. Scientific experiments often use films grown by pulsed laser deposition (PLD), which is a highly directional growth technique. Some companies like Solemates[69] focus on developing commercial-scale PLD systems which can be used for growing homogeneous thin films on industry sized wafers. The current day technology is not yet at a stage where PLD is widely implemented and optimized for large-scale industrial factory throughput but is marching ahead steadily.

Skyrmions

Magnetic hard disk drives (HDD) are a common non-volatile data storage device. Combining all HDD produced in 2014 the total storage capacity is 540 Exabytes[70]. In a HDD drive, the data is stored as the magnetization direction of tiny regions on a magnetic thin film. The desire to store more and more data led to a push to increase data density. Decreasing the size of the magnetic regions has been the main path towards increasing data density over the past 7 decades. The size reduction of the magnetic region resulted in an increase of the data density by 9 orders of magnitude from 2000 bit/in^2[71] in 1956 to surpassing the 1 Tbit/in^2 data density mark in 2012[72].

But in the last decade, the speed with which we design new methods of decreasing magnetic regions are slowing down. This is in part due to reaching technological and physical limits related to down-scaling (e.g. the Slater-Pauling Limit): therefore other non-volatile magnetic memories are investigated. Among the new techniques is the racetrack memory[73, 74], which is an experimental non-volatile memory. The advantage of a racetrack memory over the HDD is the absence of mechanical moving parts, which in turn gives the possibility to bypass the inherent two-dimensional HDD structure and expand in the third dimension[75].

Racetrack memory consists out of a magnetic wire and in the middle of the wire, the read/write lines are placed, as shown in figure 1.3. The magnetic regions split by domain walls in the wire can be pushed from one side of the wire to the other using a spin-polarized electric current[75]. The read/write wire is placed such that the magnetic regions or bits are pushed underneath the read/write wire following a close resemblance to a magnetic tape recorder. There are also technological challenges associated to the design of the racetrack memory, one of them is the high current density needed to move the domain walls. A high current density causes Joule heating[76, 77] with possible data-loss due to demagnetization. Another challenge is the reliable propagation of domain walls[76] especially in curved structures[78]. Nevertheless, in 2008 IBM showcased a proof-of-concept 3-bit racetrack memory device[73] leading to new insights to improve the racetrack memory[79].

Increasing the data density in a racetrack memory is possible by decreasing the magnetic regions or by switching to e.g. skyrmions. The latter has a few advantages as skyrmions are predicted to have (in theory) low energy consumption for their generation and destruction. Due to their topological protection, skyrmions repel each other. One can move them with magnonic currents[80, 81] or ultra-low electronic current densities[82, 83]. These features make skyrmions good candidates for improving future data storage[30, 31] or developing spintronic devices, like a
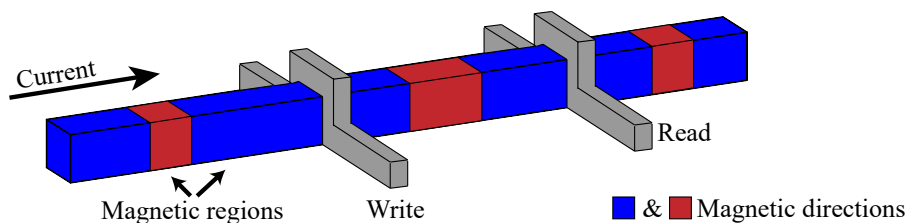
Figure 1.3: *Artist impression of a racetrack memory. A magnetic wire has magnetic regions with spins in two different directions representing '1' and '0'. The two lines connected to the memory are for writing and reading the state of the magnetic region.*

skyrmion racetrack memory[32, 33, 84].

Besides the low energy consumption, magnetic skyrmions can be as small as several nanometers in diameter[40, 85], stabilized by an interplay of Heisenberg exchange and the Dzyaloshinskii-Moriya interaction. For comparison, the size of a magnetic bit in a hard drive is approximately 100 nm in diameter, showing the potential increase in data density by using skyrmions. In skyrmion racetrack[84, 86] devices the presence or absence of a skyrmion can be interpreted as a '1' or a '0', where the skyrmions are pushed along a track as a solid-state analog to the magnetic tape recorder, in which the magnetic domains on a tape move along the steady read/write head. Later iterations on the skyrmion racetrack used a multi-lane racetrack [86] (see Fig. 1.4), where both the '1' and the '0' are encoded by a skyrmion.

In figure 1.4 (a) the orientation direction of a ferromagnetic regions are depicted, with a color representing a certain direction. The blue and red regions point in opposite directions and the gradual color shift means a gradual rotation of the magnetization direction. The presence of a skyrmion in the top lane of Fig. 1.4 (a) encodes the '1' lane and the presence of a skyrmion in the bottom lane represents a '0'. The repulsive force between the skyrmions[84] is used to keep the skyrmions from passing each other, and to keep the skyrmions traveling in straight lines. Hence a potential well is created based on the skyrmion-edge repulsion forces. The edge is the outer side of the well and the thicker middle part forms the splitting barrier between the two lanes as shown in figure 1.4 (a) and (b). To alter the position of the skyrmion, it can be destroyed in one lane and created in the other lane by using a current. Other suggestions for skyrmion racetracks are the use of two different types of skyrmions to indicate the '1' and '0', giving the potential to create a multi-state skyrmion memory. Fine-tuning the material parameters to (reliably) create skyrmion racetracks in the lab is an exciting challenge for the scientific community to take on in the coming decade.
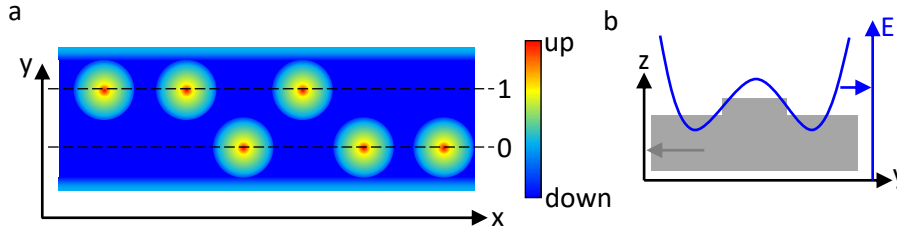
Figure 1.4: *(a) Artist impression of a skyrmion racetrack, based on Muller[86]. The colors represent the magnetization direction, where blue and red are opposite directions. The skyrmions (rainbow color) are pushed along a track and cannot pass each other as the repulsion energy between two skyrmions is too large. (b) Artist impression of the side view of the racetrack in grey color, based on Muller[86]. The middle is slightly thicker than the outside to create two potential wells, as shown with the solid line (right axis) in which skyrmions can reside. The potential wells are spaced such that skyrmions cannot pass each other in the adjacent lane.*

1.4   Outline of the Thesis

In this thesis, I present my work on magnetotransport measurements on LSMO thin films.

Chapter 2 explains all the necessary information needed to understand the experimental results presented in the successive chapters. The chapter is divided into 3 main sections, addressing the material properties, growth & fabrication, and lastly the transport measurements.

Chapter 3 discusses the temperature dependence of the magnetization of LSMO thin films. Decreasing the thickness of the film can result in magnetic behavior different from the typical Curie-Weiss law for ferromagnetic material. We observed two different magnetic phases below the Curie temperature, characterized by different magnetotransport characteristics and pure magnetic measurements. The latter indicating a change in preferential magnetic orientation from out-of-plane (at low temperature) to inplane (at higher temperatures).

In chapter 4, we investigate the inplane anisotropy of two thin films LSMO of different thickness on LaAlO$_3$. By rotating a magnetic field around [001] crystallographic axis of the sample, the inplane angle-dependent magnetoresistance is mea-

sured. Using formulas described in section 2.3, we explain the observed relation between magnetocrystalline anisotropy and thickness in the LSMO thin films.

In chapter 5, we investigate the anisotropy in the out-of-plane direction by varying the strain applied on thin films of LSMO. We observe a clear trend of a growing magnetic out-of-plane anisotropy with increasing out-of-plane tensile strain. Magentocrystalline anisotropy theory dictates that an elongation of the unit cell will favor a shift of the magnetic easy axis in the elongated direction for cubic systems. Upon increasing temperature, the magnetic easy axis falls back inplane for all samples, showing the conventional characteristics of LSMO thin films.

References

[1] J. M. D. Coey, "History of Magnetism and Basic Concepts", in *Handbook of Magnetism and Magnetic Materials*, edited by M. Coey and S. Parkin (Springer International Publishing, Cham, 2020).

[2] A. Kloss, *Geschichte des Magnetismus* (VDE verlag, Berlin, 1994).

[3] M. Fowler, Recuperado el **23**, 2012 (1997).

[4] L. Shu-hua, Isis **45**, 175 (1954).

[5] C. Wang, *Lun-heng*, edited by A. Forke, Second edition (Paragon book gallery, NJ, 1962).

[6] W. Gilbert, *De magnete, magneticisque corporibus, et de magno magnete tellure* (Peter Short, London, 1600).

[7] J. J. Fahie, *A history of electric telegraphy, to the year 1837* (E. & F.N. Spon, London, 1884).

[8] H. C. Ørsted, *Selected Scientific Works of Hans Christian ørsted*, edited by K. Jelved, A. D. Jackson, and O. Knudsen., 39A (Princeton University Press, Princeton, NJ, 1998).

[9] J. Maxwell, Trans. Cambridge Philos. Soc. **10** (1855).

[10] J. Maxwell, Philos. Mag. (1861).

[11] A. Einstein, Ann. Phys. **322**, 891 (1905).

[12] A. Ramirez, J. Phys. Condens. Matter **9**, 8171 (1997).

[13] Y. Tokura and Y. Tomioka, J. Magn. Magn. Mater. **200**, 1 (1999).

[14] L. M. Rodriguez-Martinez and J. P. Attfield, Phys. Rev. B **54**, 622 (1996).

[15] M. Baldini, T. Muramatsu, M. Sherafati, H.-K. Mao, L. Malavasi, P. Postorino, S. Satpathy, and V. V. Struzhkin, Proc. Natl. Acad. Sci. U.S.A. **112**, 10869 (2015).

[16] S. I. Khartsev, P. Johnsson, and A. M. Grishin, J. Appl. Phys. **87**, 2394 (2000).

[17] J. Zhang, X. Chen, Q. Zhang, F. Han, J. Zhang, H. Zhang, H. Zhang, H. Huang, S. Qi, X. Yan, L. Gu, Y. Chen, F. Hu, S.-S. Yan, B.-G. Liu, B. Shen, and J. Sun, ACS Appl. Mater. Interfaces **10**, 40951 (2018).

[18] A. Asamitsu and Y. Tokura, Phys. Rev. B **58**, 47 (1998).

[19] J.-B. Yau, X. Hong, A. Posadas, C. H. Ahn, W. Gao, E. Altman, Y. Bason, L. Klein, M. Sidorov, and Z. Krivokapic, J. Appl. Phys. **102**, 103901 (2007).

[20] T. Bolstad, E. Lysne, U. L. Osterberg, and T. Tybell, J. Magn. Magn. Mater. **487**, 165304 (2019).

[21] W. Dong, Y. Zhang, R. Qi, R. Huang, J. Yang, W. Bai, Y. Chen, G. Wang, X. Dong, and X. Tang, Ceram. Int., (AMEC-10) **43**, 493 (2017).

[22] M. Ziese, H. C. Semmelhack, and P. Busch, J. Magn. Magn. Mater. **246**, 327 (2002).

[23] K. Steenbeck, T. Habisreuther, C. Dubourdieu, and J. P. Senateur, Appl. Phys. Lett. **80**, 3361 (2002).

[24] H. Boschker, M. Mathews, P. Brinks, E. Houwman, A. Vailionis, G. Koster, D. H. A. Blank, and G. Rijnders, J. Magn. Magn. Mater. **323**, 2632 (2011).

[25] Y. Suzuki, H. Y. Hwang, S.-W. Cheong, and R. B. van Dover, Appl. Phys. Lett. **71**, 140 (1997).

[26] A. Tebano, C. Aruta, P. G. Medaglia, F. Tozzi, G. Balestrino, A. A. Sidorenko, G. Allodi, R. De Renzi, G. Ghiringhelli, C. Dallera, L. Braicovich, and N. B. Brookes, Phys. Rev. B **74**, 245116 (2006).

[27] J. Dho, Y. N. Kim, Y. S. Hwang, J. C. Kim, and N. H. Hur, Appl. Phys. Lett. **82**, 1434 (2003).

[28] P. Yu, Y.-H. Chu, and R. Ramesh, Mater. Today **15**, 320 (2012).

[29] M. Huijben, G. Koster, Z. L. Liao, and G. Rijnders, Applied Physics Reviews **4**, 041103 (2017).

[30] N. S. Kiselev, A. N. Bogdanov, R. Schäfer, and U. K. Rößler, J. Phys. D: Appl. Phys. **44**, 392001 (2011).

[31] J. Akerman, Science **308**, 508 (2005).

[32] R. Tomasello, E. Martinez, R. Zivieri, L. Torres, M. Carpentieri, and G. Finocchio, Sci Rep **4**, 6784 (2014).

[33] W. Kang, X. Chen, D. Zhu, X. Zhang, Y. Zhou, K. Qiu, Y. Zhang, and W. Zhao, 2018 IEEE 7th Non-Volatile Memory Systems and Applications Symposium, 7 (2018).

[34] K. Everschor-Sitte and M. Sitte, *Two skyrmions*, By Karin Everschor-Sitte and Matthias Sitte - Own work, CC BY-SA 3.0, https://commons.wikimedia.org/w/index.php?curid=37682157.

[35] C. Pappas, E. Lelievre-Berna, P. Falus, P. Bentley, E. Moskvin, S. Grigoriev, P. Fouquet, and B. Farago, Phys. Rev. Lett. **102**, 197202 (2009).

[36] S. Muhlbauer, B. Binz, F. Jonietz, C. Pfleiderer, A. Rosch, A. Neubauer, R. Georgii, and P. Boni, Science **323**, 915 (2009).

[37] T. Nakajima, H. Oike, A. Kikkawa, E. P. Gilbert, N. Booth, K. Kakurai, Y. Taguchi, Y. Tokura, F. Kagawa, and T.-h. Arima, Sci. Adv. **3**, e1602562 (2017).

[38] F. Büttner, I. Lemesh, and G. S. Beach, Sci. Rep. **8**, 1 (2018).

[39] W. Jiang, G. Chen, K. Liu, J. Zang, S. G. Te Velthuis, and A. Hoffmann, Physics Reports **704**, 1 (2017).

[40] N. Romming, C. Hanneken, M. Menzel, J. E. Bickel, B. Wolter, K. v. Bergmann, A. Kubetzka, and R. Wiesendanger, Science **341**, 636 (2013).

[41] N. Romming, A. Kubetzka, C. Hanneken, K. von Bergmann, and R. Wiesendanger, Phys. Rev. Lett. **114**, 177203 (2015).

[42] C. Hanneken, F. Otte, A. Kubetzka, B. Dupe, N. Romming, K. von Bergmann, R. Wiesendanger, and S. Heinze, Nat. Nanotechnol **10**, 1039 (2015).

[43] S. Ishiwata, T. Nakajima, J. Kim, et al., Phys. Rev. B **101**, 134406 (2020).

[44] S. Chakraverty, T. Matsuda, H. Wadati, J. Okamoto, Y. Yamasaki, H. Nakao, Y. Murakami, S. Ishiwata, M. Kawasaki, Y. Taguchi, Y. Tokura, and H. Y. Hwang, Phys. Rev. B **88**, 220405 (2013).

[45] A. Leonov and M. Mostovoy, Nat. Commun. **8**, 1 (2017).

[46] T. Kurumaji, T. Nakajima, M. Hirschberger, A. Kikkawa, Y. Yamasaki, H. Sagayama, H. Nakao, Y. Taguchi, T.-h. Arima, and Y. Tokura, Science **365**, 914 (2019).

[47] D. A. Gilbert, B. B. Maranville, A. L. Balk, B. J. Kirby, P. Fischer, D. T. Pierce, J. Unguris, J. A. Borchers, and K. Liu, Nat. Commun. **6**, 9462 (2015).

[48] W. Jiang, P. Upadhyaya, W. Zhang, G. Yu, M. B. Jungfleisch, F. Y. Fradin, J. E. Pearson, Y. Tserkovnyak, K. L. Wang, O. Heinonen, S. G. E. t. Velthuis, and A. Hoffmann, Science **349**, 283 (2015).

[49] N. Nagaosa, X. Z. Yu, and Y. Tokura, Phil. Trans. R. Soc. A **370**, 5806 (2012).

[50] K. Meng, A. S. Ahmed, M. Bacani, A. Mandru, X. Zhao, N. Bagues, B. Esser, J. Flores, D. McComb, H. Hug, et al., Nano Lett. **19**, 3169 (2019).

[51] P. Zhang, A. Das, E. Barts, M. Azhar, L. Si, K. Held, M. Mostovoy, and T. Banerjee, Phys. Rev. Res. **2**, 032026 (2020).

[52] J. O'Donnell, J. N. Eckstein, and M. S. Rzchowski, Appl. Phys. Lett. **76**, 218 (2000).

[53] M. Egilmez, K. H. Chow, and J. A. Jung, Mod. Phys. Lett. B **25**, 697 (2011).

[54] W. Thomson, Proc. R. Soc. Lond. **8**, 546 (1857).

[55] T. McGuire and R. Potter, IEEE Trans. Magn. **11**, 1018 (1975).

[56] M. Bibes, B. Martinez, J. Fontcuberta, V. Trtik, C. Ferrater, F. Sanchez, M. Varela, R. Hiergeist, and K. Steenbeck, J. Magn. Magn. Mater. **211**, 206 (2000).

[57] X. G. Chen, J. B. Yang, Y. B. Yang, C. S. Wang, S. Q. Liu, Y. Zhang, J. Z. Han, and Y. C. Yang, J. Appl. Phys. **115**, 043904 (2014).

[58] Y. Bason, L. Klein, J.-B. Yau, X. Hong, and C. H. Ahn, Phys. Status Solidi C **1**, 3336 (2004).

[59] Y. Lu, X. W. Li, G. Q. Gong, G. Xiao, A. Gupta, P. Lecoeur, J. Z. Sun, Y. Y. Wang, and V. P. Dravid, Phys. Rev. B **54**, R8357 (1996).

[60] O. Rousseau, S. Flament, B. Guillet, M. L. C. Sing, and L. Méchin, Proceedings **1** (2017).

[61] O. Aleksic, S. Savic, M. Nikolic, L. Sibinoski, and Lukovic, Microelectron. Int. **26**, 30 (2009).

[62] L. Balcells, A. E. Carrillo, B. Martınez, F. Sandiumenge, and J. Fontcuberta, J. Magn. Magn. Mater. **221**, 224 (2000).

[63] J. Z. Sun, A. Gupta, G. Xiao, P. L. Trouilloud, and P. P. Lecoeur, "Magnetic devices and sensors based on perovskite manganese oxide materials", U.S. patent US-5792569-A (11 August 1998).

[64] Y. Xu, U. Memmert, and U. Hartmann, Sens. Actuators, A **91**, 26 (2001).

[65] L. Balcells, R. Enrich, J. Mora, A. Calleja, J. Fontcuberta, and X. Obradors, Appl. Phys. Lett. **69**, 1486 (1996).

[66] S. Balevicius, N. Zurauskiene, V. Stankevic, S. Kersulis, A. Baskys, V. Bleizgys, J. Dilys, A. Lucinskis, A. Tyshko, and S. Brazil, IEEE Trans. Instrum. Meas. **69**, 2808 (2020).

[67] Z. H. Xiong, D. Wu, Z. Valy Vardeny, and J. Shi, Nature **427**, 821 (2004).

[68] M. Cesaria, A. P. Caricato, G. Maruccio, and M. Martino, J. Phys. Conf. Ser. **292**, 012003 (2011).

[69] *Solmates*, `https://www.solmates-pld.com/deposition/5812/`, Accessed: 2021-07-07.

[70] *HDD annual unit shipments increase in 2014*, `https://www.forbes.com/sites/tomcoughlin/2015/01/29/hdd-annual-unit-shipments-increase-in-2014/?sh=49ed0f5d4e21`, Accessed: 2021-07-07.

[71] J. Harker, D. Brede, R. Pattison, G. Santana, and L. Taft, IBM J. Res. Develop. **25**, 677 (1981).

[72] *Seagate*, `https://www.seagate.com/nl/nl/news/news-archive/terabit-milestone-storage-seagate-master-pr/`, Accessed: 2021-07-07.

[73] M. Hayashi, L. Thomas, R. Moriya, C. Rettner, and S. S. P. Parkin, Science **320**, 209 (2008).

[74] *Ibm research*, `https://www.research.ibm.com/labs/almaden/?racetrack`, Accessed: 2021-07-07.

[75] S. S. Parkin, Sci. Am. **300**, 76 (2009).

[76] S. S. P. Parkin, M. Hayashi, and L. Thomas, Science **320**, 190 (2008).

[77] R. Bläsing, T. Ma, S.-H. Yang, C. Garg, F. K. Dejene, A. T N'Diaye, G. Chen, K. Liu, and S. S. Parkin, Nat. Commun. **9**, 1 (2018).

[78] R. Bläsing, A. A. Khan, P. C. Filippou, C. Garg, F. Hameed, J. Castrillon, and S. S. Parkin, Proc. IEEE **108**, 1303 (2020).

[79] S. Parkin and S.-H. Yang, Nature nanotechnology **10**, 195 (2015).

[80] C. Schutte and M. Garst, Phys. Rev. B **90**, 094423 (2014).

[81] K. Everschor, M. Garst, B. Binz, F. Jonietz, S. Mühlbauer, C. Pfleiderer, and A. Rosch, Phys. Rev. B **86**, 054432 (2012).

[82] X. Yu, N. Kanazawa, W. Zhang, T. Nagai, T. Hara, K. Kimoto, Y. Matsui, Y. Onose, and Y. Tokura, Nat. Commun. **3**, 1 (2012).

[83] J. Iwasaki, M. Mochizuki, and N. Nagaosa, Nat. Commun. **4**, 1 (2013).

[84] X. Zhang, G. Zhao, H. Fangohr, J. P. Liu, W. Xia, J. Xia, and F. Morvan, Sci. Rep. **5**, 1 (2015).

[85] S. Heinze, K. Bergmann, M. Menzel, J. Brede, A. Kubetzka, R. Wiesendanger, G. Bihlmayer, and S. Blügel, Nat. Phys. **7**, 713 (2011).

[86] J. Muller, New J. Phys. **19**, 025002 (2017).

Chapter 2

Theoretical Concepts and Experimental Setup

Abstract

This chapter discusses the theoretical concepts and experimental setup needed to understand the work presented in this thesis. The chapter is split into three sections. The first section discusses the materials that are used as thin films and substrates. In the second section, the growth and fabrication of the thin film are discussed. In the last section, I present the experimental measurement setup, along with the theoretical concepts related to the experiments.

2.1 Perovskites

Three perovskite materials are used in this thesis, namely $La_{0.67}Sr_{0.33}MnO_3$, $LaAlO_3$, and $SrTiO_3$. These materials belong to the ABO_3 perovskite group where A and B are cations, and O is oxygen. The A site is a rare earth (e.g. $La^{2+/3+}$ or Sr^{2+}) and B is a transition metal (e.g. Ti^{4+}, Fe^{4+}, Al^{4+} or $Mn^{3+/4+}$), where the transition metal is surrounded by six-fold coordinated oxygen octahedral. As depicted in figure 2.1, the rare earth ions surround the oxygen octahedral with a twelve-fold coordination. An important thing to note is that the oxygen atom bonds with all other atoms and therefore are important in the system, not only for the bonding but these bonds also influence other properties like conduction and magnetism.

Moreover, the oxygen bonding allows a wide range of materials to be synthesized in the same ABO_3 perovskite structure, as the rare earth and transition metal atoms can be exchanged for others atoms belonging to the same group. Depending on the desired properties, a combination of transition metal and rare earth ions is selected. For instance, the transition metals Mn, Ru and Fe will give magnetic properties while perovskites with Ir are known for their large spin orbit coupling. As for the rare earths, the valence state as well as the atom size can play a role for creating a stable ABO_3 perovskite.
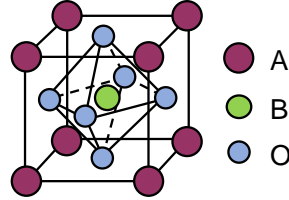
Figure 2.1: *A diagram of the ABO$_3$ unit cell where the corner atoms are made
up of rare earth elements. The face centered atoms are of oxygen and
the centered atom is of the transition metal elements.*

According to their close packing structure, the ideal ABO$_3$ perovskite is cubic in
symmetry in which all the ions fit nicely packed in the unit cell. In reality, however,
different A and B ions have different radii, resulting in the distortion of the unit
cell. The amount of distortion is predicted by the Goldschmidt tolerance factor[1].
Using the ionic radii of oxygen and both the A and B elements, in the ABO$_3$ type
perovskite, the tolerance factor (t) is determined by

$$t = \frac{r_A + r_B}{\sqrt{2}(r_B - r_O)},$$

(2.1)

where r$_{subscript}$ is the ionic radii of the respective element. In the ideal case, like
SrTiO$_3$, the Goldschmidt criterion is one. Reducing the tolerance factor below 1 re-
sults in an octahedral tilt, as the unit cell leaves space for the oxygen ions to move
in between the B ions. A tolerance factor larger than 1 indicates an elongation of
the unit cell, which distorts the cubic symmetry into a tetragonal or hexagonal crys-
tal symmetry. A symmetry change in a material causes different orbitals to overlap,
which in turn can result in a large distortion of properties, due to strong coupling be-
tween conduction, magnetism and shape of the unit cell. Examples of effects caused
by distortions are the Jahn-Teller effect[2], ferroelectricity[3], a reduction of the opti-
cal band gap[4] or oxygen deficiency[5]. Of these mentioned effects the Janh-Teller
effect is discussed in section 2.1.1 as this phenomenon plays a key role in our obser-
vations.

In the previous section, a piece of homogeneous material is discussed. In practi-
cal applications, however the perovskite is finite in size and will interact with other
materials altering its properties. This interaction allows for extra tuning opportuni-
ties to enhance or create the desired combination of physical properties. Utilizing
thin film growth methods, like pulsed laser deposition (PLD), the unit cells of the

thin film are (epitaxially) grown on a substrate. In this thesis, I focused on the behavior of thin films of $La_{0.67}Sr_{0.33}MnO_3$ grown on the substrates $LaAlO_3$ and $SrTiO_3$. In these particular cases, the growth is tuned such that the thin films copy the inplane crystal structure of the substrate, as shown in figure 2.2. In practice, this results in a continuation of the (ABO_3) lattice structure of the material, like stacking multiple unit cells on top of each other (unit cells are indicated as little cubes in figure 2.2). At the interface the La, Sr and Mn are replacing the substrate's A and B-ions in the ABO_3 unit cell. Replicating the inplane lattice structure of the substrates results in a deformation of the unit cell, with respect to the bulk state. The deformation causes a different bonding overlap with oxygen atoms as the atoms are moved either further apart (Fig. 2.2 (a)) or closer together (Fig. 2.2 (b)). Tensile deformations results in a higher Curie temperature in $La_{0.67}Sr_{0.33}MnO_3$[6–9] or a rotation of the magnetic easy-axis[10–13] when $La_{0.67}Sr_{0.33}MnO_3$ is grown on $LaAlO_3$. A more detailed description of how the orbital overlap influences the properties of $La_{0.67}Sr_{0.33}MnO_3$ is discussed with respect to the Jahn-Teller effect in section 2.1.1.

(a)　　　　　　　　　　　　　　　(b)
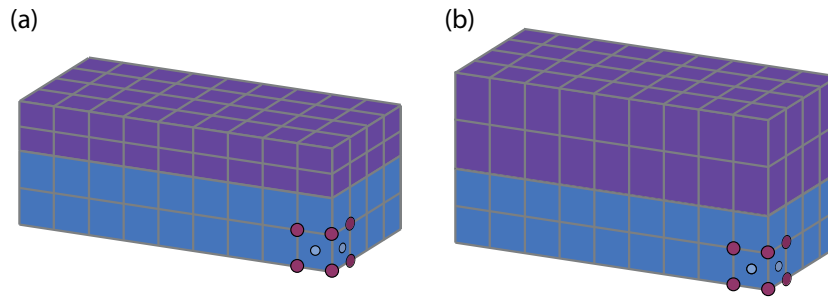
Figure 2.2: Epitaxial thin film grown with (a) tensile strain ($La_{0.67}Sr_{0.33}MnO_3$ on $SrTiO_3$) and (b) compressive strain ($La_{0.67}Sr_{0.33}MnO_3$ on $LaAlO_3$). In both cases the unit cell is depicted as a cube. The purple is the deformed unit cell of $La_{0.67}Sr_{0.33}MnO_3$ and the blue is the (pseudo-cubic) $SrTiO_3$ or $LaAlO_3$.

The deformation of the unit cell is described by the strain formula, which relates the deformation to the original size of the unit cell.

$$Strain = \frac{a_{thinfilm} - a_{crystal}}{a_{crystal}} * 100\%, \quad (2.2)$$

where $a_{thinfilm}$ is the lattice constant of the thin film and $a_{crystal}$ is the lattice constant of the single crystal. The larger the deformation in a material, the larger the strain. Changing substrates is one method of altering the strain on a thin film.

Changing substrate orientation is another option to alter the strain experienced by the thin film. Besides altering the strain on a film, in some cases, a surface charge is introduced by the termination layer, as shown in figure 2.3. At this termination layer, a special situation arises as the ABO_3 perovskite interacts with another perovskite material.
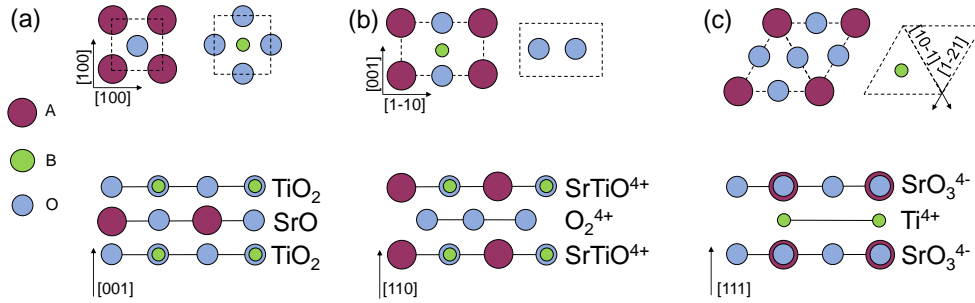
Figure 2.3: *Different crystallographic cutting planes result in different surface atoms. In the bottom of each figure, the cut through of each orientation is given. At the top, the two different surface terminations are shown as a top view. The surface charge depicted is located on $SrTiO_3$. (a) [001] oriented substrate. (b) [110] oriented substrate. (c) [111] oriented substrate. The three different orientations of the substrate are a) [001], (b) [110] and (c) [111].*

Figure 2.3 depicts several regular spaced planar directions (h,k,l) and their respective surface atoms for the ABO_3 perovskite. For instance, in the [001] direction the regular spaced planes are divided between AO (LaO, and SrO) and BO_2 (MnO_2, AlO_2, and TiO_2) planes. Ideally, a substrate has a single termination plane of either plane, but in practice, this is often not the case. For instance, an offset in the cutting angle during fabrication will cause multiple planes to be intersected, causing a mixed terminated surface. Such a surface requires a special surface treatment to achieve single termination. A famous example, where different properties arise depending on the termination plane is the $LaAlO_3/SrTiO_3$ interface, which is conducting when the $SrTiO_3$ is TiO_2 terminated and insulating when the $SrTiO_3$ is SrO terminated[14].

In this thesis, we use TiO_2 terminated $SrTiO_3$ for films grown on $SrTiO_3$. The $LaAlO_3$ substrates did not receive any termination treatment as there is a debate in literature about the effectiveness of such a treatment[15, 16].

The presence of different atoms at the surface or changing the orientation of the substrate will influence the oxygen bonds in the thin film. As a consequence, the oxygen coordination at the (interface) surface is altered. For example, the $LaAlO_3$/$SrTiO_3$ interface is conducting when grown on specific cutting directions ([001], [110], and [111]) of $SrTiO_3$, and insulating when grown on other cutting directions[14].

Lastly, oxygen deficiency also plays a key role in the crystal structure. ABO_3 perovskites with a reducible B-cation can form vacancy-ordered crystal structures with the $A_nB_nO_{3n-1}$ stoichiometry, often also marked as $ABO_{3-\delta}$ or ABO_n in thin film literature. Depending on the oxidation state of oxygen, a different superstructure (e.g. brownmillerite) is formed causing, for instance, the magnetization or conductivity to change. In this thesis, we took care to grow fully oxidized thin films by introducing annealing steps. Therefore, we will not discuss oxygen vacancy phenomena. In the following sections, three materials are discussed in more detail: the first material, $La_{0.67}Sr_{0.33}MnO_3$, is used as a thin film material, while the other two, $LaAlO_3$, and $SrTiO_3$, are used as substrates.

2.1.1 $La_{0.67}Sr_{0.33}MnO_3$

$La_{0.67}Sr_{0.33}MnO_3$ (LSMO) is a well-studied manganite perovskite with the general formula $Re_{1-x}A_xMnO_3$, where Re is a rare-earth cation and A is an alkaline-earth. The alkaline-earth strontium (Sr^{2+}) and the rare-earth lanthanum (La^{3+}) are mixed to change the average valence state of the manganese atom. Altering the valence state gives rise to different electronic and magnetic properties, as shown in figure 2.5 (a). On one hand, when x=0, $LaMnO_3$ is an A-type antiferromagnetic material (Fig. 2.4) with an orthorhombic lattice structure due to a Jahn-Teller deformation of the oxygen octahedral. Upon increasing the Sr concentration, $La_{1-x}Sr_xMnO_3$ changes magnetic ordering to a ferromagnetic state with a maximum Curie temperature of 360 K, at x=0.33. Increasing the Sr concentration further, at x=0.5, charged ordered states are formed. On the other end, at x=1, $SrMnO_3$ is an G-type antiferromagnetic material (Fig. 2.4).
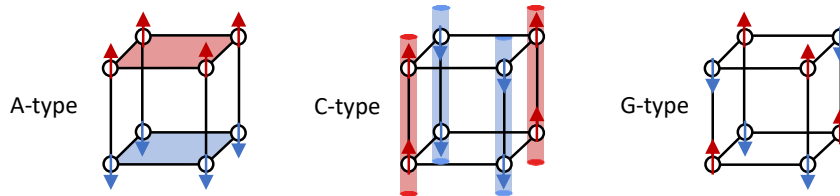
Figure 2.4: *The three types of antiferromagnetic interaction. A-type is a ferromagnetic plane (shaded blue (up spin) and red (down spin)) which are antiferromagnetically coupled to other planes. C-type are rods of ferromagnetic spins (shaded blue (up) and red (down)) coupled antiferromagnetically with other rods. G-type is general antiferromagnetic without a ferromagnetic sub-structure.*

The change in valence state and the subsequent change in magnetic order can be explained by a change in conduction mechanism in $La_{1-x}Sr_xMnO_3$. This is best explained by first understanding the unit cell of LSMO. The full unit cell is rhombohedral in bulk, such that it can be approximated as a cubic unit cell. For all purposes in this thesis, we will treat the unit cell to be pseudo-cubic, with a lattice constant of 3.88 Å, as depicted in Fig. 2.5 (b). Fig. 2.5 (b) shows $Mn^{3+/4+}$ at the center of a unit cell surrounded by an oxygen octahedral, and the corners are made up of lanthanum or strontium ions. The oxygen octahedron indirectly connects its Mn to the next Mn atom, creating an Mn-O-Mn bond. These bonds are responsible for the conduction and the itinerant magnetism of the material via either superexchange[17–21] or double-exchange[22], based on the Goodenough–Kanamori-Anderson (GKA) rules, which are explained in the following section.
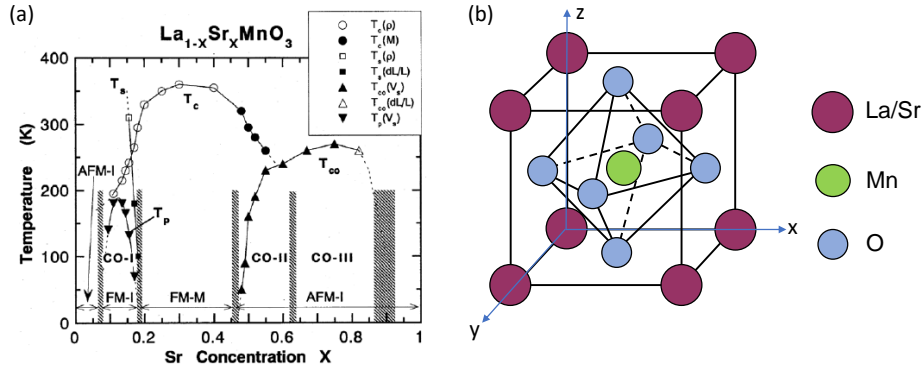
Figure 2.5: *(a) Phase diagram of $La_{1-x}Sr_xMnO_3$ denoting its magnetic properties. Figure reproduced from [23] © (1998) The Physical Society of Japan. (b) A schematic diagram of the LSMO unit cell where the corner atoms are made up of lanthanum or strontium ions. The face centered atoms are oxygen and the center atom is Mn. The occupation ratio between strontium and lanthanum determines the relative charge of the manganese ion.*

Superexchange Mechanism

The superexchange mechanism, proposed in 1934 by Hendrik Kramers[17], is a (strong) antiferromagnetic coupling between an Mn-ion and its next-to-nearest neighbors (also a Mn-ion) in MnO crystals. In MnO crystals, superexchange is possible via electron hopping from and to the Mn $d_{z^2-r^2}$-orbital via the oxygen p_z-orbital, see figure 2.6. For the exchange to happen, one of the two electrons in the O^{2-}-ion hops to the Mn^{3+}-ion. The void left by the electron in the O^{2-}-ion is filled by an electron from the other Mn-ion, completing the indirect electron transfer from one Mn-ion to the next Mn-ion.

The proposed antiferromagnetic coupling is based on two elements. Firstly, the donor and receiver atom are the same, which prefer the singlet state, reducing the energy of the system. Secondly, the spins states of both ions are coupled via their nearest neighbor.
The model for superexchange was later improved by Goodenough, Kanamori and Anderson. They formulated the GKA rules based on symmetry relations and orbital occupancy of the donor and acceptor orbitals in order to determine whether a system would exhibit antiferromagnetism or ferromagnetism.
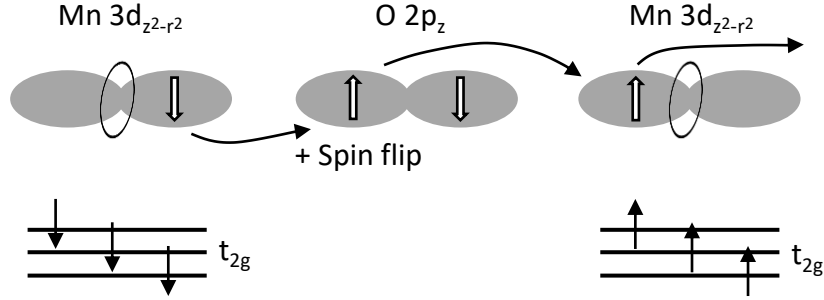
Figure 2.6: *Diagram depicting superexchange in a Mn^{3+} - O - Mn^{3+} bond. Conduction starts with one electron hopping outside the graph, indicated by the arrow from the Mn^{3+} on the right. The void is filled by an electron from the oxygen p-orbital. The oxygen orbital void is filled with an electron from the Mn-ion on the left. When, at last, the right Mn^{3+}-ion receives an electron from outside the graph the conduction is completed.*

In most cases, the GKA rules use the Pauli exclusion principle to determine the magnetic state of the Mn-O-Mn bond. There are three main rules.

- First of all, two half-filled orbitals coupled via an intermediary will favor strong antiferromagnetic coupling.

- Secondly, the coupling of an ion with half-filled orbitals with an ion with filled orbitals via an intermediary will result in ferromagnetic coupling.

- Lastly, coupling between an half-filled or filled orbital and one with a vacant orbital can be either antiferromagnetic or ferromagnetic.

The antiferromagentic exchange usually dominates when superexchange is the dominant transport mechanism. Perturbation theory predicts the hopping energy needed for transport in the energy Hamiltonian[24]

$$H = \frac{2t_{Mn,O}^2}{U} \hat{S}_1 \cdot \hat{S}_2, \tag{2.3}$$

where t is the hopping energy, U is the Hubbard energy, and S is the spin scalar product. The other charge transport exchange mechanism found in $La_{1-x}Sr_xMnO_3$ is the double-exchange mechanism.

Double-Exchange mechanism

Double-exchange is defined as an magnetic interaction between two transition metal ions via an oxygen ion. In our case, an electron can hop from a Mn^{3+} to an Mn^{4+} ion via an oxygen p-orbital as depicted in figure 2.7. The exchange mechanism was hypothesized by Zener [22] to explain the ferromagnetic or antiferromagnetic ground state of manganites. This exchange happens when the ground-state of the manganite is ferromagnetic, as spin is conserved during the exchange.
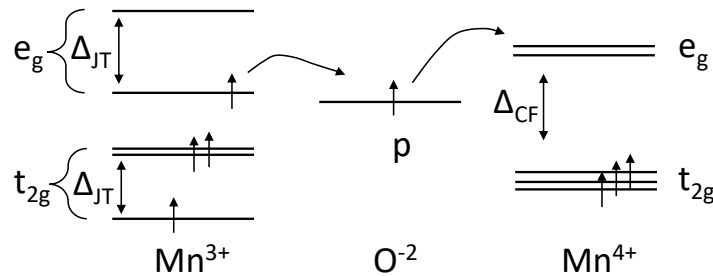
Figure 2.7*: Diagram depicting double-exchange. An electron can hop from the oxygen p-orbital to the Mn^{4+} ion, when the spin of the hopping electron and the Mn-ion electrons are parallel aligned, as shown in the right (O-Mn^{4+}) side of the figure. This process is more favorable for parallel spins due to Hund's rule. The missing electron in the oxygen p-orbital is replaced by an electron from the Mn^{3+} ion, when the Mn^{3+} spins are aligned with the missing spin in the oxygen-ion, as shown in the left (Mn^{3+}-O) side of the figure.*

The electron hopping from Mn^{3+} to Mn^{4+} is energetically favorable due to the Jahn-Teller distortion, causing a shift in energy levels of the 3d e_g orbitals on top of the crystal field splitting. Both hopping events, from and to the oxygen 2p-orbital, are more likely to happen if the spin momentum is conserved. Spin momentum conservation during hopping ensures that Hund's rule is obeyed in the recipient orbitals. The ability to hop reduces the overall energy in the system, as the Jahn-Teller deformation is happening in all Mn-ions, leading to a ferromagnetic ground state.

Jahn-Teller Effect

The different valence states of the Manganese-ions gives rise to different magnetic and electronic phases (see figure 2.5 (a)). With a change in valence state, the shape of the unit cell will change. The deformation can be explained by examining the 3d orbitals and their overlap with the neighboring atoms in the unit cells. 3d orbitals are separated into 2 groups; firstly, the 3d e_g orbitals, and secondly, the 3d t_{2g} orbitals. The lobes of the two e_g orbitals ($d_{z^2-r^2}$ and $d_{x^2-y^2}$) of the Mn-ion point along the axes in the Cartesian coordinate system, as shown in figure 2.8. While the lobes of the three 3d t_{2g} orbitals (d_{xy}, d_{xz} and d_{yz}) point in-between the axes, as shown in the bottom row of figure 2.8, which have less orbital overlap with the oxygen p-orbitals (see figure 2.9 (c-e)).
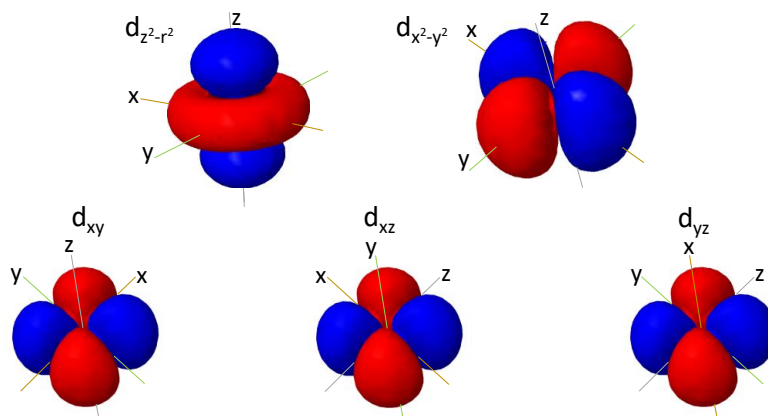
Figure 2.8*: Schematic diagram of the atomic 3d-orbitals, the red is the negative lobe and the blue is the positive lobe of the orbital. Taken from ChemTube3D[25] under the creative commons 2.0 license. The Cartesian axes are added to indicate the orbital extension into space.*

In vacuum, with only the Mn-ion present, no energy splitting exists. However, in a crystal structure, the presence of neighboring atoms results in a crystal field splitting. In an LSMO unit cell, the Mn is surrounded by the oxygen octahedral; hence the oxygen p_n (n = x, y, or z) orbitals influence the preferred occupation of the orbitals.

To minimize the energy in the system, the coulomb repulsion of the electrons should be minimized which is possible by minimizing the overlap between orbitals. By drawing the orbitals and their overlap, see figure 2.9, the low and high energy
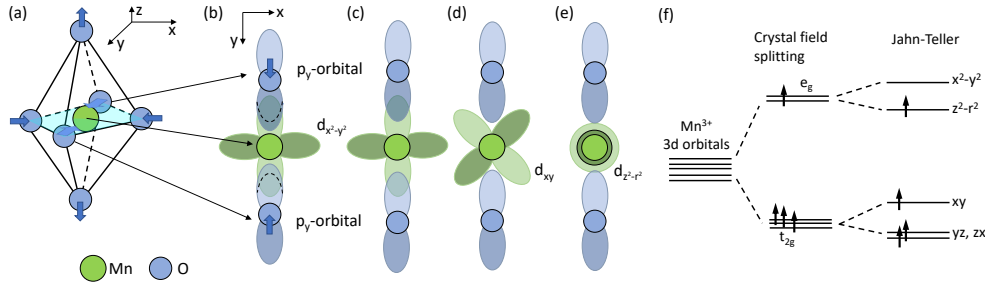
Figure 2.9: *Showing orbital overlap, unit cell deformation and the energy change of the deformation (a) Jahn-Teller distortion in the oxygen octahedral causing elongating the unit cell. (b) Orbital overlap for the $d_{x^2-y^2}$-orbital when the unit cell is deformed (c)/(d)/(e) Orbital overlap for the $d_{x^2-y^2}$/d_{xy}/$d_{z^2-r^2}$-orbitals with the p_y-orbital in the pristine case. (f) energy splitting of the 3d states due to crystal field and Jahn-Teller deformation.*

orbitals can be identified. The minimization of energy results in a preferred occupation of the three 3d t_{2g} orbitals. These orbitals (e.g. d_{xy} in figure 2.9 (d)) have minimal overlap with the p_n-orbitals (n = x, y, or z), and therefore the lowest coulomb repulsion of the 3d orbitals. When adding an extra (fourth) electron to the system, the electron has to reside in one of the two d e_g orbitals ($d_{z^2-r^2}$ and $d_{x^2-y^2}$). To minimize the bond overlap between the oxygen p_n orbital and the e_g orbital, the unit cell can deform lifting the twofold degeneracy, as shown in figure 2.9 (a), where the dark blue arrows indicate the displacement of the oxygen atoms with respect to the pristine oxygen octahedral.

Compressive strain or a Jahn-Teller distortion results in an elongated unit cell in the z-direction, reducing the orbital overlap for the $d_{z^2-r^2}$-orbital, which lowers the orbital overlap for four out of six p-orbitals. Consequently, lowering the coulomb repulsion and hence the energy. Figure 2.9 (e) shows the $d_{z^2-r^2}$-orbital interacting with the oxygen p_y-orbital, where the bright color is the negative lobe and the darker green is the positive lobe of the orbital. Moving the oxygen ion closer to the Manganese ion increase the interaction with the negative and positive lobes resulting in a net lowering of the $d_{z^2-r^2}$ state. For the $d_{x^2-y^2}$-orbital, the orbital overlap increases, as drawn in figure 2.9 (b), with respect to the pristine state, see Fig. 2.9 (c), due to the Jahn-Teller deformed octahedral state. The increased orbital overlap changes the coulomb energy which forces the $d_{x^2-y^2}$ & d_{xy} state to go up in energy as depicted in figure 2.9 (f). In a mixed valence system like LSMO, the ratio Mn^{3+}/Mn^{4+} is altered by varying the La/Sr ratio. The additional electron in

the Mn^{3+} ion can hop between multiple unit cells lowering the overall energy of the system, which is reverted to as the dynamic Jahn-Teller effect. As both Mn-ions prefer the singlet state and spin is conserved in the double-exchange mechanism, a ferromagnetic ground state will be favored by the material.

The specific $La_{0.67}Sr_{0.33}MnO_3$ compound studied in this thesis is, in bulk, a ferromagnetic metallic material.

2.1.2 LaAlO$_3$

Lanthanum aluminate, $LaAlO_3$ (LAO), is an inorganic perovskite with a rhombohedral structure with lattice constants a=3.79 Å and c= 13.11 Å resulting in a pseudo-cubic lattice parameter of 3.79 Å[26]. Above 708 K, LAO undergoes a phase transition to a cubic structure with lattice length of 3.82 Å. LAO is mainly used as a substrate, due to its desirable properties like high dielectric constant and diamagnetic behavior, making it an ideal substrate for high T_c superconducting, magnetic or ferro-electric thin films. As a thin film, it is often used as an insulating barrier due to its high dielectric constant. The most known application is the LAO/STO interface, giving rise to superconductivity at the interface while both STO and LAO being insulators.

As a substrate or single crystal, LAO is known to give twinning, visible to a naked eye as can be seen in figure 2.10 (b).
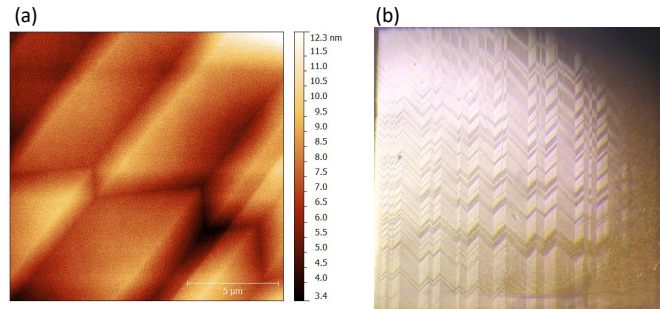
Figure 2.10: *(a) AFM image and (b) optical microscope image of a LAO [001] oriented substrate with twinning*

Though some literature suggest the preparation of the LAO substrate[15, 27], in this work we did not actively terminate the surface. This is mainly due to, debate in literature if getting a clean single phase terminated substrate[16, 28, 29] is possible. Secondly, though there might be mixed termination at room temperature, some

studies observe a single termination at growth temperatures (750 °C)[30, 31].

2.1.3 SrTiO$_3$

Strontium titanate, SrTiO$_3$ (STO), is also an inorganic perovskite, industrial synthesized in the late 1950's as a substitute for diamond in jewelry. It's other uses are in solid oxide fuel cells, precision optics, and as a substrate for growing thin films. Its high dielectric constant (300) and insulating behavior (10^9 Ω cm) combined with its cubic perovskite structure (a=3.905 Å) and high melting point (2080 °C) make it a suitable substrate for thin film growth. As an undoped crystal, STO is transparent with an indirect bandgap of 3.25 eV[32], and is know for its terrace structure in the [001] direction due to a small offset in the cutting angle while producing the substrates. The synthesized material has a non-polar mixed surface termination of TiO$_2$ and SrO, which can be altered to single TiO$_2$ termination by using a termination protocol involving etching with hydrofluoric acid. After termination and oxygen annealing (at 960 °C) neat terraces are observed, forming a well-known substrate for growing perovskite thin films.
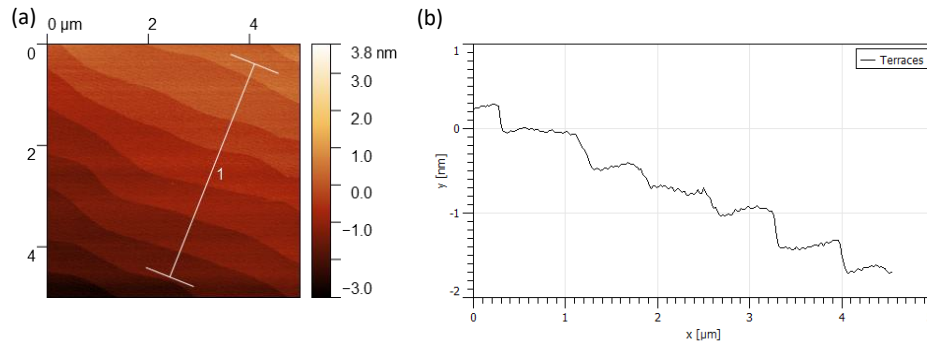
Figure 2.11: *(a) AFM image of an STO substrate and (b) height profile of the STO terraces.*

The [110] and [111] crystal cuts are polar in nature and have a layer charge of +/- 4e, which leads to a surface reconstruction. This may lead to a charge transfer in the thin film, altering the (expected) properties of the thin film. An example of this is the charge transfer from LAO [001] (+/- e) to STO [001] resulting in a superconducting 2DEG close to the interface of STO/LAO. Besides STO's insulating nature and cubic crystal structure, STO has no magnetic order. This is due to complete ionization of Sr^{2+} (completely filled band structure), leaving electrons only in the oxygen 2p band and the Ti 3d^0 bands. The latter gives rise to the colorless appearance due to the lack

of d-to-d transitions, and the lack of long range magnetic order in the compound, which makes STO an ideal substrate for magnetic studies as no complex background compensation is needed. For a more in depth review on STO, I refer the reader to Ana Marques's thesis chapter 2, in which the author describes the properties of STO in great detail [4].

2.2 Growth & Fabrication

In this thesis, I studied the transport properties of perovskite thin films grown on perovskite substrates. Preparation of these samples consists of two parts. The first step, is to grow the films with pulsed laser deposition. Secondly, the deposition of gold contacts, followed by etching the thin film, resulting in creating the Hall bars used in this thesis.

2.2.1 Growth

Thin films can be grown utilizing various methods, depending on the needs one method might be better than others. For growing complex oxides, a technique called pulsed laser deposition is frequently used, as it bears several advantages over other techniques.

Pulsed Laser Deposition

Pulsed laser deposition (PLD) is a physical deposition technique which has its origin in 1965, but gained significant scientific interest after 1987 due to the demonstration of growth of epitaxial thin films. For complex oxides, like LSMO, PLD became the growth method of choice as it allowed for the use of an oxygen background, significantly reducing the amount of oxygen vacancies in thin films. PLD is a process where a strong pulsed KrF ($\lambda = 248$ nm) laser ablates a target material into a plasma which in turn recrystallizes to grow a thin film on a substrate, see figure 2.12 (a) for a schematic drawing. To achieve homogeneous growth, a set of lenses is used to focus the laser on the target, creating a high energy density pulses to ablate the target material into a plasma. Usually an energy density between 0.1 to 5 J/cm^2 is required to locally super heat the target as shown in figure 2.12 (c) for a cross section of the target.

The fluence determines the ablation temperature, an incorrect fluence might lead to an off-stoichiometric thin film. Off-stoichiometric ablation due to a low fluence might lead to a compound remaining at the target, as the target does not get hot

enough for a compound to ablate. Secondly, a high fluence might cause the formation of a new compound with a high melting point, causing off-stoichiometric ablation. Intuitively, this makes the fluence a parameter to control the amount of material ablated as well as a control over the phase/stoichiometry of the material which gets evaporated. This allows for a wide range of new materials to be studied in thin films as PLD can deposit a mixture of elements with different melting points.
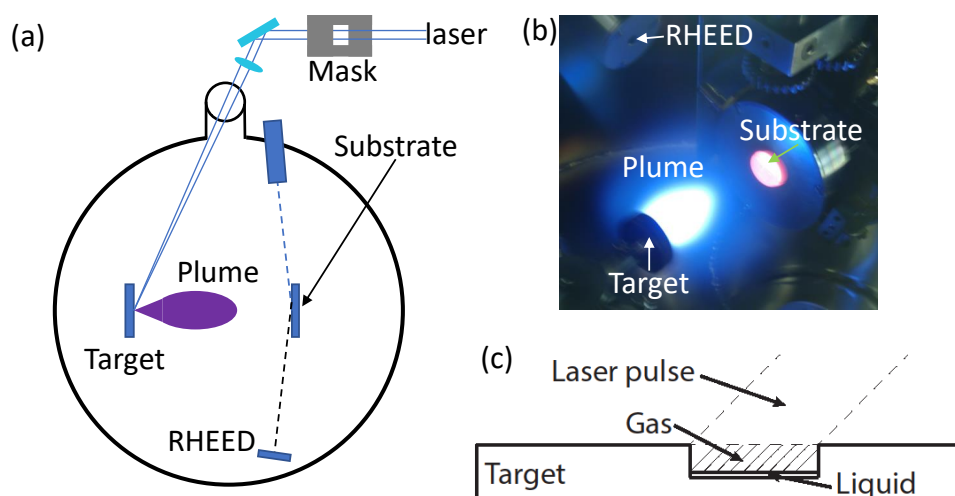
Figure 2.12: *(a) A schematic drawing of a PLD setup. (b) A picture of the inside of our PLD system. (c) A schematic drawing of a PLD laser pulse interacting with a target. Most target material hit by the laser pulse will ablate, a small layer of the target material will become liquid and re-solidify.*

After ablation, the particles are in the plasma state. The precise state in which the particles arrive at the substrate can be altered by changing the pressure in the chamber, or by altering the substrate-to-target distance. In our system, at pressures below 0.01 mbar, the particulates will travel ballistically to the substrate, resulting in a deposition of the particulates as formed in the plume. At higher pressures, the plasma plume interacts with the background gas. In our case oxygen is used to oxidize the elements in the plasma-plume. The interaction results in a reduction of vacancies in the thin film.

Another parameter is the substrate temperature. For complex oxides, the substrate is often above 650 °C and can be heated to temperatures up to 900 °C. The elevated temperatures stimulate the adsorbed particulates to diffuse over the surface which

is essential for 2D growth. The diffusion (D_s) is governed by the following equation:

$$D_s = va^2 exp(-\frac{E_A}{k_B T}),\tag{2.4}$$

where v is the hopping frequency, a is the distance an atom hops on average, E_A the hopping energy, and k_b is the Boltzmann constant. A too low temperature results in the particulates sticking to the surface upon impact. This growth creates an amorphous 3D growth with a 'sputtered' or spray-painted structure. On the other hand, increasing the temperature too high results in an increased rate of sublimation. Different compounds in the thin film have different sublimation rates, influencing the final stoichiometry of the film. The most volatile elements in a mixture have, most likely, a lower melting point and will sublimate faster compared to the other elements present.

To control the growth process in the chamber, the film is *in situ* monitored by reflective high energy electron diffraction (RHEED).

RHEED

Reflective high energy electron diffraction (RHEED) is used in surface science to characterize the surface morphology of (crystalline) materials. Besides the crystal structure of the surface, RHEED can detect changes in surface roughness. When all parameters are kept constant, a change in roughness causes an intensity fluctuation. During growth the main interest is the crystallinity of surface layer, and the roughness. The crystallinity gives information about how well the material is growing, while the roughness is an indicator of how fast a layer is formed. With RHEED, both of these parameters are monitored based on accelerated electrons (30 kV) which arrive at a grazing incidence angle on the surface of the substrate. Similar to x-ray diffraction, the electrons diffract from the substrate surface, due to their wavelike properties, forming a pattern on a phosphor screen, as seen in figure 2.13 (a-c). A digital camera captures this diffraction image on the phosphor screen which stores information regarding the light intensity and the location of the diffraction spots.

The grazing incidence angle of the electron beam combined with the strong interaction of electrons with matter results in a low penetration depth. Therefore only information regarding the top layers of material is obtained with RHEED. The low penetration depth results in a unique patterns for different surface morphology, as shown in figure 2.13. The figure gives examples of different surface ordering, where (a) shows a smooth surface of a $[001]_{pc}$ oriented LaAlO$_3$ substrate. The smooth crystalline structure is represented by the 3 sharp diffraction spots and the Kikuchi lines. Figure 2.13 (b) and (c) are taken during growth of LSMO on LAO; where (b) shows a

2D film growth, distinguished by the streaky parallel pattern. Figure 2.13 (c) shows a 3D growth characterized by the many sharp RHEED spots.
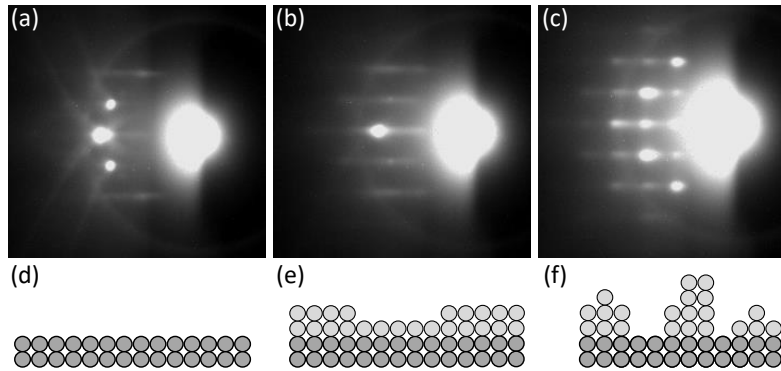
Figure 2.13: *(a) RHEED image of a smooth surface. (b) Streaky pattern characteristic for LSMO layer-by-layer growth. (c) A RHEED pattern observed when having 3D growth of LSMO on STO. (d-f) A sketch of a film which would show (a-c) as RHEED signal, respectively.*

2D growth, as shown in figure 2.13 (b), is characterized with streaks, due to the small film thickness. The diffraction in the reciprocal space is localized in the z-direction, which results in the electrons to diffuse to near infinity in the real space. The 3D growth shown in figure 2.13 (c) is from a polycrystalline film and is characterized by many diffraction spots. In general, all allowed diffraction spots are visible in 3D growth, showcasing the pseudo cubic nature of LSMO. The spots visible in 3D growth do not move when the substrate is rotated around its axis, while the spots in the other growth modes do move under rotation.

The roughness is monitored by measuring the peak intensity of the spots. Oscillations in intensity occur due to increase and subsequent decrease in roughness of the surface in layer-by-layer growth. As shown in figure 2.14 the diffraction has maximum intensity on a smooth surface due to a positive interference. Upon increasing the roughness, the diffraction patterns of the layers interfere destructively, lowering the maximum intensity of the peak. For a near perfect layer-by-layer growth only one layer is grown at any given time, resulting in a stable oscillation, with each oscillation having the same maximum and minimum intensity. In practice, for LSMO on LAO or LSMO on STO, the surface roughness increases overtime, which results in a lowering of the maximum intensity, minimum intensity, average intensity, as well as the oscillation amplitude. The increase in surface roughness will bring the oscillation amplitude to zero causing the growth mode to transition from layer-by-layer

to 3D growth.
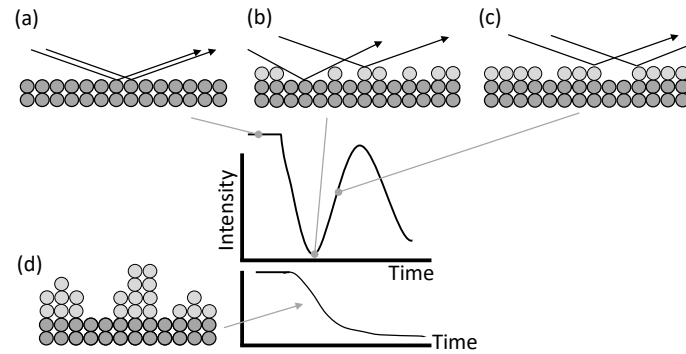
Figure 2.14: *The intensity of the RHEED spot varies depending on the rough-*
ness of the surface of the sample. For a layer-by-layer growth, of the
sample, intensity oscillates between multiple states. (a) At the start,
the atomically smooth layer will form a sharp RHEED spots with
high intensity. (b) During the initial growth of a layer the roughness
increases until the maximum step density (roughness is reached), re-
sulting in a wide and low intensity RHEED spot. (c) The growth of
the layer continues by filling in the gaps between the already formed
layer, therefore reducing the step density (roughness) of the layer,
resulting in an increasing intensity of the RHEED signal. Upon com-
pletion of one layer, the maximum intensity will be reached and the
cycle starts over from (a). (d) For island or 3D growth, the RHEED
intensity signal looks like a decaying function. The decay in intensity
is caused by the ever increasing roughness during growth.

2.2.2   Fabrication

After the growth of a thin film, the samples are first characterized by XRD and
SQUID and then the thin film is processed to fabricate Hall bars for magnetotrans-
port measurements. For the device fabrication, the sample is spin coated with
AZ5214E photoresist (indicated in red in figure 2.15), and subsequently covered
with a mask (indicated in grey) and exposed under UV light to create a pattern
in the film as shown in figure 2.15 (a) and (b), respectively. To develop the film, it is
submerged in OCD4262 for 1 minute, followed by rinsing it in demineralized water
for 15 seconds to remove the exposed photoresist. After development, the film is
partially covered with photoresist as shown in figure 2.15 (c). The next step is the

physical vapor deposition (PVD) of the contacts, by evaporating a layer of 5 nm titanium and 50 nm of gold as depicted in figure 2.15 (d). The evaporation of Ti and Au is performed in a TFC-2000, using an electron beam to heat the Ti and Au with a deposition rate of 1 Å/s at pressures below 1E-6 Torr. Subsequently the sample is submerged in warm (45 °C) acetone to remove the photoresist and the Ti/Au on top of the photoresist.

In the last stage, the Hall bars are etched from the thin film. In preparation for the etching, the steps shown in figure 2.15 (a), (b), and (c) are repeated. After step (c), the sample is submerged in aqua regia, a mixture of 1:3 mol of nitric acid (HNO_3) and hydrochloric acid (HCl), to remove the exposed thin film. The etch rate of LSMO in aqua regia is around 30 nm/s and etches the thin film within a second, therefore a quick dip suffices. After dipping the sample in aqua regia, the sample is rinsed in DI water, and the remaining photoresist is stripped off with warm (45 °C) acetone. After the described fabrication process, a LSMO film with gold contacts remains as shown in figure 2.15 (e) and is ready to be electrically connected.
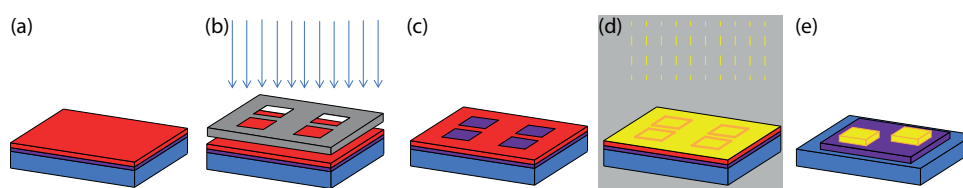
Figure 2.15: *Schematic drawings of (a) a spin coated thin film [purple] with AZ5214E photoresist [red] on top of a substrate [blue]. (b) Illustrates hard contact UV exposure of thin film. (c) After developing the photoresist. (d) PVD of Ti/Au [yellow] on the sample. (d) Final device with etched thin film and contacts.*

2.3 Characterization

Before growth, of a thin film some substrates are characterized in a magnetic property measurement system (MPMS) to make sure no magnetic impurities are present on the substrate. After thin film growth, the film is characterized with X-ray diffraction and again with a MPMS, to establish magnetic and structural properties of the thin film. After X-ray and MPMS characterization, the sample is etched into an Hall bar and the magnetotransport is investigated.

X-ray Diffraction

X-ray diffraction (XRD) is a common experimental technique in science to routinely determine or check the crystallographic properties of a material. Crystals or crystalline films are a regular array of atoms. When shining light on regularly spaced array, a predictable intensity pattern with high and low intensity appears. Lawrence and William Bragg discovered this interference phenomena in 1913 and postulated the Bragg's law:

$$n\lambda = 2d \sin(\theta), \tag{2.5}$$

where n is an integer number, λ the wavelength of the light, d the lattice spacing, and θ the angle between the scatter plane (surface) and the incident ray.

An analogy for describing the interference pattern is like throwing a body of water. The rock hitting the water generates radial moving waves. This is similar to the effect of a photon hitting an atom. When you throw two rocks into the water, the radial waves will generate regions with high and low intensity. The interference pattern in the secondary waves is similar to the interference pattern caused by X-rays in a crystal, where the location of constructive and destructive interference can be predicted with Bragg's law. In experiments, in general, not the entire 2D plane (like the water) is observed but only a single line. These experimental complications implies that a light source and a detector are moved along an angular path with respect to the sample. Shown in figure 2.16 (left) is a schematic diagram of such a measurement. An X-ray source shines light at an angle θ to the crystal consisting of regular spaced dots, at the same time the detector also is at the angle θ. The situation drawn, is a situation where the light scatters off the individual atoms and positively interferes as the atoms are regularly spaced apart. When atoms are not regularly spaced apart negative interference occurs and a low intensity signal is measured.

By moving the source and the detector over the angular path, a regular pattern of high and low intensities can be observed.In the case of a crystalline or epitaxial films on a substrate, the spacing between the atoms might be different compared to bulk. Therefore XRD is used to determine various factors for thin films like LSMO on LAO. First of all, XRD provides information regarding the crystallinity (whether or not the film has a crystal structure). Secondly, the lattice spacing of the film determines the strain on the film and thirdly, thickness of the thin film. Besides the afore mentioned features, the crystalline orientation and type of unit cell, are among the frequently studied parameters with XRD.

We typically take a single line scan (θ-2θ method) in our measurements to determine the out-of-plane crystal deformation. For a few samples, in depth reciprocal
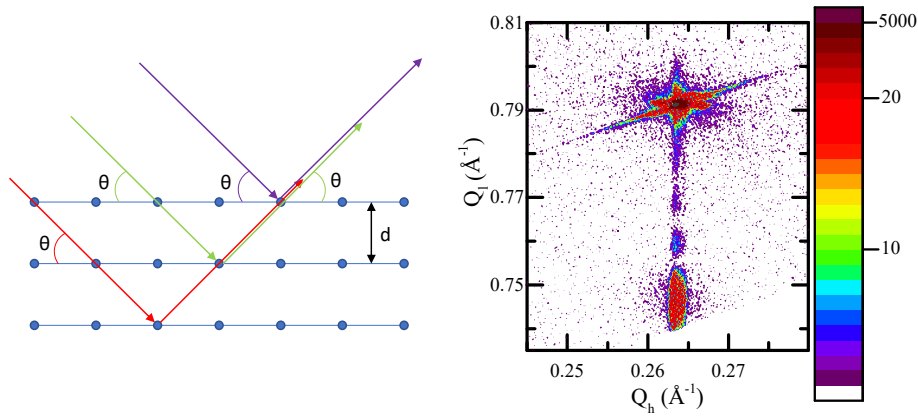
Figure 2.16: (left) Schematic drawing of Bragg's Law. (right) Example of the extracted data from an RSM measurement around the [103] peak of LAO.

space mapping (RSM) is performed which is, in essence, a series of line scans around a substrate peak while varying both ω and θ. Such an RSM measurement aids the interpretation of peak displacement and can give information about the inplane lattice deformation of thin films. An example of such a measurement is shown in figure 2.16 (right), wherein multiple peaks are observed. The horizontal alignment of the peaks indicates that the LSMO thin film unit cell is compressed and copies the inplane lattice constant of the LAO substrate.

Magnetic Property Measurement System

A Magnetic Property Measurement System (MPMS) is also referred to as a superconducting quantum interference device (SQUID) which is used for measuring changes in the magnetic flux of a sample. The magnetic flux gives information regarding the magnetization of the material in a given state. By varying the magnetic field strength and temperature, a wide range of magnetic effects can be observed in MPMS measurements, like Neel temperature, Curie temperature, blocking temperature, coercive field, and saturation magnetization. The magnetic flux is measured by oscillating the sample through a superconducting loop as shown in figure 2.17. By oscillating the (magnetic) sample through the superconducting loop, the magnetic flux generated by the magnetic sample generates a screening current in the supercon-

ducting loop. The screening current is proportional to the magnetic flux which, in turn, is related to the magnetization in the sample. To measure the screening current, a constant current is sent from one side of the superconducting loop to the other. In the middle, two Josephson junctions are added, where the screening current generated by the magnetic flux causes a phase change in the current which can be measured as a voltage drop over the superconducting loop.
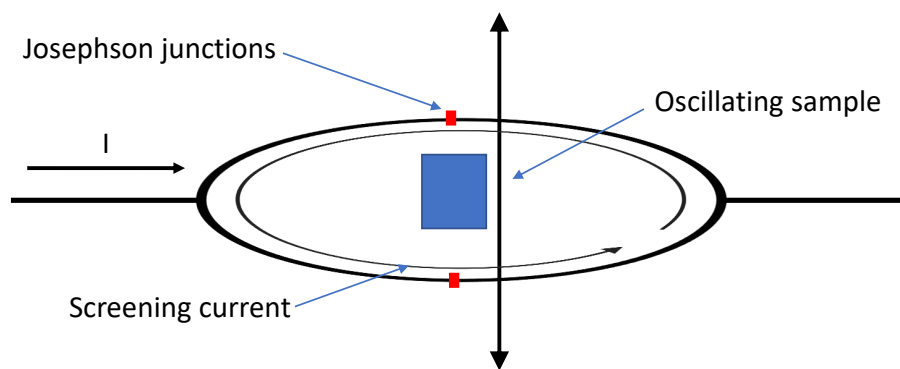
Figure 2.17: *A schematic drawing of the inner workings of the MPMS.*

The discussed characterization techniques are performed on the pristine film before any fabrication steps. For electrical transport measurements, an Hall bar is the ideal shape for measurements as its geometry allows for longitudinal as well as transverse measurements. In the next section, the electrical measurements are discussed. Firstly, the Hall bar structure with the electrical contacts is discussed, followed by the observed magnetotransport phenomena.

2.3.1 Magnetotransport Effects

For magnetotransport measurements, the Hall bar structure is used in this thesis. A Hall bar, as shown in figure 2.18, consists of at least six contacts. The two outermost contacts are used as a current probe while the four inner contacts are used for the voltage readings. In figure 2.18, the longitudinal as well as the transverse voltage contacts are indicated.

Using separate contacts for applying the current and measuring the voltage has an advantage that the interface resistance is not measured. For small devices, this
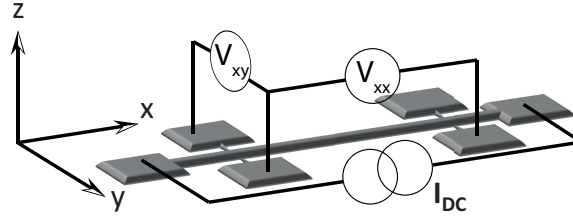
***Figure 2.18**: Drawing of a Hall bar with Cartesian coordinates as used in this thesis.*

interface resistance can be relatively high compared to the actual resistance of the sample. Secondly, using a Hall bar gives us the opportunity to measure the resistance in different crystallographic directions of the sample. The electrical transport in LSMO films is measured in a fourprobe configuration, in the equivalent [001] and [010] lattice direction of the thin film.

Electrical Transport in LSMO Films

Manganites are known for their large magnetoresistance effects due to a strong coupling between conduction and magnetism. The discovery of colossal magnetoresistance in manganites sparked a large research interest and was widely studied in the 90's of the last century. Among others, the field and temperature dependence of the electrical conductivity is studied with different techniques and models. For LSMO, three distinctly different phases are described and can be modeled by different resistivity models. Different resistive phases, such as the ferromagnetic metallic phase (FMM), paramagnetic insulating phase (PMI) and antiferromagnetic insulating phase (AFI) are modeled with eq. 2.6 and 2.7. In the low temperature regime, LSMO is in the ferromagnetic phases (FMM), caused by double-exchange hopping, leading to an orbital-disorded state which behaves like a metal and the resistivity can be fitted with an equation in the form,

$$\rho_{FMM} = \rho_0 + \rho_2 T^2 + \rho_{4.5} T^{4.5}, \tag{2.6}$$

where T is the temperature and ρ_0 is the resistivity due to temperature independent scattering. In general, ρ_0 decreases significantly under the influence of an applied magnetic field, believed to be due to an improved spin alignment at grain boundaries and domain walls. ρ_2 and $\rho_{4.5}$ are temperature dependent resistivity terms; where ρ_2 is associated with electron-electron scattering and $\rho_{4.5}$ with

electron-magnon scattering. The values of both these terms decrease when a magnetic field is applied.

In reality, the film is not in a single phase and the current model fails to account for the coexistence of ferromagnetic metallic and insulating behavior[33]. Other phases which can be found in the film are the AFI and PMI phases, which both increase the resistivity of the film. Strain in thin films of LSMO causes the transport mechanism to change from metallic double-exchange to (anti)ferromagnetic super-exchange conduction. Depending on the type of strain, tensile or compressive, the resulting orbital-ordered AFI phase is either A- or C-type, respectively. The insulating phases have the same conduction mechanism as the PMI phase.

Upon increasing the temperature, at a given temperature (T_{mit}), a metal to insulator transition can be observed ($T_{mit} = (\frac{d\rho}{dT})_{max}$). Above this temperature, an increasing fraction of the LSMO shows (paramagnetic) insulating behavior. The PMI phase of the material can be described by

$$\rho_{PMI} = \gamma T \exp\left(\frac{E_a}{k_B T}\right), \tag{2.7}$$

where E_a is the activation energy, k_B the Boltzmann constant, γ an empirical coefficient, and T is the temperature. The model indicates polaronic hopping as the main mode of transport in bulk LSMO, in which the activation energy is needed to facilitate an electron to hop from one Mn-ion to the next. Due to the strong localization of the polaronic electron in the t_{2g} orbital, the electron also exhibits the magnetic effects related to an unfilled 3d shell, important for magnetism-conduction coupling in the super-exchange conduction.

The transition from FMM to PMI is a gradual one. The depicted models resulting in equations 2.6 and 2.7 do not account for an overlapping of phases. This resulted in the need for fitting both phases separately, well below and well above the Curie temperature. To improve the model, equations 2.6 and 2.7 are combined in equation 2.8, such that the total resistance of the film can be fitted with a single equation, given by

$$\rho_{total}(T) = \rho_{FMM}(f) + \rho_{PMI}(1 - f) \tag{2.8}$$

where ρ is the resistivity of a phase and f is the volume fraction of the material in the FMM phase, consequently the remaining part of the volume will be in the PMI. The fraction f is governed by the Boltzmann distribution as

$$f_{FMM} = \frac{1}{1 + \exp\left[\frac{U_0(T/T_C^{model}-1)}{k_B T}\right]} \tag{2.9}$$
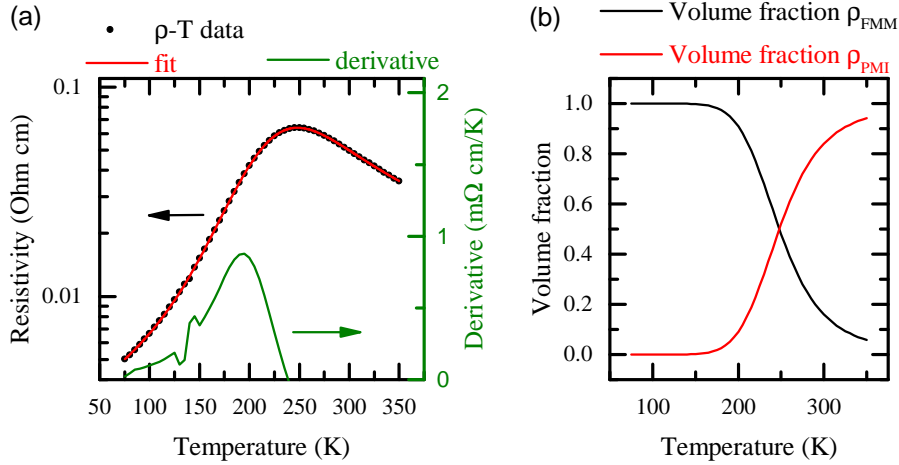
***Figure 2.19**: (a) Left axis depicts a typical ρ-T curve for LSMO grown on LAO where below 250 K, the LSMO is behaving according to ρ_{FMM} and above 250 K, the behavior is characterized by the ρ_{PMI}. Right axis depicts the derivative of ρ-T. The maximum derivative at 195 K represents the metal-to-insulator transition. (b) Volume fraction of LSMO FMM and PMI with temperature according to equation 2.8.*

where T_C^{model} is an empirical fitting parameter and U_0 is the energy difference between the FMM phase and PMI phase at 0 K. T_C^{model} should be close to the observed T_C and indicates the transition temperature from FMM phase to PMI phase[34]. Figure 2.19 (a) shows $\rho - T$ data, measured on an LSMO Hall bar grown on LAO substrate, fitted with equation 2.8. The resulting volume fraction is plotted in figure 2.19 (b). Application of a magnetic field will reduce the resistance of LSMO, giving rise to a novel magnetoresistance phenomena called colossal magnetoresistance.

Colossal Magnetoresistance

Colossal magnetoresistance (CMR) is an isotropic phenomena which describes the drastic change in resistance of a material upon applying a magnetic field. CMR is defined as:

$$CMR(B) = \frac{\rho(B) - \rho(0)}{\rho(0)} * 100\%, \qquad (2.10)$$

where $\rho(B)$ and $\rho(0)$ are the resistivity of material with and without application of a magnetic field, respectively. Most materials have a magnetoresistance effect, and in metals, for instance, it is known to increase the resistivity up to only a few percent. However, for doped manganites the resistivity decreases when a magnetic field is applied, resulting in a negative magnetoresistance. The decrease in resistivity can be of several orders of magnitude for manganites, therefore the mangnites have been extensively studied since the discovery of the negative CMR effect in manganites[35–37].

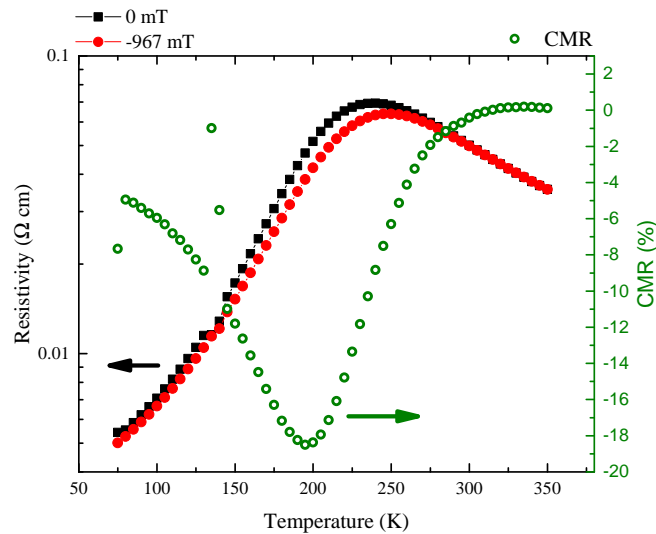

Figure 2.20: *Resistivity versus temperature (left axis) for an LSMO thin film. Measured with and without the application of a magnetic field. The difference in resistance is expressed with the CMR percentage (right axis).*

The phenomena of the negative CMR in manganite is explained based on the hopping of itinerant electrons in the Mn-ion e_g orbital. The double-exchange hopping, from Mn^{3+} to Mn^{4+}, is only possible when the spin states of the $Mn^{3+/4+}$-ions are aligned. Upon applying a magnetic field, the spin states align and the double-exchange hopping is possible, lowering the overall resistance of the manganite material. In manganite the CMR peaks close to the Curie temperature, as shown in figure 2.20, making the CMR peak-value a useful feature to determine the Curie temperature in transport measurements.
The isotropic nature of the CMR effect allows it to be separated from other phenomena, such as the anisotropic magnetoresistance (AMR).

Anisotropic Magnetoresistance

Anisotropic magnetoresistance (AMR) is found in a multitude of materials and is already observed over 150 years ago in materials like iron[36]. AMR is calculated using the resistance when the magnetization is parallel to the current $\rho(\|)_B$, and when orthogonal to each other $\rho(\perp)_B$. The resulting resistivity change is expressed in percentage, with the following equation:

$$AMR(B) = \frac{\rho(\|)_M - \rho(\perp)_M}{\rho(\perp)_M} * 100\%. \tag{2.11}$$

The magnetization for the AMR is set using an applied magnetic field (B). Therefore, often the M in equation 2.11 is often replaced with B, assuming the magnetization follows the magnetic field (B$\|$M when B>μ_0H$_{sat}$).
The origin of the effect was first worked out for metals and lies in the combination of spin-orbit interaction and the magnetization of the material, causing an angle-dependence in the scattering. The proposed two-current model by Mcguire and Potter describes the AMR effect due to spin-orbit interaction of electron-scattering in the s and d orbitals in metals[37]. Scattering from, for instance, impurities causes electrons to scatter from conduction orbitals into localized d-orbitals. The d-states are influenced by the applied magnetic field and spin-orbit coupling, consequently the angle between magnetic field and current influences the scattering rate. By taking different scattering processes into account, namely $s \uparrow \rightarrow s \uparrow, s \uparrow \rightarrow d \uparrow, s \uparrow \rightarrow d \downarrow$, $s \downarrow \rightarrow s \downarrow, s \downarrow \rightarrow s \downarrow$, and $s \downarrow \rightarrow s \uparrow$, where the $\uparrow$ and $\downarrow$ indicate the spin state, the resistance can be calculated for $\rho(\|)_M$ and $\rho(\perp)_M$. The AMR ratio for weak ferromagnet ($\rho_{s\uparrow} = \rho_{s\downarrow} = \rho_s$) is defined as:

$$\frac{\Delta\rho}{\rho} = \frac{\gamma(\rho_{s \rightarrow d\downarrow} - \rho_{s \rightarrow d\uparrow})^2}{(\rho_s + \rho_{s \rightarrow d\uparrow})(\rho_s + \rho_{s \rightarrow d\downarrow})}, \tag{2.12}$$

with $\gamma = 3/4(\lambda/B_{applied})^2$[38, 39]. When $\rho_{s \to d\uparrow} = 0$, Campbell, Fert and Jaoul's (CFT) expression for strong ferromagnets appears[38, 40]. Based on the CFT model and the two-current model, Kokado *et al*[41] proposed a more universal description of AMR which could correctly predict the sign of the AMR effect. The model replaces the s-orbital by σ as the conduction orbital and predicts that if either $s \downarrow \to d \downarrow$ or $s \uparrow \to d \uparrow$ scattering is dominant, the AMR ratio is negative. The latter is the case for $La_{0.67}Sr_{0.33}MnO_3$ as it is a half metal at 0 K, with only spin up states in the 3d-orbital. This results in an AMR ratio, given by[41]:

$$\frac{\Delta\rho}{\rho} = \frac{-\gamma}{(\rho_{s\uparrow \to d\uparrow}/\rho_{s\uparrow})^{-1} + 1}. \tag{2.13}$$

Plugging in realistic numbers for LSMO gives an AMR of -0.4 %[41], which is in close correspondence to the values we observed for AMR in chapter 4, suggesting that angle dependent scattering due to spin-orbit coupling is the driving factor.

A more intuitive explanation for the AMR is based on the anisotropy energy[37]. For this we need to separate the AMR into two parts, a non-crystalline part and a crystalline part, as the theory is based on a polycrystalline sample. Equation 2.11 refers to the non-crystalline part reflecting the differences in the scattering between M∥I and M⊥I in the resistance matrix. The difference in scattering between electrons with momentum parallel to and orthogonal to the applied magnetic field, is due to relativistic spin-orbit coupling [42]. In angle-dependent magnetoresistance studies, as performed in this thesis, the noncrystalline AMR is visible in the transport measurements as a $sin^2(\theta)$ or $cos^2(\theta)$ oscillation, depending on whether the magnetoresistance is positive or negative, respectively. The non-crystalline AMR is given by [37]:

$$E = A_0 + A_1 cos^2(\theta), \tag{2.14}$$

where A_0 and A_1 are energy anisotropy constants which depend on factors such as magnetization, and applied magnetic field, and θ is the angle between current and applied magnetic field, assuming B∥M. The cosine originates due to multiplication of the magnetization and magnetic field vectors and is maximum when both are parallel and zero when orthogonal as shown in figure 2.21.
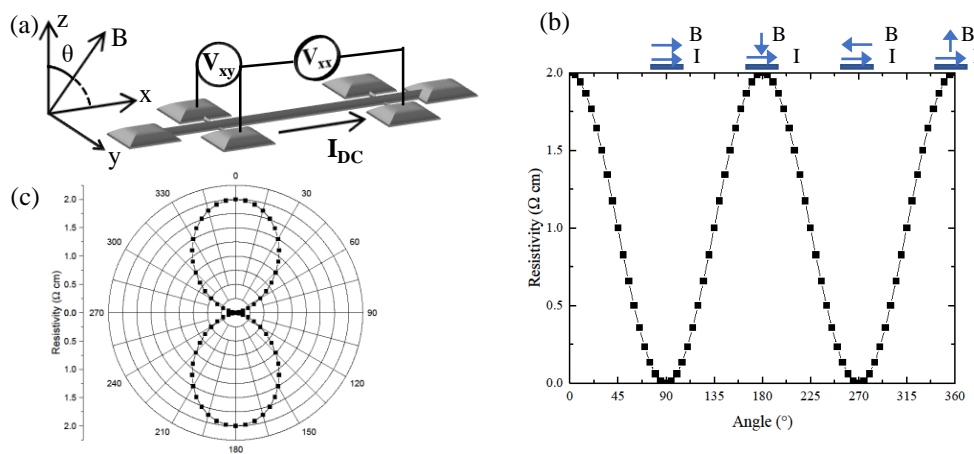
Figure 2.21: *(a) Hall bar with the current and field directions as indicated. (b) The ideal curve for AMR. (c) AMR plotted in a polar plot showing the twofold symmetry.*

The interplay with other factors, such as crystal-structure, are not taken into account by this polycrystalline model but will have an effect on the system. The crystalline component depends on properties like crystal symmetry[43], leading to higher order symmetries.

Magnetocrystalline Anisotropy

Magnetocrystalline anisotropy (MCA), similar to AMR, is observed when rotating the magnetic field around a sample, either inplane or out-of-plane, while measuring the resistance. Since the sample is crystalline, the angle dependence can be related to the crystallographic directions in the sample. Figure 2.22 shows an rotating magnetic field around a unit cell of $La_{0.67}Sr_{0.33}MnO_3$.
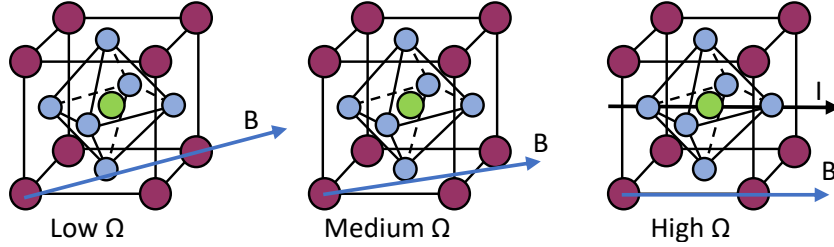
Figure 2.22: $La_{0.67}Sr_{0.33}MnO_3$ *unit cell with an applied magnetic field in the [110] (left side) [210] (middle) [100] direction, having a low/medium/high resistance, respectively. The current is in the [100] direction, as drawn in the right figure, for all three cases as drawn.*

In its origin, the effect is based on electron scattering being influenced by spin-orbit interaction interacting with the crystal structure of the material. Localized electrons in the atomic orbitals interact with the magnetic field. Depending on the occupied orbitals the coupling with magnetic field will cause a change in the relativistic electron scattering matrix[43], which in turn results in a change in resistance. Depending on the symmetry of the crystal structure, band structure and orbital symmetry, MCA might contribute to the angle-dependent magnetotransport signal. For LSMO, the crystal structure is pseudo-cubic, giving rise to a fourfold signal, expanding the energy equation 2.14 to

$$E = A_0 + A_1 cos^2(\theta) + A_2 cos^4(\theta), \tag{2.15}$$

where the last term is added for the fourfold signal, and A_2 is an energy constant depending on various parameters. Figure 2.23 depicts the observed fourfold magnotoresistance signal, where the clover leaf shape in the left figure is a characteristic of the MCA signal in a cubic symmetry.

The MCA can be tuned by utilizing extrinsic as well as intrinsic properties such as exchange bias (gate voltage), or by altering the valence state of ions[44]. Both gating and changing the valence state aim to change the band structure, where the manipulation of MCA with application of gating has recently gained scientific interest[45–49].

Other effects like shape anisotropy can also play a role in the angle dependent measurements. Shape anisotropy is the demagnetization energy re-orienting magnetic domains to create closed flux lines. The extent to which this happens depends
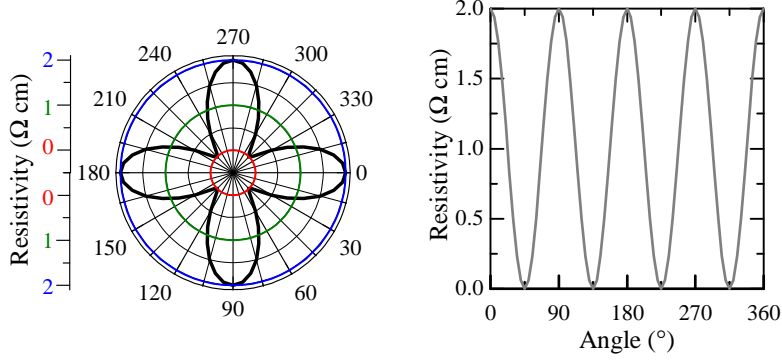
Figure 2.23: *An example graph depicting fourfold magnetocrystalline anisotropy in a polar plot (left) and conventional graph (right). The red, green and blue circles of the left figure correspond to 0, 1, and 2 value on the y-axis of the left figure.*

on the shape of the material. The bigger the sample in all three dimensions, the less is the influence of the demagnetization term. For thin films, this effect plays a role while performing out-of-plane measurements, as the demagnetization energy causes the material to have a preferred inplane magnetization to created closed flux lines. For the inplane rotations, the shape anisotropy is neither expected nor observed to play a large role as the Hall bars are relatively large, 50 μm by 3 mm, compared to their thickness (∼5-25 nm). If shape anisotropy would occur in the inplane direction, the easy axis would lie along the Hall bar giving rise to an uniaxial (twofold) signal.

Magnetoresistance Fitting

In the itinerant ferromagnet LSMO, the electrical conduction and magnetization are coupled due to the double-exchange mechanism. The strong coupling between the phenomena leads to a resistance change due to the previously discussed CMR and AMR effects. The longitudinal resistivity can be derived from equation 2.15, to be given by[45]:

$$\rho_{long} = \rho_0 + \rho_{2f} \cos\left(2\theta - \delta_{2f}\right) + \rho_{4f} \cos\left(4\theta - \delta_{2f} - \delta_{4f}\right), \qquad (2.16)$$

where the longitudinal resistivity, ρ_{long}, depends on a baseline resistance ρ_0, and on two cosine-modulated functions, with amplitudes ρ_{2f} and ρ_{4f}. The terms δ_{2f} and

δ_{4f} are offsets to fit the cosines to the oscillation. Without offsets, the cosines would peak at 0 degree. This offset can arise due to a mismatch between applied magnetic field, current direction, and crystallographic axis. Thermal drift has been an issue, especially close to and above Curie temperature, in the thin films. For this reason, the thermal drift behavior was studied and an extra exponential term was added to equation 2.16, to compensate for the thermal drift. Resulting in the following equation:

$$\rho_{long} = \rho_0 + \rho_{2f} \cos\left(2\theta - \delta_{2f}\right) + \rho_{4f} \cos\left(4\theta - \delta_{2f} - \delta_{4f}\right)$$
$$+ \rho_{drift} \exp\left[-(360 + \theta)/\tau_0\right], \tag{2.17}$$

where ρ_{drift} and τ_0 are fitting parameters. Figure 2.24 shows obtained data from an inplane rotational measurement fitted with equation 2.17.
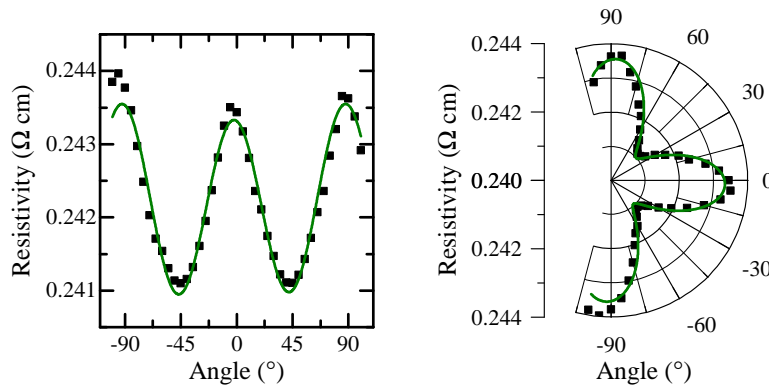
Figure 2.24: *(Left side) Graph with measured angular dependent magnetoresistance data (black squares) fitted with equation 2.17. (Right side) Polar plot with the same data and same fit, showcasing the fourfold symmetry observed in our low temperature measurements.*

Equation 2.17 is used for fitting all angle-dependent data in chapters 4 and 5. In chapter 4, the angle θ rotates inplane and is relative to the crystallographic [001] axes of the substrate. In chapter 5, the angle θ rotates out-of-plane and is also relative to the crystallographic [001] axes of the substrate.

References

[1] V. M. Goldschmidt, "Die Gesetze der Krystallochemie", Naturwissenschaften **14**, 477 (1926).

[2] H. A. Jahn, E. Teller, and F. G. Donnan, Proc. R. Soc. Lond., A Math. phys. sci. **161**, 220 (1937).

[3] T. Gao, X. Zhang, W. Ratcliff, S. Maruyama, M. Murakami, A. Varatharajan, Z. Yamani, P. Chen, K. Wang, H. Zhang, R. Shull, L. A. Bendersky, J. Unguris, R. Ramesh, and I. Takeuchi, Nano Lett. **17**, 2825 (2017).

[4] A. Marques, *Advanced si pad detector development and SrTiO3 studies by emission channeling and hyperfine interaction experiments*, Doctoral dissertation, Universidade de Lisboa, Lisbon (2009).

[5] L. Wu, J. Ma, J. Ma, Y. Zhang, Y. Gao, Q. Zhang, M. Liu, and C.-W. Nan, Sci. Bull. **61**, 157 (2016).

[6] C. Adamo, X. Ke, H. Q. Wang, H. L. Xin, T. Heeg, M. E. Hawley, W. Zander, J. Schubert, P. Schiffer, D. A. Muller, L. Maritato, and D. G. Schlom, Appl. Phys. Lett. **95**, 112504 (2009).

[7] S. Chromik, V. Strbik, E. Dobrocka, A. Dujavova, M. Reiffers, J. Liday, and M. Spankova, Appl. Surf. Sci. **269**, 98 (2013).

[8] H. Boschker, J. Kautz, E. P. Houwman, W. Siemons, M. Huijben, D. H. A. Blank, G. Koster, A. Vailionis, and G. Rijnders, Phys. Rev. Lett. **109** (2012).

[9] S. Chen, S. Wei, F. Jin, S. Ke, X. Zeng, L. Chen, and C. Huang, Ceram. Int. **44**, 13695 (2018).

[10] Z. Liao, M. Huijben, Z. Zhong, N. Gauquelin, S. Macke, R. J. Green, S. Van Aert, J. Verbeeck, G. Van Tendeloo, K. Held, G. A. Sawatzky, G. Koster, and G. Rijnders, Nat. Mater. **15**, 425 (2016).

[11] E. P. Houwman, G. Maris, G. M. De Luca, N. Niermann, G. Rijnders, D. H. A. Blank, and S. Speller, Phys. Rev. B **77**, 184412 (2008).

[12] J. Zhang, X. Chen, Q. Zhang, F. Han, J. Zhang, H. Zhang, H. Zhang, H. Huang, S. Qi, X. Yan, L. Gu, Y. Chen, F. Hu, S.-S. Yan, B.-G. Liu, B. Shen, and J. Sun, ACS Appl. Mater. Interfaces **10**, 40951 (2018).

[13] H. Sharma, H. Bana, A. Tulapurkar, and C. V. Tomy, Mater. Chem. Phys. **180**, 5 (2016).

[14] A. Ohtomo and H. Y. Hwang, Nature **427**, 423 (2004).

[15] D. W. Kim, D. H. Kim, C. Choi, K. D. Lim, T. W. Noh, D. R. Lee, J. H. Park, and K. B. Lee, J. Korean Phys. Soc. **36**, 444 (2000).

[16] A. J. H. van der Torren, S. J. van der Molen, and J. Aarts, Phys. Rev. B **91**, 245426 (2015).

[17] H. A. Kramers, Physica **1**, 182 (1934).

[18] P. W. Anderson, Phys. Rev. **79**, 350 (1950).

[19] J. B. Goodenough, Phys. Rev. **100**, 564 (1955).

[20] J. B. Goodenough, J. Phys. Chem. Solids **6**, 287 (1958).

[21] J. Kanamori, J. Phys. Chem. Solids **10**, 87 (1959).

[22] C. Zener, Phys. Rev. **82**, 403 (1951).

[23] H. Fujishiro, T. Fukase, and M. Ikebe, J. Phys. Soc. Jpn **67**, 2582 (1998).

[24] W. Heisenberg, Z. Physik **49**, 619 (1928).

[25] N. Greeves, *Chemtube3d*, https://www.chemtube3d.com/orbitals-d/.

[26] *Bayville chemical supply company inc*, https://www.bayvillechemical.net/lanthanum-aluminate-single-crystal, 2021-04-08.

[27] R. Gunnarsson, A. S. Kalabukhov, and D. Winkler, Surf. Sci. **603**, 151 (2009).

[28] D. A. Schmidt, T. Ohta, Q. Yu, and M. A. Olmstead, J. Appl. Phys. **99**, 113521 (2006).

[29] R. J. Francis, S. C. Moss, and A. J. Jacobson, Phys. Rev. B **64**, 235425 (2001).

[30] Z. L. Wang and A. J. Shapiro, Surf. Sci. **328**, 159 (1995).

[31] J. Yao, P. B. Merrill, S. S. Perry, D. Marton, and J. W. Rabalais, J. Chem. Phys. **108**, 1645 (1998).

[32] K. van Benthem, C. Elsässer, and R. H. French, J. Appl. Phys. **90**, 6156 (2001).

[33] A. A. Burema, J. J. L. van Rijn, and T. Banerjee, J. Vac. Sci. Technol. A **37**, 021103 (2019).

[34] L. Yin, C. Wang, Q. Shen, and L. Zhang, RSC Advances **6**, 96093 (2016).

[35] X. G. Chen, J. B. Yang, Y. B. Yang, C. S. Wang, S. Q. Liu, Y. Zhang, J. Z. Han, and Y. C. Yang, J. Appl. Phys. **115**, 043904 (2014).

[36]W. Thomson, Proc. R. Soc. Lond. **8**, 546 (1857).

[37]T. McGuire and R. Potter, IEEE Trans. Magn. **11**, 1018 (1975).

[38]A. P. Malozemoff, Phys. Rev. B **32**, 6080 (1985).

[39]A. P. Malozemoff, Phys. Rev. B **34**, 1853 (1986).

[40]I. A. Campbell, A. Fert, and O. Jaoul, J. phys., C, Solid state phys. **3**, 95 (1970).

[41]S. Kokado, M. Tsunoda, K. Harigaya, and A. Sakuma, J. Phys. Soc. Jpn **81**, 024705 (2012).

[42]I. Fina, X. Marti, D. Yi, J. Liu, J. H. Chu, C. Rayan-Serrao, S. Suresha, A. B. Shick, J. zelezny, T. Jungwirth, J. Fontcuberta, and R. Ramesh, Nat. Commun. **5**, 4671 (2014).

[43]D. J. Groenendijk, N. Manca, J. de Bruijckere, A. M. R. V. L. Monteiro, R. Gaudenzi, H. S. J. van der Zant, and A. D. Caviglia, Eur. Phys. J. Plus **135**, 627 (2020).

[44]D. Yi, J. Liu, S.-L. Hsu, L. Zhang, Y. Choi, J.-W. Kim, Z. Chen, J. D. Clarkson, C. R. Serrao, E. Arenholz, P. J. Ryan, H. Xu, R. J. Birgeneau, and R. Ramesh, Proc. Natl. Acad. Sci. U.S.A. **113**, 6397 (2016).

[45]Y. Bason, J. Hoffman, C. H. Ahn, and L. Klein, Phys. Rev. B **79** (2009).

[46]H. Boschker, M. Mathews, P. Brinks, E. Houwman, A. Vailionis, G. Koster, D. H. A. Blank, and G. Rijnders, J. Magn. Magn. Mater. **323**, 2632 (2011).

[47]Y. Gao, J. Zhang, X. Fu, G. Cao, and H.-U. Habermeier, Prog. Nat. Sci. Mater **23**, 127 (2013).

[48]L. D. Anh, N. Okamoto, M. Seki, H. Tabata, M. Tanaka, and S. Ohya, Sci. Rep. **7**, 8715 (2017).

[49]L. D. Anh, T. Yamashita, H. Yamasaki, D. Araki, M. Seki, H. Tabata, M. Tanaka, and S. Ohya, Phys. Rev. Appl. **12**, 041001 (2019).

Chapter 3

Temperature dependence of the magnetization of La$_{0.67}$Sr$_{0.33}$MnO$_3$ thin films on LAO$_3$

Abstract

We report on the interplay between magnetically ordered phases with temperature and magnetic field across compressively strained interfaces of thin La$_{0.67}$Sr$_{0.33}$MnO$_3$ films on LaAlO$_3$ substrates. From the temperature dependence of the magnetization and resistivity studies, we find two distinct temperature regimes, where this interplay is clearly exhibited. We ascribe this to the strain induced Jahn-Teller-like distortion that favors the stabilization of the d$_{3z^2-r^2}$ orbitals and enhances superexchange between adjoining Mn atoms. The temperature and field sweep of the magnetization and electronic transport lead to a hybridization between the closely spaced energy levels of d$_{3z^2-r^2}$ and d$_{x^2-y^2}$ orbitals leading to the coexistence of ferromagnetic and antiferromagnetic phases. Such an observation, not reported earlier, offers new routes for the design and study of magnetic textures in variously strained interfaces between perovskite oxides.

3.1   Introduction

Substrate engineering at perovskite heterointerfaces through strain, termination control or oxygen octahedral coupling has emerged as a promising routes to stabilize novel physical properties in these materials.[1–11] For example, it has been shown that the induced epitaxial strain arising at different substrate interfaces with thin films of the same magnetic oxide can lead to the occurrence of diverse magnetic phases.[12] The epitaxial strain induced distortion of the oxygen octahedron in ABO$_3$ perovskite thin films leads to anisotropic hopping between different BO$_6$ orbitals and thus to differences in magnetic ordering in-plane and out-of-plane of the film.[13] For a compressively strained interface ($a < c$), an out-of plane ferromagnetic ordering and an in-plane antiferromagnetic ordering are usually favored, while the reverse is true for a tensile strained interface, whereas for an unstrained

interface (a $\sim$ c), a three dimensional ferromagnetic ordering can be stabilized. Lattice distortions at engineered interfaces are thus strongly coupled with magnetic properties and can lead to an anisotropy of magnetization along different crystalline directions or to a distribution of different magnetically ordered phases in magnetic films.

$La_{0.67}Sr_{0.33}MnO_3$ (LSMO) is a canonical ferromagnetic oxide in the manganite family whose application potential is driven by unique physical properties as well as its relatively high Curie temperature.[14] Besides its large colossal magnetoresistance and demonstration of 100% spin-polarized carriers,[15–22] it has also been used in different electronic and spintronic devices such as in magnetic tunnel junctions, hot-electron based transistors[23] as well as in ferroelectric tunnel junctions.[24] The rich phase diagram of LSMO and the strong coupling between magnetic and electronic phases in thin LSMO films on different substrates [25] such as SrTiO$_3$, [3, 4, 26] NdGaO$_3$,[27] DyScO$_3$[12] and $(LaAlO_3)_{0.3}$-$(SrAl_{0.5}Ta_{0.5}O_3))_{0.7}$ (LSAT)[4] have been widely investigated. However, less is known about the coupling between magnetic and electronic properties in strained thin films of LSMO on a twinned LaAlO$_3$ (LAO) (100) oriented substrate. In this work, we study the interplay between coexisting magnetically ordered phases with temperature and magnetic field across compressively strained interfaces of thin LSMO films on LAO. We employ magnetization studies and electronic transport for this and find such an interplay to be active at different temperature regimes. These findings are further corroborated with the temperature dependence of the resistivity with and without an applied magnetic field across the heterointerface. Our findings indicate that the compressive strain rendered at such film-substrate interfaces lead to the stabilization of the d$_{3z^2-r^2}$ orbitals and to the coexistence of ferromagnetic and antiferromagnetic phases. The latter is a consequence of the stretching of Mn-O-Mn bond lengths and bond angles at the interface, altering the overlap between the MnO$_6$ orbitals. This coupling between the spin and orbital degrees of freedom at such engineered interfaces offers interesting prospects for the design and study of new magnetic textures at such interfaces.

3.2 Fabrication and structural characterization

3.2.1 Thin Film Growth

The 15 unit cell (u.c.) thick LSMO film is grown using Pulsed Laser Deposition (PLD) on a 5x5 mm LAO substrate. Optical microscope image shows a twinned surface, typical of a LAO substrate. Additionally, the twinned surface of LAO is visualized by Atomic Force Microscopy (AFM), as shown in Fig. 3.1. From these

observations, we find the twinning width to be several microns whereas the length ranges from tens to hundreds of micrometers. The highest and lowest point of the twinned plane is found to be up to 20 nm in height. The size of the twins is smaller than the Hall bar (100 by 3000 μm) and the Hall bar includes tens to hundreds of twins.
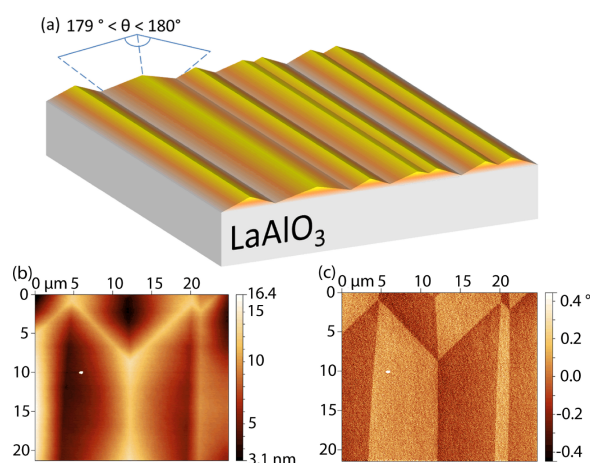
Figure 3.1: *(a) A schematic of the top surface of a twinned LAO substrate (not to scale). The angle between the two faces of a typical twin boundary is indicated. (b) The AFM image shows twinning of a LAO substrate. The twinning varies in width between 1 μm and 7 μm and is tens to hundreds of microns long. The height of a twin is between 5 nm and 20 nm, hence three orders of magnitude smaller compared to the width. The resulting tilting angle of two faces on either side of the twin boundary is between 179° and 180°. (c) The phase image of the figure clearly shows the contrast of the twin faces on either side of the boundary.*

The depositions were done in a Twente Solid State Technology PLD system with an excimer (KrF) laser (248 nm), at 750 °C under a pure oxygen pressure of 35 Pa. A laser fluence of 2 J/cm^2 at a frequency of 1 Hz is used with an oxygen flow of 1 cm^3/s and a pressure of 35 Pa in the PLD chamber. The deposition is monitored using an *in situ* Reflection High-Energy Electron Diffraction (RHEED) system. The RHEED spots are captured every 795 ms. Figure 3.2(a) shows post-deposition processing of the RHEED images for the analysis of the RHEED oscillations. This analysis provides information on the thickness of the film, considering one RHEED oscillation to correspond to the growth of one monolayer of LSMO. From the RHEED

image, 15 oscillations are seen, establishing that a 15 u.c. thick LSMO film is grown on top of LAO. After deposition, the sample is cooled down at a rate of 10 °C/min to room temperature, under an oxygen pressure of 1 kPa in order to anneal the film. The post-deposition annealing of the LSMO minimizes oxygen vacancy related defects.

3.2.2 Thin film characterization

The structural and magnetic properties of the film are characterized by X-Ray Diffraction (XRD) (PANalytical) and magnetic property measurement system (Quantum design) measurements. The XRD 2θ scan of the (001) and (002) peaks shows a 2.1% out-of-plane tensile strained LSMO film on top of the LAO substrate as shown in Fig. 3.2(b).
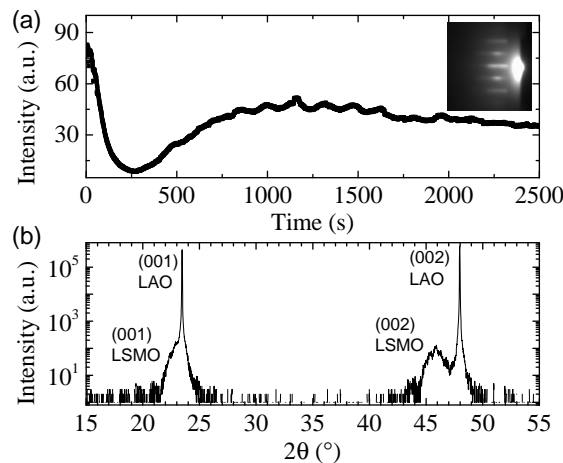
Figure 3.2: (a) The RHEED intensity oscillations of the first diffraction spot. The inset shows the RHEED spots, 5 min after the deposition of LSMO and is used to obtain the RHEED oscillations. The displayed intensity oscillations originate from the central spot. Analysing the RHEED intensity, 15 oscillations are visible establishing that 15 u.c. of LSMO are deposited on the LAO substrate. (b) XRD of a LSMO thin film on LAO. The intensity peaks correspond to the (001) and (002) peaks from LSMO and LAO. The absence of peaks in other reciprocal crystal directions suggest epitaxial growth of the film. A 2.1% out-of-plane lattice strain is determined, comparing the extracted lattice parameter of 0.396 nm with that of the bulk value of 0.388 nm.

We used the same figure (Fig. 3.2b) and fitted the LSMO (002) Bragg peak and the fringe on the left side of the peak to confirm the thickness of 15 u.c.. In the XRD 2θ scan with $\omega=0$, only [00l] peaks are visible, suggesting that the film is grown epitaxially in the out-of-plane direction.

The magnetic property measurement system is used to perform magnetization measurements with temperature and applied magnetic field. In Fig. 3.3, the magnetization dependence on applied field is shown, where the magnetic field is swept both in-plane and out-of-plane with respect to the sample surface. The field dependent loops show ferromagnetic behavior. The coercive field of 43 mT at 10 K is similar for in-plane and out-of-plane measurements, indicating weak anisotropy. The highest saturation magnetization (M_s) is determined to be 570 emu/cm^3 at 2 T for 10 K.
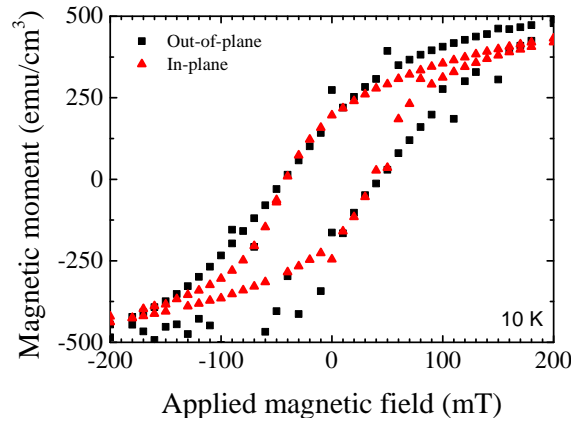
Figure 3.3: *The magnetization with respect to the applied magnetic field for out-of-plane (square) and in-plane (up-triangles) field directions. The ferromagnetic loops at 10 K have similar coercive fields. Initially, a magnetic field of -2 T is applied, thereafter it is swept to 2 T and back to -2 T. Between the out-of-plane and in-plane measurements, the film is warmed above the Curie temperature. The saturation magnetization (M_s) of 570 emu/cm^3 is determined from the full loop (not shown).*

The magnetization versus temperature, shown in Fig. 3.4, represents the Zero Field Cooling (ZFC) and two Field Cooled Warming (FCW) measurements. From

the curves, two magnetic phase transition temperatures are extracted, around 230 K and 85 K. The maximum magnetization is reached around 130 K for the ZFC in-plane curve. Below 130 K the magnetization decreases for the in-plane component while the out-of-plane magnetization increases around 100 K. The in-plane magnetization deviates from a typical ferromagnetic behavior for LSMO films on LAO. The magnetization curves are an indication of an interplay between different magnetic phases in the film with temperature and the cooling field.
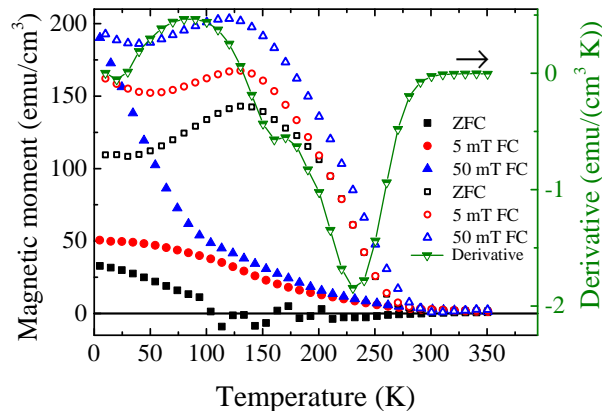
Figure 3.4: *The magnetization, on the left axis, is measured during heating after cooling down to 10 K. The closed symbols correspond to the out-of-plane magnetization, while the open symbols correspond to the magnetization in-plane. A measuring field of 5 mT was applied. In addition to the ZFC measurement, FCW experiments were performed with cooling fields of 5 mT and 50 mT. The Curie temperature, defined as the lowest point in the derivative, on the right axis, is at 230 K, which is lower than reported bulk values. The plotted derivative is taken from the ZFC in-plane measurement. A second phase transition is observed at 85 K. The out-of-plane (closed symbols) show decreasing magnetization with temperature and reaches a negligible value around 100 K.*

The in-plane magnetization shows a clear ferromagnetic phase between 130 K and 270 K. At lower temperatures, the magnetization decreases, suggesting the presence of an antiferromagnetic phase. The ZFC plots for the out-of-plane direction show the occurrence of spontaneous magnetic moments below 130 K. The 50 mT and 5 mT FCW out-of-plane magnetization plots show a similar trend between

130 K and 270 K, however, below 130 K the 50 mT FCW out-of-plane magnetization increases significantly. From the trends observed for ZFC plots at 130 K, we infer an interplay between coexisting ferromagnetic and antiferromagnetic phases. The 50 mT FCW measurements show that this cooling field is sufficient to order the existing ferromagnetic phase in the out-of-plane direction.

3.3 Magnetotransport

In addition to the bulk film properties, magnetotransport measurements are performed in a Hall bar geometry. The Hall bar geometry is created using UV-lithography followed by wet etching in aqua regia to etch LSMO, using an established protocol.[28] A schematic of the Hall bar is shown in the inset of Fig. 3.5.

For the longitudinal resistivity measurements, the field is set to either 0 T or 1 T, in the z-direction, and a direct current of 5 μA is applied. By sweeping the temperature from 25 K to 240 K and simultaneously measuring the longitudinal voltage, the temperature dependence of the longitudinal resistivity is determined and plotted in Fig. 3.5. The resistivity measurements show an insulating trend below 130 K, which is expected for a 15 u.c. thin film LSMO [29] on LAO.[26] In the temperature range between 145 K and 210 K, both the ZFC and 1 T curve show a regime where the conduction is metallic. This indicates that there is phase coexistence in the material below 130 K and corroborates with our findings from M-T measurements.

From Fig. 3.5, we observe two distinct resistivity regimes with temperature. For temperatures between 25 K to 85 K, the resistivity changes from weakly insulating to metallic, while above 85 K, the LSMO film resistivity changes from metallic to weakly insulating. The resistivity increase in the low temperature regime is reminiscent of an antiferromagnetic phase, which, as suggested from earlier works [12, 25, 30] can occur under different growth conditions of the LSMO film or for different choices of the underlying substrate.

At higher temperatures, the resistivity of LSMO, transiting from metallic to insulating corresponds to the commonly observed magnetic phase transition from a ferromagnetic metal to a paramagnetic insulating phase.[17–20]

The applied magnetic field of 1 T is larger than the magnetic saturation field and is expected to align all spins that are in the ferromagnetic state. This will also lead to an overall decrease of the resistivity. This reflects the strong coupling between magnetic and electronic states in manganite thin films. This reflects the strong coupling between magnetic and electronic states in manganite thin films. The resistivity studies also matches well with the M-T findings discussed earlier. From the derivative
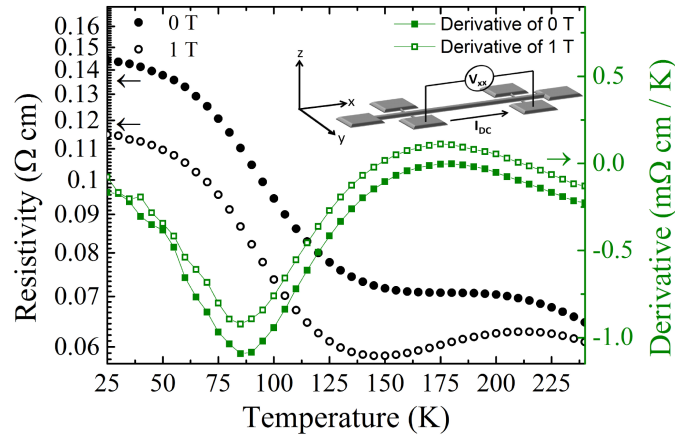
Figure 3.5: *Temperature dependence of the resistivity, left axis, for the 15 u.c. LSMO film with and without a magnetic field (1 T) and with a direct current of 5 μA. The temperature dependence of the derivative of the resistivity, with and without a magnetic field (1 T), is shown in the right axis. From the derivative plots two phase transition temperatures at 85 K and at 175 K are determined. (Inset) A schematic of the Hall bar with spatial definitions. The field is applied in the positive z-direction and current is applied in the positive x-direction.*

plots two phase transition temperatures at 85 K and at 175 K are determined.

3.4   Discussion

Both the temperature dependence of magnetization and resistivity shown in Fig. 3.4 and Fig. 3.5 respectively suggest phase coexistence in our thin films.[2, 12] Phase coexistence in tensile strained LSMO films deposited on $DyScSr_{0.3}$ accompanied by a phase transition from ferromagnetic to A-type antiferromagnetic behavior with changing temperature was reported earlier.[12] Moreover, earlier works utilizing x-ray absorption spectroscopy have reported on the observation of C-type antiferromagnetism in ultrathin films of LSMO on LAO and its insulating behavior.[30] However, for compressively strained thin LSMO films on LAO substrates, such as in our case, a phase coexistence has not been reported earlier. Our findings show the interplay between ferromagnetic metal and an antiferromagnetic insulator with temperature and applied magnetic field.

Epitaxial growth of strained LSMO thin films on LAO substrate causes a deformation of the pseudo-cubic structure, elongating the crystal in the [001] direction and compressing it in the [100] and [010] directions. The strain resulting in a Jahn-Teller-like distortion,[31] favors the stabilization of the $d_{3z^2-r^2}$ orbital over $d_{x^2-y^2}$ orbitals for compressively strained films.[14] Since the Mn-O-Mn bond angles and bond lengths are modified at such strained interfaces, this alters the overlap between the MnO_6 orbitals. The favorable occupation of the $d_{3z^2-r^2}$ orbital rather than the $d_{x^2-y^2}$ orbital induces low hopping probability via double exchange and enhances superexchange between Mn atoms, favoring an antiferromagnetic orientation of the spins and this is captured in Fig. 3.4. The dominant ferromagnetic phase observed in many thicker films of LSMO on LAO,[32] originates from the well-described double exchange between the Mn atoms. We find from both Fig. 3.4 and Fig. 3.5, the presence of insulating antiferromagnetic phase below 130 K and a dominant ferromagnetic phase between 130 K and 270 K. For such Jahn-Teller like distorted heterointerfaces, the thermal energy is sufficient to induce hybridization between $d_{3z^2-r^2}$ and $d_{x^2-y^2}$ orbitals due to their relatively close-spaced energy levels, leading to the observation of the interplay between the two magnetically ordered phases with temperature and applied field.

3.5 Conclusion

Strain engineered interfaces of thin LSMO films on LAO were studied using magnetization and electronic transport measurements. Two distinct temperature regimes are observed that are associated with an antiferromagnetic and a ferromagnetic phase. Such a coexistence of different magnetically ordered phases in compressively strained interfaces arises due to the stabilization of the $d_{3z^2-r^2}$ orbital over $d_{x^2-y^2}$ orbitals and has not been reported earlier for such interfaces. The possibility to tailor the spin and orbital degrees of freedom across variously strained interfaces can be extended to the study and stabilization of non collinear magnetic textures across perovskite oxide interfaces.

References

[1] J. Dho, Y. N. Kim, Y. S. Hwang, J. C. Kim, and N. H. Hur, Appl. Phys. Lett. **82**, 1434 (2003).

[2] K. H. Ahn, T. Lookman, and A. R. Bishop, Nature **428**, 401 (2004).

[3] E. P. Houwman, G. Maris, G. M. De Luca, N. Niermann, G. Rijnders, D. H. A. Blank, and S. Speller, Phys. Rev. B **77**, 184412 (2008).

[4] H. Boschker, M. Mathews, P. Brinks, E. Houwman, A. Vailionis, G. Koster, D. H. A. Blank, and G. Rijnders, J. Magn. Magn. Mater. **323**, 2632 (2011).

[5] N. Naftalis, N. Haham, J. Hoffman, M. S. J. Marshall, C. H. Ahn, and L. Klein, J. Appl. Phys. **115**, 053709 (2014).

[6] M. S. Gabor, T. Petrisor, O. Pop, S. Colis, and C. Tiusan, J. Magn. Magn. Mater. **392**, 79 (2015).

[7] S. Roy, A. Solmaz, J. D. Burton, M. Huijben, G. Rijnders, E. Y. Tsymbal, and T. Banerjee, Phys. Rev. B **93**, 115101 (2016).

[8] Y. Feng, K.-J. Jin, L. Gu, X. He, C. Ge, Q.-H. Zhang, M. He, Q.-L. Guo, Q. Wan, M. He, H.-B. Lu, and G. Yang, Sci. Rep. **6**, 22382 (2016).

[9] Z. Liao, M. Huijben, Z. Zhong, N. Gauquelin, S. Macke, R. J. Green, S. Van Aert, J. Verbeeck, G. Van Tendeloo, K. Held, G. A. Sawatzky, G. Koster, and G. Rijnders, Nat. Mater. **15**, 425 (2016).

[10] Z. L. Liao, G. Koster, M. Huijben, and G. Rijnders, Sci. Rep. **7** (2017).

[11] M. Huijben, G. Koster, Z. L. Liao, and G. Rijnders, Applied Physics Reviews **4**, 041103 (2017).

[12] B. Wang, L. You, P. Ren, X. Yin, Y. Peng, B. Xia, L. Wang, X. Yu, S. Mui Poh, P. Yang, G. Yuan, L. Chen, A. Rusydi, and J. Wang, Nat. Commun. **4**, 2778 (2013).

[13] B. R. K. Nanda and S. Satpathy, Phys. Rev. B **78**, 054427 (2008).

[14] Y. Tokura and N. Nagaosa, Science **288**, 462 (2000).

[15] J.-H. Park, E. Vescovo, H.-J. Kim, C. Kwon, R. Ramesh, and T. Venkatesan, Nature **392**, 794 (1998).

[16] A. Urushibara, Y. Moritomo, T. Arima, A. Asamitsu, G. Kido, and Y. Tokura, Phys. Rev. B **51**, 14103 (1995).

[17] J. Burgy, A. Moreo, and E. Dagotto, Phys. Rev. Lett. **92**, 097202 (2004).

[18] J. B. Goodenough and J.-S. Zhou, Nature **386**, 229 (1997).

[19] J. M. D. Teresa, M. R. Ibarra, P. A. Algarabel, C. Ritter, C. Marquina, J. Blasco, J. Garcia, A. del Moral, and Z. Arnold, Nature **386**, 256 (1997).

[20] M. Uehara, S. Mori, C. H. Chen, and S.-W. Cheong, Nature **399**, 560 (1999).

[21] M. Bowen, M. Bibes, A. Barthelemy, J.-P. Contour, A. Anane, Y. Lemaitre, and A. Fert, Appl. Phys. Lett. **82**, 233 (2003).

[22] J. M. D. Teresa, A. Barthelemy, A. Fert, J. P. Contour, F. Montaigne, and P. Seneor, Science **286**, 507 (1999).

[23] K. G. Rana, T. Yajima, S. Parui, A. F. Kemper, T. P. Devereaux, Y. Hikita, H. Y. Hwang, and T. Banerjee, Sci. Rep. **3**, 1274 (2013).

[24] V. Garcia and M. Bibes, Nat. Commun. **5**, 4289 (2014).

[25] C. Adamo, X. Ke, H. Q. Wang, H. L. Xin, T. Heeg, M. E. Hawley, W. Zander, J. Schubert, P. Schiffer, D. A. Muller, L. Maritato, and D. G. Schlom, Appl. Phys. Lett. **95**, 112504 (2009).

[26] L. Yin, C. Wang, Q. Shen, and L. Zhang, RSC Advances **6**, 96093 (2016).

[27] M. Mathews, E. P. Houwman, H. Boschker, G. Rijnders, and D. H. A. Blank, J. Appl. Phys. **107**, 013904 (2010).

[28] K. G. Rana, S. Parui, and T. Banerjee, Phys. Rev. B **87**, 085116 (2013).

[29] W. Yuan, Y. Zhao, C. Tang, T. Su, Q. Song, J. Shi, and W. Han, Appl. Phys. Lett. **107**, 022404 (2015).

[30] C. Aruta, G. Ghiringhelli, A. Tebano, N. G. Boggio, N. B. Brookes, P. G. Medaglia, and G. Balestrino, Phys. Rev. B **73**, 235121 (2006).

[31] H. A. Jahn, E. Teller, and F. G. Donnan, Proc. R. Soc. Lond., A Math. phys. sci. **161**, 220 (1937).

[32] A. Tebano, C. Aruta, P. G. Medaglia, F. Tozzi, G. Balestrino, A. A. Sidorenko, G. Allodi, R. De Renzi, G. Ghiringhelli, C. Dallera, L. Braicovich, and N. B. Brookes, Phys. Rev. B **74**, 245116 (2006).

Chapter 4

Temperature-dependent Periodicity halving of the Inplane Angular Magnetoresistance in $La_{0.67}Sr_{0.33}MnO_3$ Thin Films on $LaAlO_3$

Abstract

Strain-engineering is used as a tool to alter electronic and magnetic properties like anisotropy energy. This study reports the different angle-dependent magnetoresistance properties of the strain-engineered $La_{0.67}Sr_{0.33}MnO_3$ thin films, grown on $LaAlO_3$, compared to their bulk analogues. Upon increasing temperature, a symmetry change from fourfold ($cos(4\theta)$) to twofold ($cos(2\theta)$) is observed in the angle-dependent resistance measurements. This systematic study with increasing temperature allows us to define three distinct temperature-dependent phases. The fourfold symmetric signal originates from magnetocrystalline anisotropy, whereas the twofold symmetric signal is believed to be the conventional anisotropic magnetoresistance. Our observations show that strain-engineering creates the possibility to manipulate the anisotropy which, for example, can ultimately lead to observations of noncollinear quasi-particles like skyrmions in single layer thin films of $La_{0.67}Sr_{0.33}MnO_3$.

4.1 Introduction

Doped manganites are studied extensively since the first observation of the colossal magnetoresistance (CMR) effect[1–3] in manganites. Other magnetoresistive effects such as anisotropic magnetoresistance (AMR)[2–6] and the planar Hall effect[7] have also gained attention. This interest resulted in various sensors[8–13] and applications due to the rising popularity of Internet of Things[14], which increased the demand for electronic magnetoresistance sensors measuring anything from traffic mobility to water flow[12]. From a scientific point of view, the magnetoresistance effects form handles for measuring and/or manipulating properties of the material to form, for example, new magnetic textures like skyrmions. A first step towards

creating magnetic textures can be the fine tuning of the anisotropy which creates the ideal circumstances for finding magnetic textures.

One manganite in particular, $La_{0.67}Sr_{0.33}MnO_3$ (LSMO), has attracted much attention due to its high Curie temperature of 360 K. Using pulsed laser deposition (PLD), epitaxial thin films of LSMO can be grown with minimal oxygen vacancies[15]. Thickness-dependent thin film studies in LSMO led to new findings such as a shift in Curie temperature[16–18], coexisting magnetic phases[16, 19] and presence of magnetic dead layers[20–24].

Besides controlling film thickness, the influence of strain induced by an underlaying substrate[6] on the angle-dependent magnetotransport in LSMO thin films has been investigated. However, most (LSMO) films are grown on $SrTiO_3$[7, 25–35], giving rise to tensile strain[36, 37]. Growing films on different substrates may change physical properties such as deforming the lattice, inducing oxygen octahedral tilt, or noncollinear magnetization thus introducing novel physical properties in thin films of $La_{1-x}Sr_xMnO_3$[20, 36, 38, 39]. On the other hand, replacing $SrTiO_3$ (001) (STO) with $LaAlO_3$ (001) (LAO) as a substrate, induces a large in-plane compressive strain in the pseudocubic LSMO film, resulting in a deformation to a tetragonal structure with an elongation in the [001] direction. Compressive strain reduces Curie temperature and can result in out-of-plane magnetic anisotropy[36, 40]. The out-of-plane anisotropy can be understood as a result of compressive strain deforming the unit cell, tweaking the magnetocrystalline anisotropy (MCA) to a preferential out-of-plane direction.

Anisotropy effects are mainly studied with either bulk characterization techniques such as ferromagnetic resonance (FMR)[35, 41], torque magnetometry[42] or a superconducting quantum interference device (SQUID) magnetometer[23, 42, 43] to characterize the temperature-dependent magnetic anisotropy. Alternative to bulk characterization techniques, techniques such as magnetic force microscopy[36] are used to study magnetization behavior locally (at small areas). Due to a Curie temperature above room temperature, various magnetism based studies have been conducted with $La_{0.67}Sr_{0.33}MnO_3$ at room temperature. Recent FMR studies at room temperature showed little MCA for LSMO on $SrTiO_3$[41], whereas in another study at 200 K, the MCA is clearly observed in thin films[35], showing the need for systematic temperature-dependent studies. Both torque magnetometry and FMR can be used to quantify the exact anisotropy energy, whereas often it is desirable to observe and influence the effective anisotropy.

In this paper, we present the longitudinal magnetotransport data of strain-engineered LSMO thin films on LAO, and investigate the temperature-dependent anisotropy, which provides information regarding the effective anisotropy.

4.2   Experimental setup

The films used in our experiments have been grown using PLD with an excimer (KrF) laser using the previously published parameters[19]. The growth of both films were monitored *in-situ*, using reflection high-energy electron diffraction (RHEED), to verify a smooth epitaxial growth (see Supplementary Information [SI] Fig. 4.5).
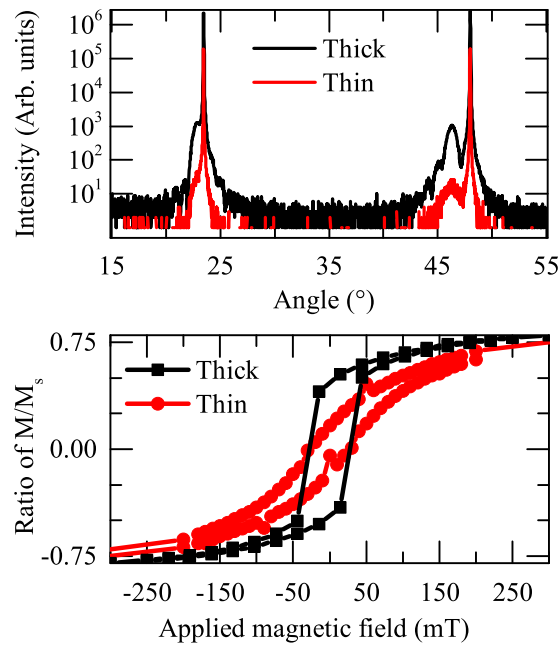
***Figure 4.1**: (a) X-ray θ-2θ diffraction of LSMO films. The Laue oscillations, clear from the thick film spectra, indicate a smooth and epitaxial growth of 23 unit cells, which is in close correspondence to the 25 unit cells observed with RHEED. (b) Normalized in-plane magnetization loops at 10 K for both films, with a coercive field of 30 mT and a saturation magnetization around 250 mT.*

The thickness of the film is calculated from the Laue fringes and is found to be 9.1 nm (23 u.c.) and 5.5 nm (14 u.c.) for the thick and thin film, respectively. Laue fringes fitting on the XRD $\theta - 2\theta$ are shown in Fig. 4.7 of the SI. The thickness determined from XRD corresponds to the values obtained by counting RHEED intensity oscillations. Magnetic hysteresis loops, taken at 10 K and 300 K using a magnetic property measurement system (MPMS) is shown in Fig. 4.1 (b). At 10 K, both films

display typical ferromagnetic behavior with a coercive field of 30 mT and a saturation magnetization around 250 mT.

	Thin film	Thick film
Thickness	5.5 nm	9.1 nm
H_{M_s} at 10 K	200 mT	300 mT
H_c at 10 K	30 mT	30 mT
Curie temperature	195 K	320 K

***Table 4.1**: Summary of investigated thin films characteristics*

The magnetic properties of LSMO are further characterized by temperature-dependent magnetotransport measurements. For this purpose, the films are patterned with a Hall bar structure and etched using aqua regia[44]. Thereafter, we measured the temperature-dependence of the resistivity in the presence of a magnetic field. A DC current of 5 μA is sent through the LSMO Hall bar to measure the longitudinal resistance in a 4-probe configuration as presented in Fig. 4.2 (a), using a Keithley 2410. The longitudinal resistivity, ρ-T (in Fig. 4.2 [b]), is measured while heating the sample from 10 K to 300 K. The thin film (black squares) has two transition temperatures around 50 K and 225 K. Below 50 K and above 225 K the film behaves as an insulator, while in the temperature range 50–225 K, the film behaves as a metal. The insulating behavior below 50 K is caused by a reduction in double exchange hopping and is more often observed in LSMO thin films of several unit cells thick[16, 19]. The transition at 225 K is close to the Curie temperature of this film (see Fig. 4.8). The thick film (green circles) is metallic through the entire temperature range, as depicted in Fig. 4.2 (b). Other ρ-T measurements on the films (see Fig. 4.8, at higher temperatures allowed us to determine the maximum CMR to extract T_C as depicted in Table 4.1.

For the angle-dependent magnetoresistance measurements (AdMR) the magnetic field is rotated around the [001] crystallographic axis, as shown in Fig. 4.2 (a), while the resistance is measured in the 4-probe configuration. The applied field of 0.7 T is at least one order of magnitude greater than the coercive magnetization field, as observed from the hysteresis loop in Fig. 4.1 (b). Therefore, one can assume that the magnetization is parallel to the applied field direction (**M** ∥ **B**). The data obtained from the measurements (see Fig. 4.3 [a] and [b] and SI Fig. 4.9) is fitted with an equation based on the AMR energy terms [3]:

$$E = A_0 + A_1 \cos^2(\theta) + A_2 \cos^4(\theta), \tag{4.1}$$

where A_0, A_1 and A_2 are constants, and θ is the angle between current and ap-
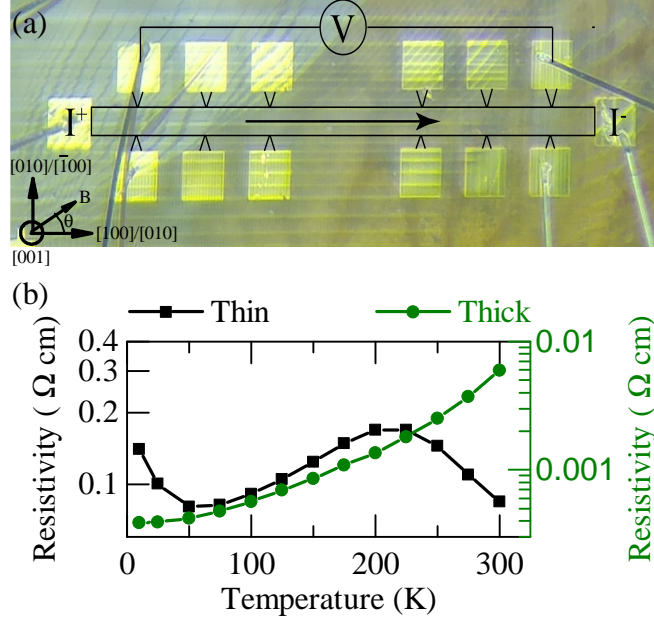
Figure 4.2: *(a) Optical microscope picture of the etched Hall bar from the thick LSMO film with the current direction either along the, equivalent, $[010]_{pc}$ or $[100]_{pc}$ pseudocubic crystallographic direction of LAO. In the picture the contacts used in the 4-wire setup are indicated. (b) Temperature dependence of LSMO's longitudinal resistivity (ρ-T) for both thin (black squares) and thick (green circles) films.*

plied magnetic field. For angle-dependent resistivity measurements, this equation is transformed into equation 4.2, as shown in literature[45], to which we added a term to compensate for thermal drift. The resulting formula is used to fit the longitudinal resistivity:

$$\rho_{long} = \rho_0 + \rho_{2f} \cos\left(2\theta - \delta_{2f}\right) + \rho_{4f} \cos\left(4\theta - \delta_{2f} - \delta_{4f}\right)$$
$$+ \rho_{drift} \exp\left[-(360 + \theta)/\tau_0\right], \tag{4.2}$$

where the longitudinal resistivity, ρ_{long}, in equation 4.2 depends on a baseline resistance ρ_0, and on two cosine-modulated functions with amplitudes ρ_{2f} and ρ_{4f}. The terms δ_{2f} and δ_{4f} are offsets indicating the position of the magnetic hard-axis. The last term, ρ_{drift}, is added to compensate for thermal drift. More in depth infor-

mation regarding the process undertaken to account for and eliminate the thermal drift effect is discussed in SI AMR fitting section. Fig. 4.3 (a) and (b) show the angle-dependent resistivity and their respective fittings with equation 4.2 for the thin (black squares) and the thick (green circles) film.

4.3   Results & Discussion

Fig. 4.3 (c) shows the normalized AdMR ($\rho_{(\theta)}/\rho_0 * 100\%$) at different temperatures for the thin film. At temperatures 10–125 K, a fourfold symmetry in the resistance is observed. Upon increasing the temperature, at 100 K, the signal starts to show an asymmetry. Increasing the temperature, from 125 to 250 K, causes the signal to show twofold symmetry, which peaks close to the CMR maximum, at 195 K, for the thin film. Above 250 K, no angle-dependent signal is observed. For the thick film in Fig. 4.3 (d), we observed at low temperatures no dominant periodicity. Upon increasing the temperature, the twofold signal becomes dominant around 150 K and remains so until 300 K. The twofold signal present in both films is observed in various magnetic materials and depends directly on the applied magnetic field strength and the angle between the applied magnetic field and the current direction [3, 5].

To quantify the change in signal with temperature, the extracted amplitudes from a fit with equation 4.2 are plotted versus temperature in Fig. 4.4 (a) and (b). To follow similar conventions as in published literature, Figs. 4.4 (c) and (d) show AMR percentage versus temperature based on the conventional AMR definition:

$$AMR \stackrel{\text{def}}{=} \frac{\rho(90) - \rho(0)}{\rho(0)} \times 100\% \approx \frac{2\,A_{2f}}{\rho_0} \times 100\%, \tag{4.3}$$

where the AMR is defined as twice the extracted amplitude from equation 4.2 divided by ρ_0. This definition is used for both the two- and fourfold signals in Fig. 4.4 (c) and (d).

The thin film, in Fig. 4.4 (a) and (c), confirms that the dominant signal is fourfold symmetric below 125 K. The observed peak at 50 K, in Fig. 4.4 (c), is due to the increase in resistance below 50 K, decreasing the AdMR percentage for the measurements at 10 K and 25 K. The twofold signal for both films shows a maximum around Curie temperature, which is expected for the conventional AMR effect[3, 5]. In addition, the CMR, shown in SI Fig. 4.8, shows the same trend in signal strength as does the conventional AMR, as is commonly observed.

Similar trends, comparable to the temperature scaling, for both the two- and fourfold signals are shown with increasing magnetic field strength in SI Fig. 4.10. The temperature and magnetic field dependence, for the fourfold symmetric signal, can be explained by a constant anisotropic energy in the LSMO thin film. The
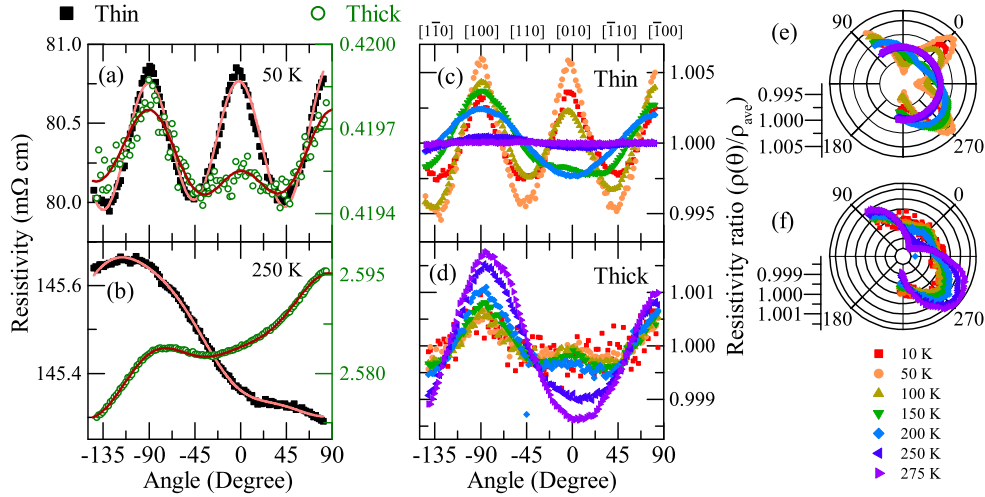
Figure 4.3: *(a) and (b) AdMR signal at 50 and 250 K, respectively, for the thin (black squares) and thick (green circles) films with a fit (solid line) based on equation 4.2. For (c) and (d) the plotted resistance is corrected for thermal drift and normalized, $\rho(\theta)/\rho_{average}$, for multiple temperatures. Note that the indicated axes are allowed to be rotated by 90 degrees as the axes [010] and [100] are equivalent. Plots (e) and (f) are the normalized data of (c) and (d), plotted in polar plot format, respectively. The plot (e) shows a clear transition from fourfold to twofold without any change in peak positions, indicating that there is no magnetic easy-axis transformation. The legend in the right bottom corresponds to Fig. 4.3 (c), (d), (e), and (f).*

constant anisotropy energy ($E_{ani}|_{0K,0T} = E_{100} - E_{110}$) can be overcome by increasing either temperature, applied magnetic field, or thickness. Based on the crystallographic directions of the LaAlO$_3$ substrate and the Hall bar placement, the observed fourfold signal in our measurements follows the in-plane bi-axial magnetic easy axes along the $[110]_{pc}$ and $[1\bar{1}0]_{pc}$ directions, similar to the fourfold observations reported previously in literature[6, 46–48]. Based on the temperature scaling in Fig. 4.4 (a) and on existing literature review, we attribute the fourfold symmetric signal to the tetragonal MCA, as it fits all observed features.

In Fig. 4.4 we observe a dominant MCA signal in the thin film, but not in the thick film. A possible explanation stems from a change in the conduction mechanism of LSMO. The two major conduction mechanisms found in LSMO are, first of all, the double exchange hopping causing electron–electron ($\sim \rho T^2$) and electron–
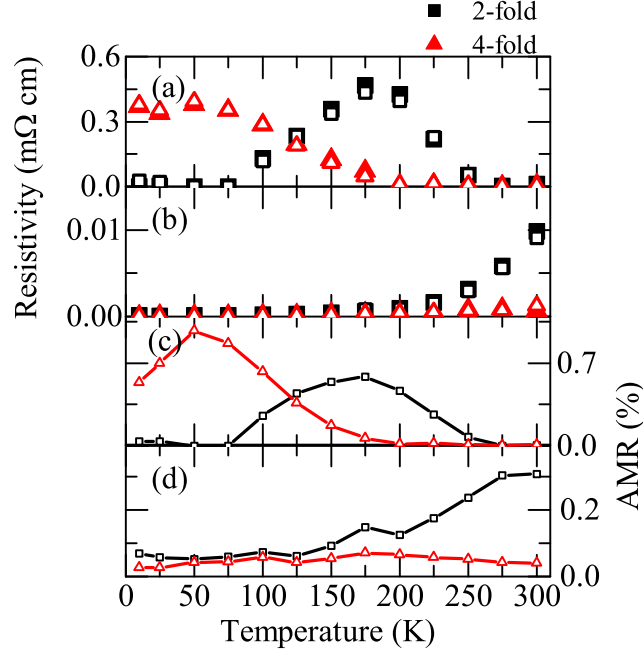
Figure 4.4: *The thin film, in (a) and (c), shows three distinct phases with tem-
perature. (a) Shows the amplitude of the fitted signal. The fourfold
amplitude is stable in size, around 0.4 mΩ cm, up to 50 K, after which
it decreases to zero at 200 K. The thick film, in (b) and (d), shows two
distinct regions. (c) and (d) show the AMR strength based on equation
4.3. (all) The closed and open symbols correspond to the clockwise or
counterclockwise rotation in the measurement, respectively.*

magnon ($\sim \rho T^{4.5}$) scattering below T$_C$, and secondly the polaronic conduction via
hopping above T$_C$. Decreasing film thickness causes the resistance to increase, at-
tributed to a decrease in the semiconducting bandwidth of the itinerant d-electrons[49].
The decrease in thickness eventually leads to a thermally activated hopping
($\sim e^{E_a/T}$)[16], as observed below 50 K in our thin film. Rotating the magnetic field,
for example, by orienting the magnetic field along an easy or hard axis, decreases or
increases, respectively, the required hopping energy due to the MCA contribution.
The net effect, MCA has on the conduction, is larger for resistive films. This ef-
fect is intuitively understood for a metallic film where the activation energy is zero,
therefore hopping is always possible irrespective of the orientation of the applied
magnetic field.

4.4   Conclusion

To conclude, we report the following on the temperature-dependent AdMR signal versus temperature: At low temperature, the fourfold signal appears to be directly related to the MCA, with easy axes in $[110]_{pc}$ and $[1\bar{1}0]_{pc}$ directions. At higher temperatures, a twofold signal is observed, caused by the conventional AMR signal of ferromagnetic compounds. We relate the increase in signal strength for AdMR and CMR to the increasing resistivity of the films caused by the decreasing thickness. These results indicate the feasibility to tune strain and thickness to control the anisotropy. Based on the results, we predict resistance changes due to strain-engineering to be best observed in thin samples which still portray metallic behavior. Future experiments can aim to engineer an out-of-plane magnetization to deeper understand the relation between strain and the (out-of-plane) MCA observed by magnetotransport. Inducing a larger compressive strain on a thin (5.5 nm) film of LSMO can induce an out-of-plane anisotropy to facilitate the formation of magnetic textures like skyrmions in a single layer LSMO.

References

[1] X. G. Chen, J. B. Yang, Y. B. Yang, C. S. Wang, S. Q. Liu, Y. Zhang, J. Z. Han, and Y. C. Yang, J. Appl. Phys. **115**, 043904 (2014).

[2] W. Thomson, Proc. R. Soc. Lond. **8**, 546 (1857).

[3] T. McGuire and R. Potter, IEEE Trans. Magn. **11**, 1018 (1975).

[4] J. O'Donnell, J. N. Eckstein, and M. S. Rzchowski, Appl. Phys. Lett. **76**, 218 (2000).

[5] M. Egilmez, K. H. Chow, and J. A. Jung, Mod. Phys. Lett. B **25**, 697 (2011).

[6] M. Bibes, B. Martinez, J. Fontcuberta, V. Trtik, C. Ferrater, F. Sanchez, M. Varela, R. Hiergeist, and K. Steenbeck, J. Magn. Magn. Mater. **211**, 206 (2000).

[7] Y. Bason, L. Klein, J.-B. Yau, X. Hong, and C. H. Ahn, Phys. Status Solidi C **1**, 3336 (2004).

[8] L. Balcells, A. E. Carrillo, B. Martınez, F. Sandiumenge, and J. Fontcuberta, J. Magn. Magn. Mater. **221**, 224 (2000).

[9] J. Z. Sun, A. Gupta, G. Xiao, P. L. Trouilloud, and P. P. Lecoeur, "Magnetic devices and sensors based on perovskite manganese oxide materials", U.S. patent US-5792569-A (11 August 1998).

[10] Y. Xu, U. Memmert, and U. Hartmann, Sens. Actuators, A **91**, 26 (2001).

[11] L. Balcells, R. Enrich, J. Mora, A. Calleja, J. Fontcuberta, and X. Obradors, Appl. Phys. Lett. **69**, 1486 (1996).

[12] O. Aleksic, S. Savic, M. Nikolic, L. Sibinoski, and Lukovic, Microelectron. Int. **26**, 30 (2009).

[13] S. Balevicius, N. Zurauskiene, V. Stankevic, S. Kersulis, A. Baskys, V. Bleizgys, J. Dilys, A. Lucinskis, A. Tyshko, and S. Brazil, IEEE Trans. Instrum. Meas. **69**, 2808 (2020).

[14] X. Liu, K. H. Lam, K. Zhu, C. Zheng, X. Li, Y. Du, C. Liu, and P. W. T. Pong, IEEE Trans. Magn. **55**, 1 (2019).

[15] H. Guo, J.-o. Wang, X. He, Z. Yang, Q. Zhang, K.-j. Jin, C. Ge, R. Zhao, L. Gu, Y. Feng, W. Zhou, X. Li, Q. Wan, M. He, C. Hong, Z. Guo, C. Wang, H. Lu, K. Ibrahim, S. Meng, H. Yang, and G. Yang, Adv. Mater. Interfaces **3**, 1500753 (2016).

[16]H. Boschker, J. Kautz, E. P. Houwman, W. Siemons, M. Huijben, D. H. A. Blank, G. Koster, A. Vailionis, and G. Rijnders, Phys. Rev. Lett. **109** (2012).

[17]S. Chen, S. Wei, F. Jin, S. Ke, X. Zeng, L. Chen, and C. Huang, Ceram. Int. **44**, 13695 (2018).

[18]T. Nurgaliev, U. Topal, B. Blagoev, and E. Mateev, J. Supercond. Nov. Magn. **25**, 2495 (2012).

[19]A. A. Burema, J. J. L. van Rijn, and T. Banerjee, J. Vac. Sci. Technol. A **37**, 021103 (2019).

[20]X. Li, I. Vrejoiu, M. Ziese, and P. van Aken, European Microscopy Congress 2016: Proceedings, 968 (2016).

[21]L. Wu, J. Ma, J. Ma, Y. Zhang, Y. Gao, Q. Zhang, M. Liu, and C.-W. Nan, Sci. Bull. **61**, 157 (2016).

[22]R. P. Borges, W. Guichard, J. G. Lunney, J. M. D. Coey, and F. Ott, J. Appl. Phys. **89**, 3868 (2001).

[23]H. Boschker, J. Kautz, E. P. Houwman, G. Koster, D. H. A. Blank, and G. Rijnders, J. Appl. Phys. **108**, 103906 (2010).

[24]S. B. Porter, M. Venkatesan, P. Dunne, B. Doudin, K. Rode, and J. M. D. Coey, IEEE Trans. Magn. **53**, 1 (2017).

[25]N. Naftalis, N. Haham, J. Hoffman, M. S. J. Marshall, C. H. Ahn, and L. Klein, Phys. Rev. B **86**, 184402 (2012).

[26]V. Bhosle, J. T. Prater, and J. Narayan, J. Appl. Phys. **102**, 013527 (2007).

[27]J.-B. Yau, X. Hong, A. Posadas, C. H. Ahn, W. Gao, E. Altman, Y. Bason, L. Klein, M. Sidorov, and Z. Krivokapic, J. Appl. Phys. **102**, 103901 (2007).

[28]H. Sharma, H. Bana, A. Tulapurkar, and C. V. Tomy, Mater. Chem. Phys. **180**, 5 (2016).

[29]H. Sharma, A. Tulapurkar, and C. V. Tomy, Appl. Phys. Lett. **105**, 222406 (2014).

[30]Y. Suzuki, H. Y. Hwang, S.-W. Cheong, and R. B. van Dover, Appl. Phys. Lett. **71**, 140 (1997).

[31]M. Mathews, E. P. Houwman, H. Boschker, G. Rijnders, and D. H. A. Blank, J. Appl. Phys. **107**, 013904 (2010).

[32]R.-W. Li, H. Wang, X. Wang, X. Z. Yu, Y. Matsui, Z.-H. Cheng, B.-G. Shen, E. W. Plummer, and J. Zhang, Proc. Natl. Acad. Sci. U.S.A. **106**, 14224 (2009).

[33]D. J. Groenendijk, N. Manca, J. de Bruijckere, A. M. R. V. L. Monteiro, R. Gaudenzi, H. S. J. van der Zant, and A. D. Caviglia, Eur. Phys. J. Plus **135**, 627 (2020).

[34]C. Wang, H. Seinige, G. Cao, J.-S. Zhou, J. B. Goodenough, and M. Tsoi, Phys. Rev. X **4**, 041034 (2014).

[35]J. M. Vila-Fungueiriño, C. T. Bui, B. Rivas-Murias, E. Winkler, J. Milano, J. Santiso, and F. Rivadulla, J. Phys. D: Appl. Phys. **49**, 315001 (2016).

[36]J. Dho, Y. N. Kim, Y. S. Hwang, J. C. Kim, and N. H. Hur, Appl. Phys. Lett. **82**, 1434 (2003).

[37]E. P. Houwman, G. Maris, G. M. De Luca, N. Niermann, G. Rijnders, D. H. A. Blank, and S. Speller, Phys. Rev. B **77**, 184412 (2008).

[38]M. Ziese, H. C. Semmelhack, and P. Busch, J. Magn. Magn. Mater. **246**, 327 (2002).

[39]M. Baldini, T. Muramatsu, M. Sherafati, H.-K. Mao, L. Malavasi, P. Postorino, S. Satpathy, and V. V. Struzhkin, Proc. Natl. Acad. Sci. U.S.A. **112**, 10869 (2015).

[40]Y. Tokura and Y. Tomioka, J. Magn. Magn. Mater. **200**, 1 (1999).

[41]I. Benguettat-EL Mokhtari, Y. Roussigné, T. Petrisor, F. Zighem, F. Kail, L. Chahed, V. Pierron, L. Méchin, M. Gabor, and M. Belmeguenai, Phys. Status Solidi B **257**, 2000265.

[42]K. Steenbeck, T. Habisreuther, C. Dubourdieu, and J. P. Senateur, Appl. Phys. Lett. **80**, 3361 (2002).

[43]H. Boschker, M. Mathews, P. Brinks, E. Houwman, A. Vailionis, G. Koster, D. H. A. Blank, and G. Rijnders, J. Magn. Magn. Mater. **323**, 2632 (2011).

[44]K. G. Rana, T. Yajima, S. Parui, A. F. Kemper, T. P. Devereaux, Y. Hikita, H. Y. Hwang, and T. Banerjee, Sci. Rep. **3**, 1274 (2013).

[45]Y. Bason, J. Hoffman, C. H. Ahn, and L. Klein, Phys. Rev. B **79** (2009).

[46]B. Aktas, B. Heinrich, G. Woltersdorf, R. Urban, L. R. Tagirov, F. Yildiz, K. Ozdogan, M. Ozdemir, O. Yalcin, and B. Z. Rameev, J. Appl. Phys. **102**, 013912 (2007).

[47]W. Y. Cui, P. Li, and H. L. Bai, J. Appl. Phys. **117**, 133904 (2015).

[48]H. Wang, W. Wang, N. Hu, T. Duan, S. Yuan, S. Dong, C. Lu, and J.-M. Liu, Phys. Rev. Appl. **10**, 014025 (2018).

[49]K. G. Rana, *Electron transport across complex oxide heterointerfaces*, Doctoral dissertation, University of Groningen, Groningen (s.n., 2013).
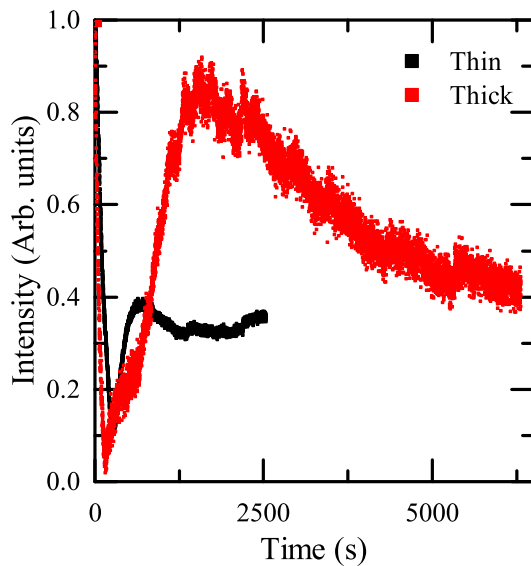
Supplementary Information

Figure 4.5: The growth of the thin film is in situ monitored by RHEED during the deposition. The RHEED shows intensity oscillations indicating a layer-by-layer growth for LSMO on LAO. The oscillations can be discerned by processing the data and give a thickness of 5.5 and 9.5 nm similar to the Laue fringe fitting of the XRD.
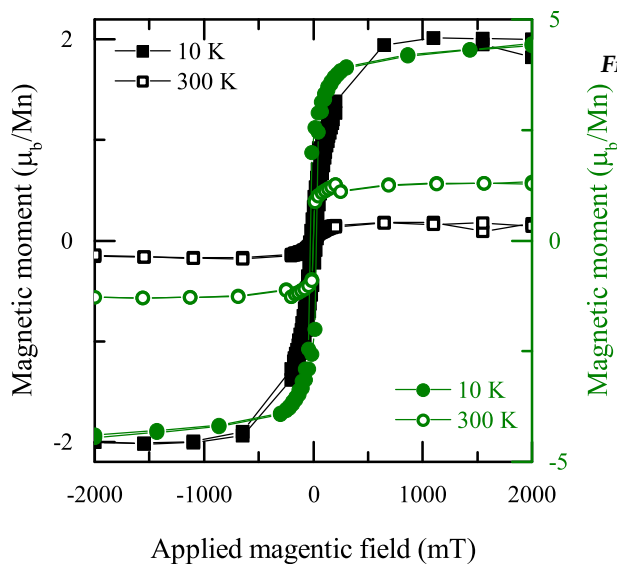

Figure 4.6: Magnetization versus applied magnetic field for the thick (green circles) and thin (black squares) film, with a saturation magnetization of 4.9 μ_b/Mn and 2.0 μ_b/Mn, respectively. The signal is measured in-plane at 10 K and 300 K. Both have a similar coercive field of 30 mT, as presented in the paper.
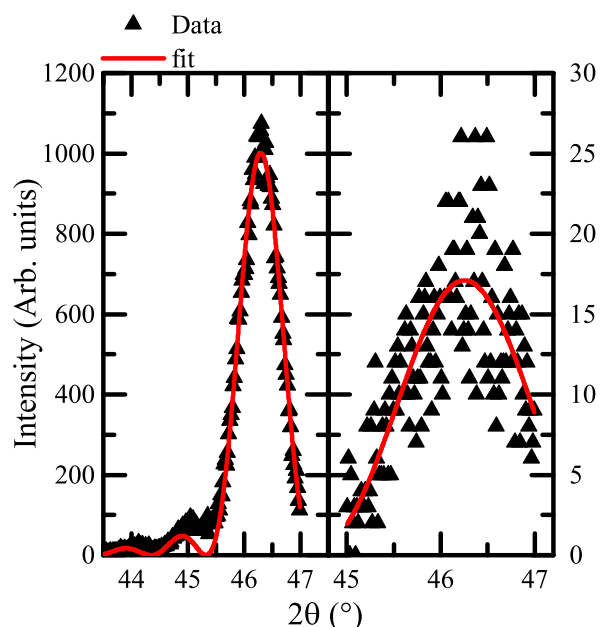
Figure 4.7: *Zoom in of the XRD spectrum obtained from the thick and thin LSMO films. The Laue fringe fitting is performed on the 002 thin film peak of the film. A thickness of 23±1 u.c. (9.1±0.4 nm) is extracted from the fitting for the thick film and a thickness of 13±1 u.c. (5.2±0.4 nm) is extracted for the thin film.*

CMR

Colossal magnetoresistance (CMR) is defined as:

$$CMR = \frac{\rho(H) - \rho(0)}{\rho(0)} \times 100\%, \tag{4.4}$$

where $\rho(H)$ is the resistivity when a magnetic field is applied, and $\rho(0)$ is the resistivity without an applied magnetic field. The CMR versus temperature peaks at the Curie temperature.

In figure 4.8, the observed MR is significantly larger for the thin film compared to the thick film, also observed by others[1]. Decreasing the film thickness causes the demagnetization energy term to be relatively stronger. The stronger demagnetization energy reduces the spontaneous magnetization and therefore the double exchange hopping of the electrons. The larger demagnetization causes a greater difference in resistance between $\rho(0)$ and $\rho(H)$. In turn, this leads to a large CMR for thinner films. The ρ-T measurements of Fig. 4.8 show two electrical phases. Below T_C, the films behave metallic and above T_C their behavior is insulating. The insulating phases below 50 K for the thin film is not observed as the measurements start
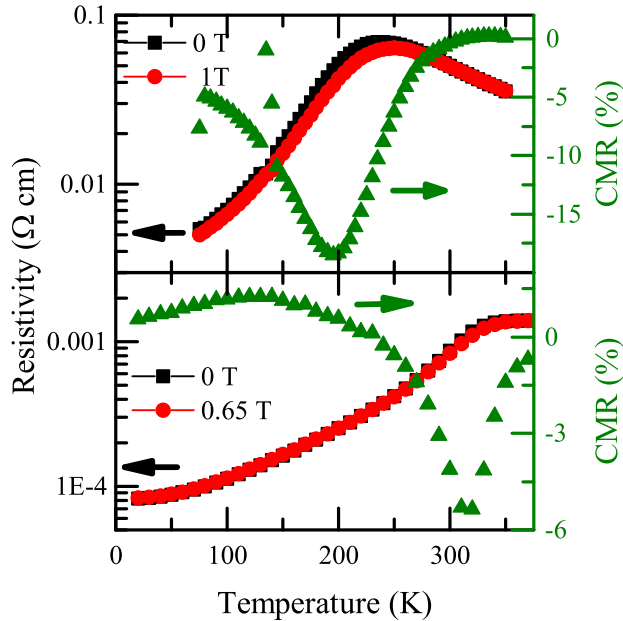
Figure 4.8: *Temperature dependence of LSMO's longitudinal resistivity (ρ-T) for both thin (top panel) and thick (bottom panel) films. (black squares) correspond to measurements without a magnetic field applied. (red circles) correspond to measurements with a magnetic field applied. The resistivity shows typical low-strain LSMO films, which behave as a ferromagnetic metal below T_C, and as a paramagnetic insulator above T_C. The negative CMR (green triangles) peaks at 195 K and 320 K, for thin and thick films, respectively.*

at 75 K. The maximum in CMR coincides with 195 and 320 K for the thin and thick film respectively.

AMR fitting

To minimize thermal drift and allow for a steady-state situation before each measurement a temperature was set, followed by a settling time of 45 minutes to allow the temperature to stabilize. During this time the current of 5 µA is still applied, and the applied magnetic field of 0.7 T is along the 90 degree position. During AdMR measurements, the observed temperature in the system fluctuated less than 0.1 K.

From time-dependent studies as well as high temperature AdMR measurements, we observe a clear exponential decay in resistance with time. Upon reversing the rotation direction the resistance decreases, indicating a time-dependent effect, which

can be fitted with

$$\rho_{drift} = A * exp(-(360 + \theta)/\tau), \tag{4.5}$$

where A is the exponential decay amplitude in Ω cm, θ is the angle (in degree) between the current and magnetic field, and τ is a fitting parameter. The 360 degree is added to prevent crossing over $\theta = 0$, to ease the fitting.

As multiple measurements are taken, a good starting estimate of exponential decay amplitude (A) can be made ($A = \rho_{90}(t = start) - \rho_{90}(t = end)$). This estimate is used to verify if the subtracted drift is not overcompensating and to increase the fit quality. Secondly, the baseline resistance is verified with the known resistance obtained from ρ-T measurements. A quantitative deviation in shape of the curve would indicate an overcompensation of the drift. Lastly, the results of the trace and retrace are compared. The trace and retrace yielded similar numbers for the fitting parameters, indicating a proper systematic removal of thermal drift from the data.

For all curves both trace and retrace are fitted. Two curves did not fit properly, the 100 K trace and retrace and 125 K trace, for the thick 9.5 nm film. The 3 mentioned data points give an unexpected high AdMR % signal. The mentioned data set has difficulty in fitting the background drift resulting in lower values for the baseline resistance and hence the high AdMR % signals. The output parameters were cross-referenced with known values, for instance the baseline resistivity (ρ_0) versus the measured ρ-T curve.
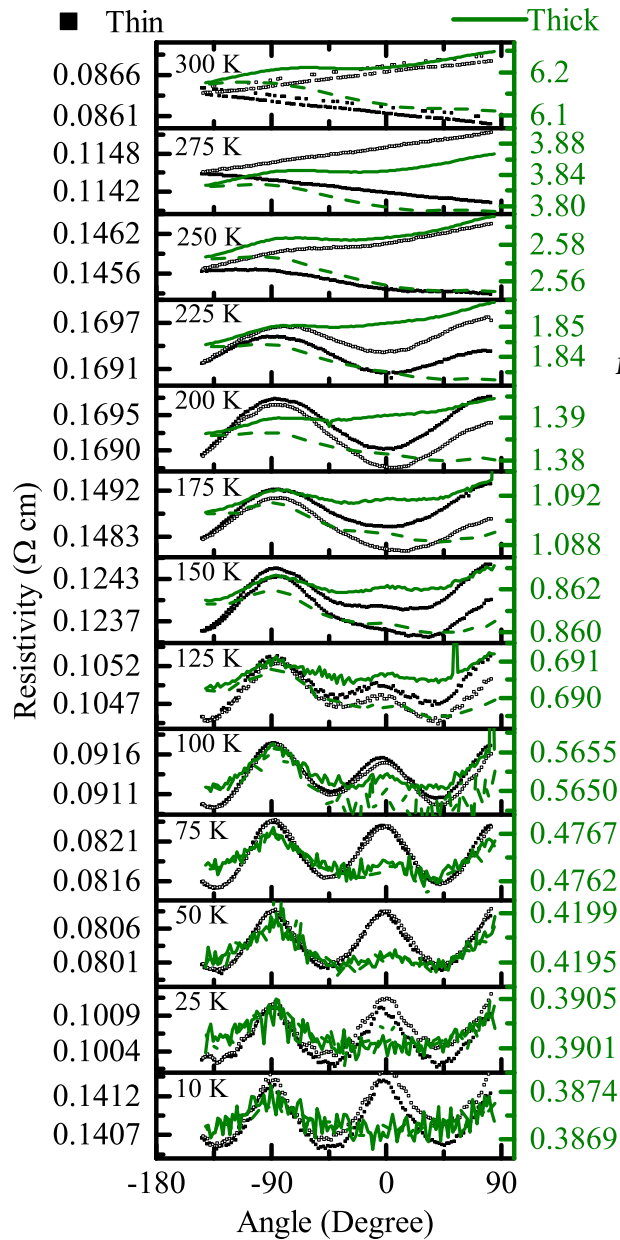
Figure 4.9: Longitudinal AdMR resistivity signal of the thin (black symbols) and thick (green lines) LSMO films measured at different temperatures, with an applied magnetic field of 0.7 T magnetic field. Each panel indicates the temperature at which the data was obtained. The left axis is for the thin film (black symbols) and the right axis is for resistivity of the thick film (green lines)
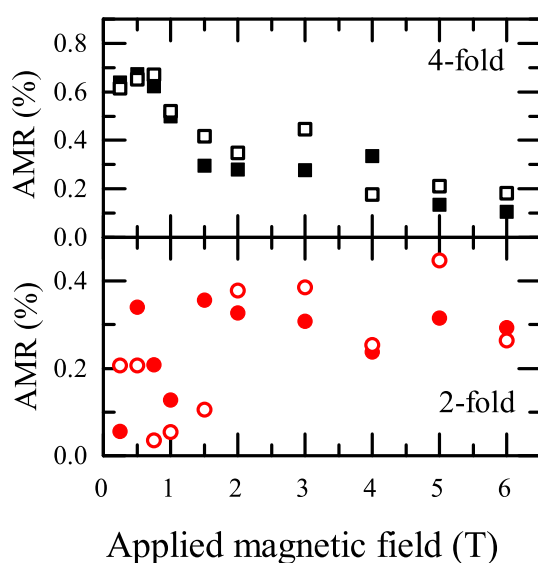
Figure 4.10: *AdMR signal decreases with applied magnetic field strength at 50 K for the 5.5 nm thick film. The data shows the fourfold symmetric signal (top panel), originating from a constant energy term e.g. crystalline anisotropy. The fourfold signal disappears with increasing magnetic field, indicating a constant energy term as the signal's origin, which can be overcome by increasing the Zeeman energy in the system. The twofold symmetric signal (bottom panel) originates from a coupling between magnetic field and current. This coupling causes a positive scaling of the conventional AMR with increasing magnetic field.*

References

[1]S. Mukhopadhyay, I. Das, and S. Banerjee, J. Phys.: Condens. Matter **21**, 026017 (2008).

Chapter 5

Temperature-dependent Out-of-plane Anisotropy in Compressively strained $La_{0.67}Sr_{0.33}MnO_3$ Thin Films

Abstract

We studied the temperature and strain dependence of the perpendicular magnetic anisotropy in $La_{0.67}Sr_{0.33}MnO_3$ thin films by performing temperature- and angle-dependent magnetotransport measurements. Three films of similar thickness (14 u.c., 14 u.c. and 15 u.c.) but with different out-of-plane crystallographic strain (1.9%, 0.9% and -0.7%) are studied. The films are grown on $LaAlO_3$ and $SrTiO_3$ substrates by pulsed laser deposition. We observe a clear increase in the out-of-plane magnetic anisotropy with increasing out-of-plane strain in the angle-dependent magnetotransport measurements which is present up to 80 K for the highest (1.9%) strained sample. The deformation of the unit cell, as discussed in earlier reports, point to the magnetocrystalline anisotropy as the main driver altering the magnetic easy axis direction. Our results highlight the utility of the effective magnetocrystalline anisotropy as a tool to control the desired anisotropy in crystalline thin films of $La_{0.67}Sr_{0.33}MnO_3$.

5.1 Introduction

Manganites attracted scientific interest due to the discovery of key phenomena such as colossal magnetoresistance (CMR)[1–6], half-metallicity[7], anisotropic magnetoresistance (AMR)[2, 3, 8–14], magnetocrystalline anisotropy (MCA)[13, 15–17] and negative magnetoresistance effect[3]. Furthermore, the introduction of pulsed laser deposition technique allowed for the systematic and reliable growth of complex oxide thin films, such that the influence of material properties, like strain[18–20], doping/stoichiometry[21–23], or step-edges[24] can be systematically investigated.

$La_{0.67}Sr_{0.33}MnO_3$ (LSMO) is a widely studied member in the manganite family. In bulk, LSMO has a ferromagnetic metallic (FMM) ground state below the

Curie temperature (T_C) and has a paramagnetic insulating (PMI) state above T_C. The physical coupling between the electrical transport and magnetic properties in LSMO causes CMR and AMR to peak close to T_C, which is explained invoking the double-exchange mechanism, as proposed by Zener[25]. Double exchange is based on electron hopping from the $Mn^{3+}e_g$ orbital via the oxygen 2p orbital to the $Mn^{4+}e_g$ orbital. However, a caveat is the angle dependence of the hopping probability between the two spin states that favors the spin alignment of neighboring Mn atoms for the double exchange process. Due to a strong interaction between spin orientation, charge hopping and orbital overlap, manipulation of the magnetic anisotropy in LSMO is possible by applying strain during thin film growth.

In particular, thin films of $La_{0.67}Sr_{0.33}MnO_3$ on $SrTiO_3$ (STO) have been studied extensively, because of their high T_C of 360 K and relatively easy stoichiometric growth characteristics. But LSMO grown on STO yields an inplane anisotropy whereas, creating a controllable out-of-plane magnetic anisotropy is desirable for various applications, especially for stabilizing magnetic skyrmions[26], creating innovative magnetic memories like a (skyrmion) racetrack memory[27–29], and SOT-MRAM devices[30–32].

A proven method of applying epitaxial strain is by growing thin films on a suitable substrate with the desired inplane (ip) lattice constant. The ip compressive (tensile) strain results in a deformation of the LSMO unit cell (u.c.) leading to an increased (decreased) c/a ratio, causing a tetragonal (orthorhombic) deformation of the unit cell due to the Poisson effect. Consequently, due to the strong coupling between conduction and magnetism, magnetic properties are also altered, causing effects like a change in Curie temperature[33, 34], a change in coercive field or a rotation of the magnetic easy axis[16, 35, 36].

Previous studies on compressively strained manganites used various experimental techniques to examine the anisotropy of manganites, ranging from magnetic force microscopy[19, 37], ferromagnetic resonance[38–41], magneto-optical Kerr effect[42] or torque measurements[16]. But for practical applications, demonstration of electric current control of magnetic anisotropy is desired.

Therefore, we study temperature-dependent magnetic anisotropy by performing temperature- and angle-dependent magnetoresistance measurements. The angle dependence gives an indication of the anisotropy direction, while the temperature-dependence serves as a rough estimate of the magnitude of $\Delta E_{anisotropy}$ between the ip and out-of-plane (oop) direction.

Our results qualitatively reinforce the general understanding of the behavior of doped manganites, by systematically studying the temperature dependence of the anisotropy via magnetotransport measurements. At low temperatures, an oop anisotropy is observed, whereas at high temperatures, the ip anisotropy dominates.

We also observe a change in oop anisotropy by varying the oop strain in the grown films. We hypothesize that the deformation of the unit cell caused by the epitaxial ip strain alters the magnetocrystalline anisotropy, which is known to favor the magnetization direction along the c-axis of the pseudo-cubic unit cell for LSMO and $La_{0.67}Ca_{0.33}MnO$ on STO and LAO substrates[16, 37, 43–45].

5.2 Experimental setup

To characterize the magnetic anisotropy in LSMO thin films, three films with different oop strain are grown with pulsed laser deposition (PLD). The LAO substrates used are as-received, while the STO substrate is treated following a well established protocol [46, 47] using a buffered hydrofluoric acid solution and annealing at 960 °C in a pure oxygen environment to ensure single termination and smooth step edges. All films are deposited using similar growth conditions during PLD. During PLD, the heater temperature is set to 750 °C and the steady oxygen flow (10 ccpm) results in a background pressure between 0.3 and 0.35 mBar. The fluence of the KrF laser (248 nm) was set to 2 J/cm^2 with a repetition rate of 1 Hz. *In situ* reflective high energy electron diffraction (RHEED) is used to track the growth of the samples. After reaching the desired thickness, the samples are annealed in 70 mBar oxygen while cooling down (10 °C/min). The RHEED oscillations indicate an epitaxial layer-by-layer growth which is confirmed by X-ray diffraction. From the $\theta - 2\theta$ scans (Fig. 5.5) an oop strain between -0.7%-1.9% for the discussed samples is extracted. More details can be found in the supplementary information (Fig. 5.5 and Fig. 5.6)

Before the magnetotransport experiments are conducted, the LSMO thin film is chemically etched into Hall bars using aqua regia and electrically connected as shown in Fig. 5.1. Angle-dependent magnetoresistance measurements (AdMR) are performed by rotating the magnetic field around the sample. During the rotation in the yz-plane, the longitudinal resistivity is measured in the 4-probe configuration, see Fig. 5.1. The magnetic field pointing in the oop direction ([001]) is defined as 0 degree and the rotation of the applied magnetic field is counter clockwise. The applied magnetic field, 0.7 T, is at least one order of magnitude greater than the coercive field of the deposited LSMO thin films. Hence, the net magnetization can be assumed to be parallel to the applied field direction ($\mathbf{M} \parallel \mathbf{B}$).

For the transport studies, the samples are cooled to liquid helium temperatures without applying a magnetic field. During warming, from 4 to 380 K, the AdMR measurements are performed. The obtained angle-dependent resistivity is fitted with
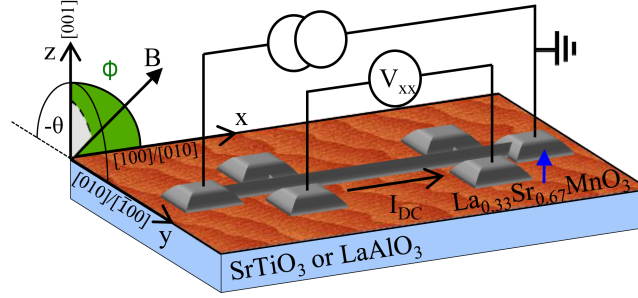
Figure 5.1: *Schematic drawing of the Hall bar with a 4-wire setup to measure the longitudinal resistivity. The crystallographic axes as shown correspond to LSMO, STO and LAO. The AFM image superimposed on the substrate is from the STO substrate with the LSMO film of 15 u.c. deposited on top.*

$$\rho_{long} = \rho_0 + \rho_{2f} \cos\left(2\theta - \delta_{2f}\right) + \rho_{4f} \cos\left(4\theta - \delta_{4f}\right)$$
$$+ \rho_{drift} \exp\left[-(360 + \theta)/\tau_0\right], \tag{5.1}$$

where ρ_0 is the baseline resistivity, ρ_{2f}, and ρ_{4f} are the two- and fourfold resistivities. The δ_{2f} and δ_{4f} are terms which indicate the position of the peak resistivity for the two- and fourfold, respectively. The last term ($\rho_{drift} \exp\left[-(360 + \theta)/\tau_0\right]$) is used to compensate for thermal drift in the resistivity during measurements. Equation 5.1 is based on the AMR energy terms [3, 48]:

$$E = A_0 + A_1 \cos^2(\theta) + A_2 \cos^4(\theta), \tag{5.2}$$

where A_0, A_1 and A_2 are constants and θ is the angle between the current and applied magnetic field.

The fourfold term in Eq. 5.1 and Eq. 5.2 is added to fit secondary phases present in the system. If a system has two distinct easy-axes, the superposition of the two results in a fourfold contribution in the AdMR.

As the base resistivity (ρ_0) varies per sample, the amplitude for the twofold (ρ_{2f}) and fourfold (ρ_{4f}) terms can be compared by expressing the change in AdMR percentage as

$$AdMR\% \overset{\text{def}}{=} \frac{\rho|_{max} - \rho|_{min}}{\rho|_{min}} * 100\% \approx \frac{2\rho_{2f}[2\rho_{4f}]}{\rho_0} * 100\%, \tag{5.3}$$

where the first expression is the anisotropic magnetoresistance, which for conventional bulk LSMO systems results in $\rho|_{max/min}$ at 90°/0°, respectively. The left hand side of Eq. 5.3 can be rewritten into variables used in Eq. 5.1 and results in the right hand part of the equation for the twofold [fourfold] AdMR%.

5.3   Results

Fig. 5.2 shows two resistivity plots for all three samples and shows the resistivity for the low (high) temperature in the left (right) axis. At low temperature for the highly strained sample, see Fig. 5.2 (a) (black squares), the lowest resistivity can be found at 0° and -180°. The negative magnetoresistance of the LSMO causes the lowest resistivity to correspond to the location of the magnetic easy-axis. Upon increasing the temperature to 180 K the $\cos(2\theta)$ signal changes sign, peaking at 0° and 180°, indicating that the magnetic easy-axis orients along the ip direction at 180 K.

For the sample which is 0.9% compressively strained, shown in Fig. 5.2 (b), four peaks are visible at 4 K. The big peaks can be fitted with $\cos(2\theta)$ of Eq. 5.1 and the smaller peaks, which peak at 90° and -90°, are fitted with the secondary phase $\cos(4\theta)$ part of Eq. 5.1. Upon increasing the temperature to 195 K, the signal is transformed into a pure $\cos(2\theta)$ signal, see Fig. 5.2 (b) (green circles). The two components can be explained as a superposition of two magnetic easy-axes, resulting in a fourfold contribution in the AdMR signal[49]. The easier of the two magnetization directions will have the strongest lowering in the resistivity. The position of the magnetic easy-axes are extracted from the angular resistance change using both four-fold and two-fold contributions. For the lowest strained sample (Fig. 5.2 (c)), with -0.7% oop strain, the resistivity always peaks at 0° and -180° for all temperatures, corresponding to an ip magnetic anisotropy.

In the supplementary information, resistivity plots at different temperatures are shown in Figs. 5.7, 5.8, and 5.9. The data is fitted with Eq. 5.1 and the extracted parameters are plotted in Fig. 5.3. Fig. 5.3 (a) portrays the fitted two-fold signal. Fig. 5.3 (b) shows ρ_0 versus T, measured under the application of a magnetic field. The metal-to-insulator transition point ($T_{mit} = \delta\rho/\delta T|_{max}$) decreases with increasing strain, indicating a lowering of the Curie temperature with increasing strain.

Based on our earlier work and that of others[12, 14, 50], we estimate the Curie temperatures of the samples to correspond closely to the peak in AdMR%. This results in Curie temperatures of 265 K, 180 K, and 130 K for the -0.7%, 0.9% and 1.9% strain samples, respectively. The highest strained sample (1.9%) shows a negative AdMR at low temperatures. When fitting the signal below 80 K the constraints imposed by the fitting terms considered in equations 1 and 2 are evident, with the
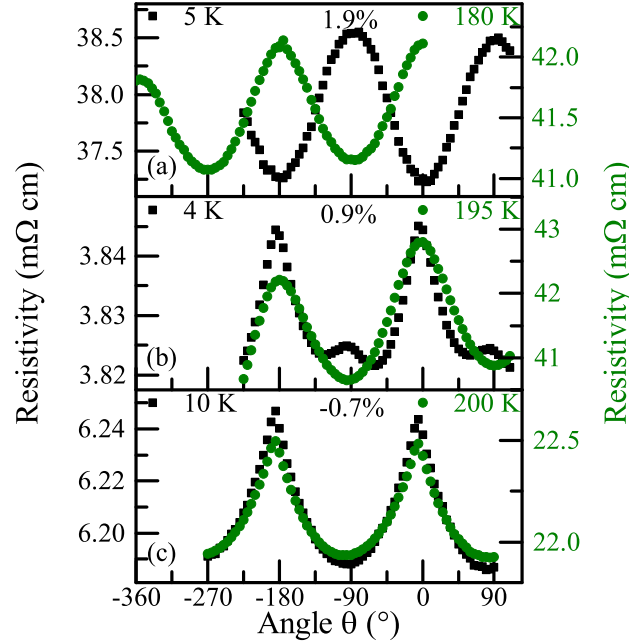
Figure 5.2: *Angle-dependent magnetoresistance results for the three samples with 1.9%, 0.9%, and -0.7% oop strain. The left axis (black squares) shows the resistivity measured at low temperatures (5, 4 and 10 K). The right axis (green dots) shows the resistivity measured at high temperatures (180 K, 195 K, and 200 K).*

best fitting obtained with -A cos (2θ). These indicate that at low temperatures the anisotropy transitions to an oop direction for this film.

In table 5.1 all important features of the three films are summarized, showing the clear dependence with strain.

OOP strain	1.9%	0.9%	-0.7%
Thickness	5.5 nm	5.5 nm	5.7 nm
Thickness	14 u.c.	14 u.c.	15 u.c.
AMR peak temperature	130 K	180 K	265 K
OOP anisotropy temperature	80 K	50 K	0 K
T_{MIT}	150 K	180 K	290 K
OOP AdMR% at 25 K	3.6%	0.3%	0%

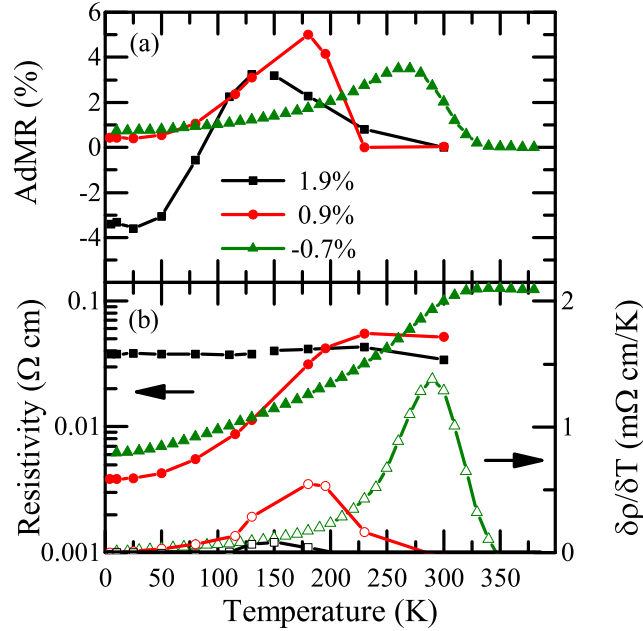**Table 5.1**: *Summary of investigated thin films characteristics*

Figure 5.3: *Extracted parameters from fitting the AdMR curves. (a) Two-fold angle dependent magnetoresistance of all three samples expressed in AdMR% varying with temperature. (b) Extracted ρ_0 resistivity of the samples (solid symbols) on the left side and the derivative of the resistivity ($\delta\rho_0/\delta T$) on the right axis (open symbols).*

What we thus see is that the primary ρ_{2f} contribution, ascribed to either oop or ip anisotropy depends on strain and/or temperature. We discuss this next for the film with the highest strain and where this response is most prominent. This is shown in Fig. 5.4. This figure depicts the influence of the varying magnetic fields (10 mT to 500 mT) on the AdMR for the 1.9 % strained film at 10 K. The measurements were performed in the xz-plane with 0 degree being the oop direction.

5.4 Discussion

As mentioned in the introduction, surface sensitive techniques have already shown magnetic mazelike patterns (with MFM[19]), indicating a partial oop anisotropy in thin LSMO films. The difference between earlier reports and the significance of our work lies in the revelation of a full perpendicular magnetic anisotropy as demon-
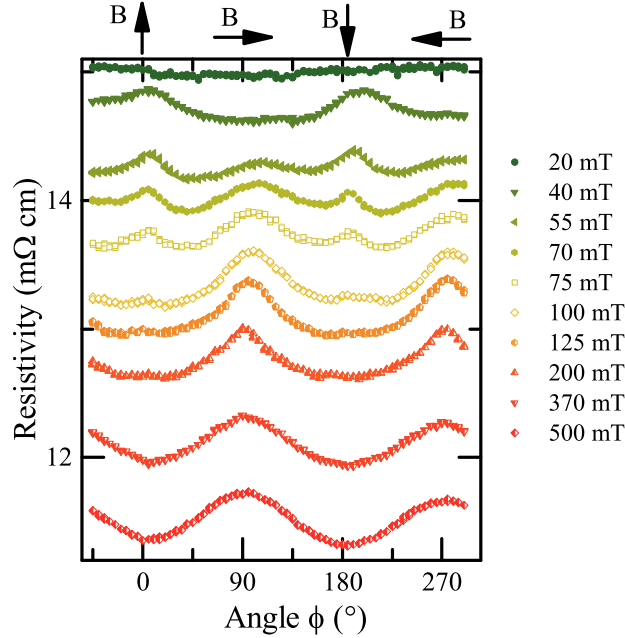
Figure 5.4: *Field dependence at 10 K of the AdMR of the high strain (1.9%)*
sample. The measurements are performed in the xz-plane, with 0 de-
grees being the oop direction.

strated in the magnetotransport studies in our samples. We explain this manifesta-
tion to have its origin in the magnitude of the applied magnetic field. For our stud-
ies, a magnetic field several times larger than the coercive field is used. Performing
the AdMR measurements with a smaller magnetic field as used in MFM studies,
yields a lower signal (see Fig. 5.4 and 5.10). Secondly, as shown in Fig. 5.4, a smaller
magnetic field (below the coercive field) shows an ip magnetization, with resistivity
dips at 90° and -90°. Further we note that we observe a change in peak resistivity
with increasing magnetic field due to the measurement preparation, in which we
cool from room temperature down to 10 K. While cooling down, the spins prefer
to align ip. Decreasing the temperature further will result in a change of the mag-
netocrystalline anisotropy, reorienting the magnetically easier axis in the oop direc-
tion. However, the orientation of the spins are not necessarily altered, possibly due
to a lack of thermal excitation. Performing AdMR measurements at magnetic fields
below the coercive field values will not result in significant changes of the spin ori-
entation resulting in an in-plane anisotropy. This is evident in the gradual increase

and decrease of the oop and ip peaks with increasing applied magnetic field. As the highest applied field is below the saturation magnetization field (see Fig. 5.11 for M-H), we correlate the sign change to an increasing number of magnetic domains following the applied magnetic field upon increasing the applied magnetic field.

We attribute the change in magnetic easy axis to the change in magnetocrystalline anisotropy (MCA). By varying the oop strain we vary the size of the unit cell and observe a change in the oop anisotropy in the system, similar to the earlier observations reported in literature [49]. Elongating LSMO's unit cell along the c axis results in a tetragonal unit cell, with the principal axis along the elongated direction. The tetragonal LSMO unit cell is known to have the easy axis along the elongated direction[16, 51, 52]. The AdMR scaling w.r.t. ip component shows that the temperature at which the maximum AdMR is reached decreases with increasing oop strain. This is inline with the MCA theory, suggesting that the inplane anisotropy decreases upon compressively straining the thin films.

5.5 Conclusion

To conclude, we report on the observation of perpendicular magnetic anisotropy in compressively strained thin films of LSMO by measuring angle dependent magnetoresistance. The observed anisotropy is measured for three films with different strain and at various temperatures. The temperature dependence of the 1.9% oop strained thin film shows a change of the magnetic easy axis from the oop to the ip direction at 80 K.

Based on the obtained data for the OOP anisotropy energy vs strain, we show a qualitative reinforcement of the general understanding between the elongation of a unit cell and the alteration of the magnetic easy axis towards the elongated direction. Our results also heralds possibilities for asymmetrically straining the unit cell, suggesting the creation of multiple easy axes in different directions, in thin films of LSMO. This is particularly relevant for creating multi-state memory bits for unconventional computing applications.

References

[1] X. G. Chen, J. B. Yang, Y. B. Yang, C. S. Wang, S. Q. Liu, Y. Zhang, J. Z. Han, and Y. C. Yang, J. Appl. Phys. **115**, 043904 (2014).

[2] W. Thomson, Proc. R. Soc. Lond. **8**, 546 (1857).

[3] T. McGuire and R. Potter, IEEE Trans. Magn. **11**, 1018 (1975).

[4] Y. Tokura and Y. Tomioka, J. Magn. Magn. Mater. **200**, 1 (1999).

[5] M. Baldini, T. Muramatsu, M. Sherafati, H.-K. Mao, L. Malavasi, P. Postorino, S. Satpathy, and V. V. Struzhkin, Proc. Natl. Acad. Sci. U.S.A. **112**, 10869 (2015).

[6] S. L. Yuan, Z. Y. Li, W. Y. Zhao, G. Li, Y. Jiang, X. Y. Zeng, Y. P. Yang, G. Q. Zhang, F. Tu, C. Q. Tang, and S. Z. Jin, Phys. Rev. B **63**, 172415 (2001).

[7] G. Banach, R. Tyer, and W. M. Temmerman, J. Magn. Magn. Mater. **272-276**, 1963 (2004).

[8] J. O'Donnell, J. N. Eckstein, and M. S. Rzchowski, Appl. Phys. Lett. **76**, 218 (2000).

[9] M. Egilmez, K. H. Chow, and J. A. Jung, Mod. Phys. Lett. B **25**, 697 (2011).

[10] H. Sharma, H. Bana, A. Tulapurkar, and C. V. Tomy, Mater. Chem. Phys. **180**, 5 (2016).

[11] P. K. Muduli, G. Singh, R. Sharma, and R. C. Budhani, J. Appl. Phys. **105**, 113910 (2009).

[12] M. Ziese and S. P. Sena, J. Phys.: Condens. Matter **10**, 2727 (1998).

[13] M. Bibes, B. Martinez, J. Fontcuberta, V. Trtik, C. Ferrater, F. Sanchez, M. Varela, R. Hiergeist, and K. Steenbeck, J. Magn. Magn. Mater. **211**, 206 (2000).

[14] J.-B. Yau, X. Hong, A. Posadas, C. H. Ahn, W. Gao, E. Altman, Y. Bason, L. Klein, M. Sidorov, and Z. Krivokapic, J. Appl. Phys. **102**, 103901 (2007).

[15] H. Boschker, M. Mathews, P. Brinks, E. Houwman, A. Vailionis, G. Koster, D. H. A. Blank, and G. Rijnders, J. Magn. Magn. Mater. **323**, 2632 (2011).

[16] K. Steenbeck, T. Habisreuther, C. Dubourdieu, and J. P. Senateur, Appl. Phys. Lett. **80**, 3361 (2002).

[17] Z. Liao, M. Huijben, Z. Zhong, N. Gauquelin, S. Macke, R. J. Green, S. Van Aert, J. Verbeeck, G. Van Tendeloo, K. Held, G. A. Sawatzky, G. Koster, and G. Rijnders, Nat. Mater. **15**, 425 (2016).

[18] H. Boschker, J. Kautz, E. P. Houwman, W. Siemons, M. Huijben, D. H. A. Blank, G. Koster, A. Vailionis, and G. Rijnders, Phys. Rev. Lett. **109** (2012).

[19] J. Dho, Y. N. Kim, Y. S. Hwang, J. C. Kim, and N. H. Hur, Appl. Phys. Lett. **82**, 1434 (2003).

[20] K. H. Ahn, T. Lookman, and A. R. Bishop, Nature **428**, 401 (2004).

[21] W. Y. Cui, P. Li, and H. L. Bai, J. Appl. Phys. **117**, 133904 (2015).

[22] M. Ziese, H. C. Semmelhack, and P. Busch, J. Magn. Magn. Mater. **246**, 327 (2002).

[23] A. Asamitsu and Y. Tokura, Phys. Rev. B **58**, 47 (1998).

[24] T. Bolstad, E. Lysne, U. L. Osterberg, and T. Tybell, J. Magn. Magn. Mater. **487**, 165304 (2019).

[25] C. Zener, Phys. Rev. **82**, 403 (1951).

[26] F. Büttner, I. Lemesh, and G. S. Beach, Sci. Rep. **8**, 1 (2018).

[27] W. Jiang, P. Upadhyaya, W. Zhang, G. Yu, M. B. Jungfleisch, F. Y. Fradin, J. E. Pearson, Y. Tserkovnyak, K. L. Wang, O. Heinonen, S. G. E. t. Velthuis, and A. Hoffmann, Science **349**, 283 (2015).

[28] R. Tomasello, E. Martinez, R. Zivieri, L. Torres, M. Carpentieri, and G. Finocchio, Sci. Rep. **4**, 6784 (2014).

[29] W. Kang, X. Chen, D. Zhu, X. Zhang, Y. Zhou, K. Qiu, Y. Zhang, and W. Zhao, 2018 IEEE 7th Non-Volatile Memory Systems and Applications Symposium, 7 (2018).

[30] I. M. Miron, K. Garello, G. Gaudin, P.-J. Zermatten, M. V. Costache, S. Auffret, S. Bandiera, B. Rodmacq, A. Schuhl, and P. Gambardella, Nature **476**, 189 (2011).

[31] A. Manchon, J. Zelezny, I. M. Miron, T. Jungwirth, J. Sinova, A. Thiaville, K. Garello, and P. Gambardella, Rev. Mod. Phys. **91**, 035004 (2019).

[32] M. Cubukcu, O. Boulle, M. Drouard, K. Garello, C. Onur Avci, I. Mihai Miron, J. Langer, B. Ocker, P. Gambardella, and G. Gaudin, Appl. Phys. Lett. **104**, 042406 (2014).

[33] F. Zhang, B. Wu, G. Zhou, Z.-Y. Quan, and X.-H. Xu, Nanoscale Res. Lett. **13**, 24 (2018).

[34] P. Dey, T. K. Nath, and A. Taraphder, Appl. Phys. Lett. **91**, 012511 (2007).

[35] H. Nishikawa, E. Houwman, H. Boschker, M. Mathews, D. H. A. Blank, and G. Rijnders, Appl. Phys. Lett. **94**, 042502 (2009).

[36] H. Boschker, J. Kautz, E. P. Houwman, G. Koster, D. H. A. Blank, and G. Rijnders, J. Appl. Phys. **108**, 103906 (2010).

[37] C. Kwon, M. C. Robson, K.-C. Kim, J. Y. Gu, S. E. Lofland, S. M. Bhagat, Z. Trajanovic, M. Rajeswari, T. Venkatesan, A. R. Kratz, R. D. Gomez, and R. Ramesh, en, J. Magn. Magn. Mater. **172**, 229 (1997).

[38] I. Benguettat-EL Mokhtari, Y. Roussigne, T. Petrisor, F. Zighem, F. Kail, L. Chahed, V. Pierron, L. Méchin, M. Gabor, and M. Belmeguenai, Phys. Status Solidi B **257**, 2000265.

[39] J. M. Vila-Fungueirino, C. T. Bui, B. Rivas-Murias, E. Winkler, J. Milano, J. Santiso, and F. Rivadulla, J. Phys. D: Appl. Phys. **49**, 315001 (2016).

[40] J. Zhang, A. A. Burema, J. Chen, J. Hu, C. Guo, H. Wang, N. Li, B. Wei, X. Han, T. Banerjee, and H. Yu, Appl. Phys. Lett. **117**, 232402 (2020).

[41] Y. Zhang, J. Liu, Y. Dong, S. Wu, J. Zhang, J. Wang, J. Lu, A. Rückriegel, H. Wang, R. Duine, H. Yu, Z. Luo, K. Shen, and J. Zhang, Phys. Rev. Lett. **127**, 10.1103/PhysRevLett.127.117204, 117204 (2021).

[42] M. Saib, M. Belmeguenai, L. Mechin, D. Bloyet, and S. Flament, J. Appl. Phys. **103**, 113905 (2008).

[43] L. M. Berndt, V. Balbarin, and Y. Suzuki, Appl. Phys. Lett. **77**, 2903 (2000).

[44] A. B. Shick, Phys. Rev. B **60**, 6254 (1999).

[45] J. Dho and N. Hur, J. Magn. Magn. Mater. **318**, 23 (2007).

[46] M. Kawasaki, K. Takahashi, T. Maeda, R. Tsuchiya, M. Shinohara, O. Ishiyama, T. Yonezawa, M. Yoshimoto, and H. Koinuma, Science **266**, 1540 (1994).

[47] G. Koster, B. L. Kropman, G. J. Rijnders, D. H. Blank, and H. Rogalla, Appl. Phys. Lett. **73**, 2920 (1998).

[48] Y. Bason, J. Hoffman, C. H. Ahn, and L. Klein, Phys. Rev. B **79** (2009).

[49] A. A. Burema and T. Banerjee, Appl. Phys. Lett. **119**, 011901 (2021).

[50] A. A. Burema, J. J. L. van Rijn, and T. Banerjee, J. Vac. Sci. Technol. A **37**, 021103 (2019).

[51] Z.-H. Wang, G. Cristiani, H.-U. Habermeier, Z.-R. Zhang, and B.-S. Han, J. Appl. phys. **94**, 5417 (2003).

[52] F. Tsui, M. Smoak, T. Nath, and C. Eom, Appl. Phys. Lett. **76**, 2421 (2000).
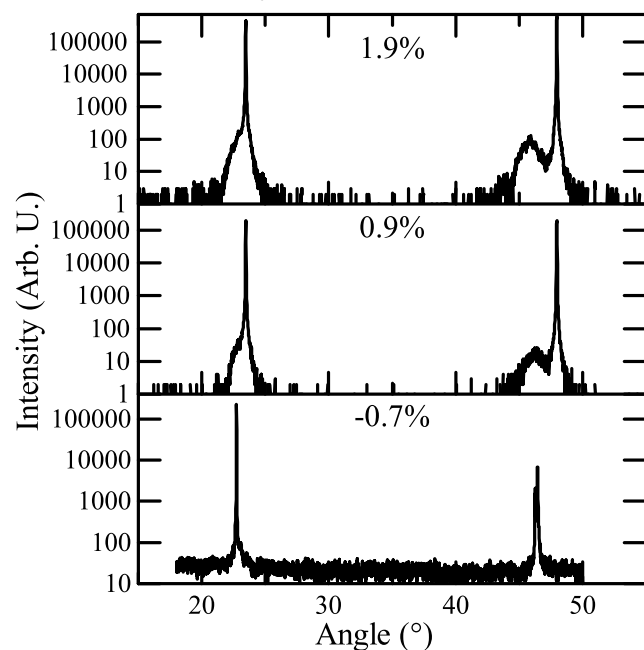
Supplementary Information

Figure 5.5: XRD θ-2θ scan of all three samples. (Part of) the dataset presented in the top and middle window appeared in [1] and [2], respectively.
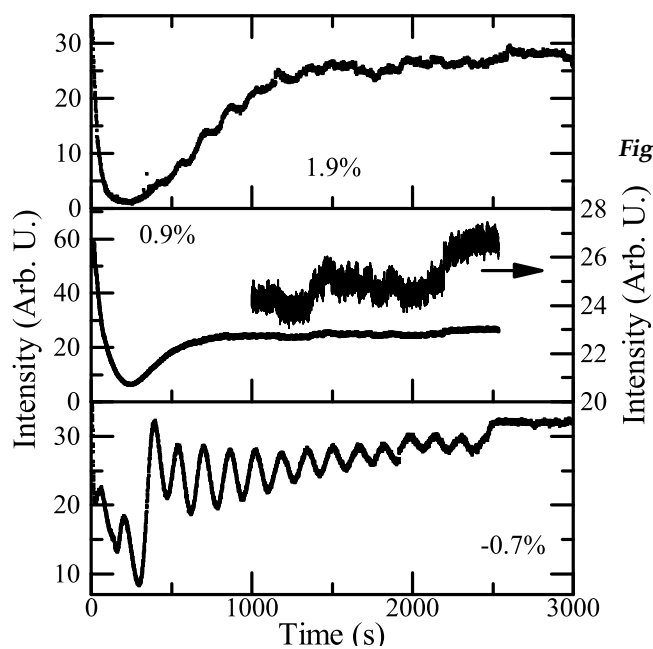

Figure 5.6: RHEED of all three samples. (Part of) the dataset presented in the top and middle window appeared in [1] and [2], respectively.
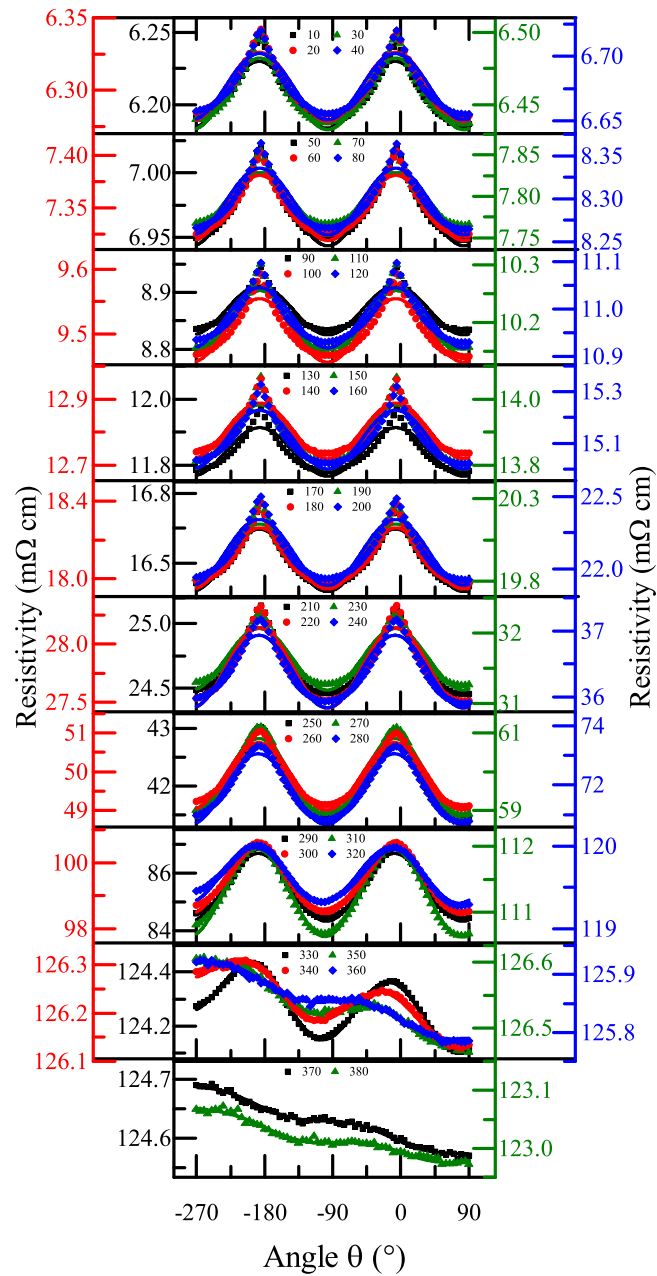
Figure 5.7: *Plotted are the angle dependent resistivity curves of the -0.7% strained sample. All measured temperatures are depicted as measured. The color of the axes correspond to the color of the graph, for black & white the axes correspond to the circle, square, triangle, diamond data (f.l.t.r.). Solid lines are the fit with Eq. 1.*

Figure 5.8: *Plotted are the angle dependent resistivity curves of the 0.9% strained sample. All measured temperatures are depicted as measured. The black squares correspond to the left axis and the circles correspond to the right axis. Solid lines are the fit with Eq. 1.*
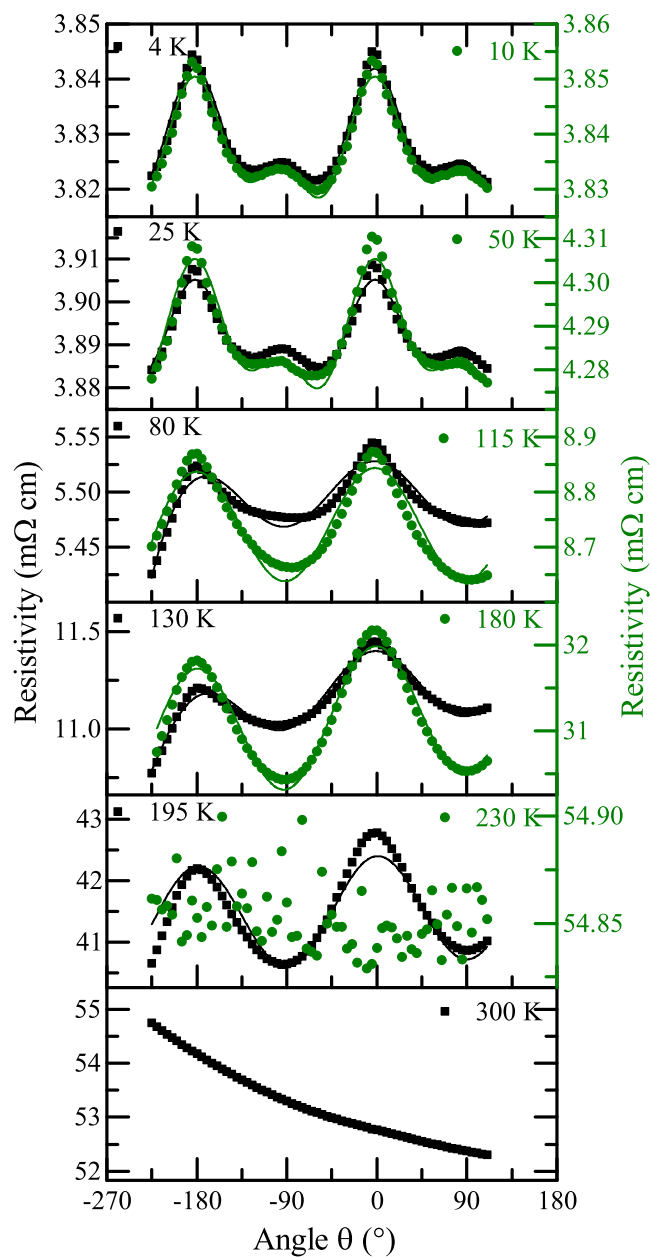
Figure 5.9: *Plotted are the angle dependent resistivity curves of the 1.9% strained sample. All measured temperatures are depicted as measured. The black squares correspond to the left axis and the circles correspond to the right axis. Solid lines are the fit with Eq. 1.*
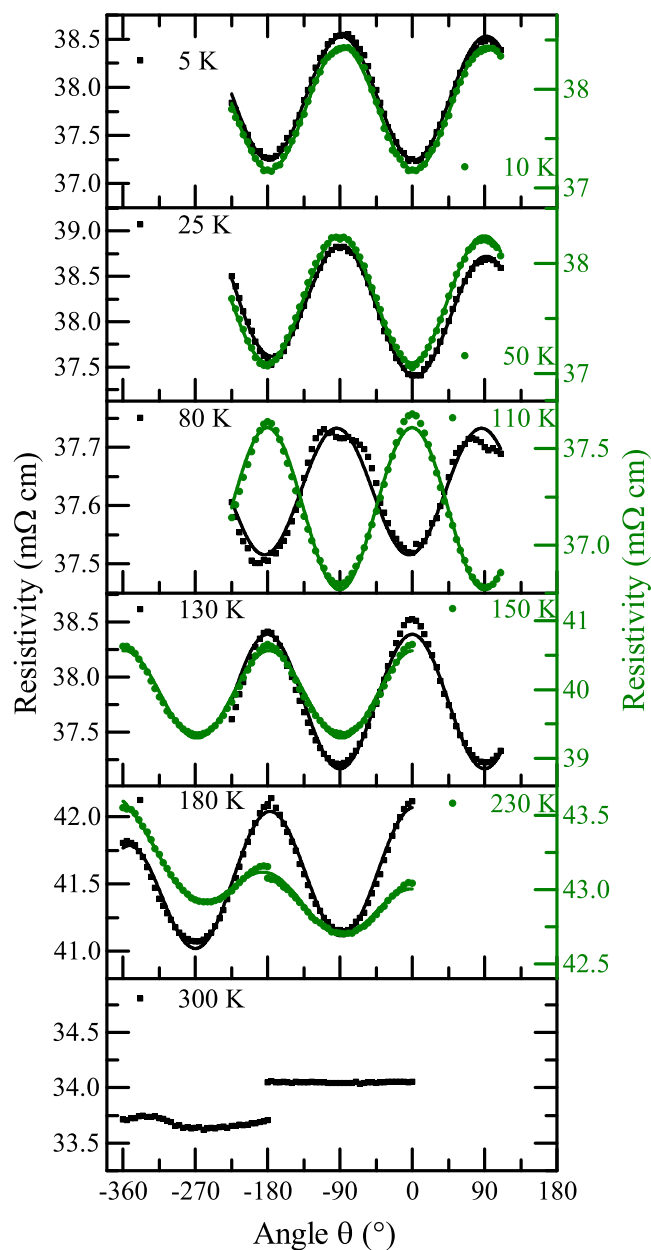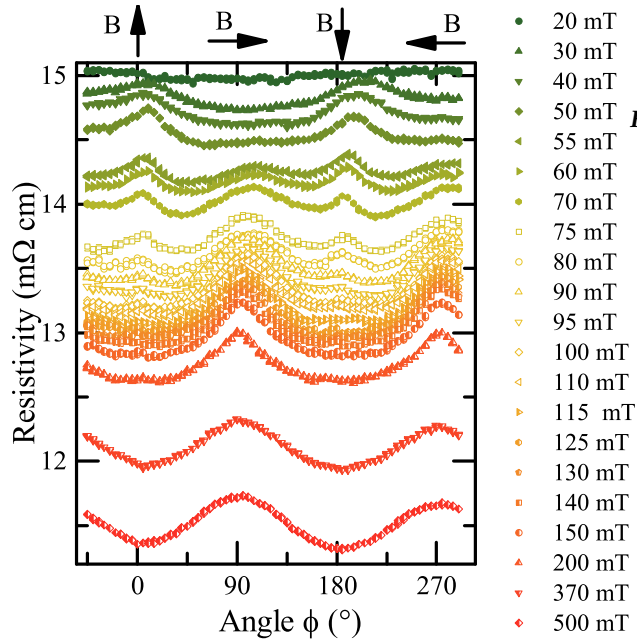
Figure 5.10: *Field dependence at 10 K of the AdMR of the high strain (1.9%) sample. The measurements are performed with increasing applied magnetic field in the xz-plane, with 0 degrees being the oop direction.*

Figure 5.11: *Adapted figure from [1]. The magnetization versus applied magnetic field of 1.9% strained sample at 10 K.*

References

[1] A. A. Burema, J. J. L. van Rijn, and T. Banerjee, J. Vac. Sci. Technol. A **37**, 021103 (2019).

[2] A. A. Burema and T. Banerjee, Appl. Phys. Lett. **119**, 011901 (2021).

Samenvatting

In de afgelopen decennia hebben elektronische apparaten zich in verscheidende aspecten van ons dagelijks leven doordrongen. Dit resulteerde in meer controle over, en ve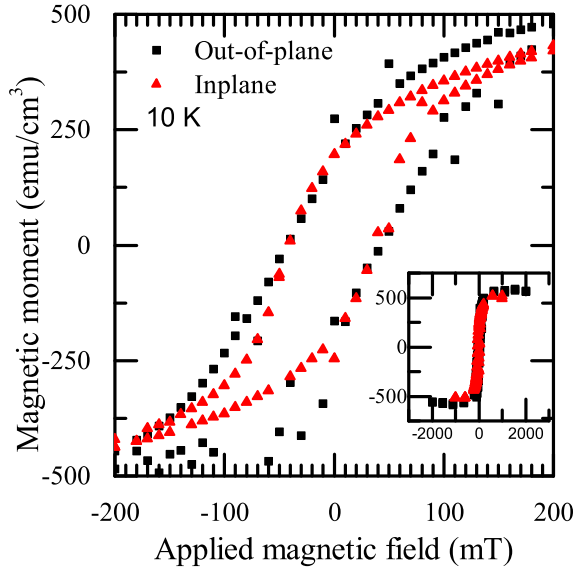rbeteringen van, onze omgeving. Ontwikkelingen in onder andere de halfgeleiderindustrie hebben deze ontwikkeling mogelijk gemaakt door het verbeteren van elektronische apparaten. Deze verbetering is grotendeels te danken aan de verkleining van de omvang van transistoren en dataopslag. Dataopslag bestaat uit een verzameling van magnetische bits en de grootte van deze bits is in de afgelopen decennia met een factor 10^9 verkleind. De verkleining is deels te danken aan de ontwikkelingen binnen het onderzoeksveld van de spintronica, waardoor de huidige grootte van een magnetische bit uit slechts enkele magnetische domeinen bestaat. De bitgrootte is nu zo klein dat conventionele verkleining steeds moeilijker wordt. Voor verdere verkleining van magnetische bits, of beter gezegd het verhogen van de data dichtheid per cm^2, wordt gekeken naar andere manieren van geheugenopslag.

Een veelbelovende nieuwe opslagmethoden is de *(skyrmion) racetrack memory*. De twee grootste voordelen van dit type geheugen over bestaande varianten zijn alleerst de mogelijkheid om een hoge datadichtheid te generen en ten tweede het ontbreken van bewegende delen. Daarnaast heeft het gebruik van skyrmionen in tegenstelling tot magnetische domeinen ook andere voordelen. Zo is voorspeld dat een skyrmion energetisch stabieler is dan een magnetisch domein waardoor verlies van informatie minder waarschijnlijk is. Daarnaast kunnen skyrmionen makkelijker gestuurd worden met stroom of magnonen. Ook de topologische bescherming bied voordelen, deze zorgt ervoor dat skyrmionen minder aan magnetische afwijkingen blijven plakken, wat het gecontroleerd creëren, sturen en annihileren van skyrmionen makkelijker maakt.

Voor een hoge bitdichtheid geven we de voorkeur aan een systeem met een dunne magnetische laag. De dunne laag heeft tevens als voordeel dat een symmetriebreking op het raakvlak resulteert in een raakvlak Dzyaloshinskii–Moriya in-

teractie die de stabiliteit van skyrmionen verbeterdt. Des te dunner de laag is, des te dominanter het raakvlakeffect op de energietermen. Wij hebben het materiaal $La_{0.67}Sr_{0.33}MnO_3$ (LSMO) onderzocht en gekeken welke veranderingen we konden aanbrengen aan het materiaal zodat skyrmionen in het materiaal kunnen verblijven. In hoofdstuk 3 van deze thesis hebben we de magnetische en elektronische eigenschappen van in het platte vlak samengeperst LSMO gegroeid op $LaAlO_3$ onderzocht. Opmerkelijk was de observatie van twee temperatuurafhankelijke magnetische fases onder de Curie temperatuur. Dit, in tegenstelling tot de enkele magnetische fase in bulk LSMO, laat zien dat de magnetisch kristallijne anisotropie (MKA) gestuurd kan worden door fysieke spanning uit te oefenen op het materiaal. De extra magnetische fase beneden 130 K is waarschijnlijk een coëxistentie van twee fasen gestabiliseerd onder invloed van een zwak magnetisch veld (tot 50 mT). Naast de magnetische data lieten ook de ladingtransport experimenten zien dat er twee temperatuurafhankelijke toestanden zijn, exemplarisch voor de sterke connectie tussen magnetisme en lading transport in LSMO.

Om skyrmionen te creëren en stabiliseren in LSMO, is een goede controle over de effectieve MKA nodig. Om de optimale balans van krachten voor de stabilisatie van skyrmionen te vinden zoeken we een optimale dikte van de dunne laag om de energietermen het best te kunnen bestuderen. Hoofdstuk 4 gaat over de dikteafhankelijkheid van de effectieve MKA in samengeperst LSMO gegroeid op $LaAlO_3$. Door weerstandfluctuaties te meten in de dunne laag terwijl deze wordt geroteerd in een constant magneetveld kan de MKA worden bestudeerd. Voor de dikteafhankelijkheid hebben we de weerstandfluctuaties van rotaties in het platte vlak bestudeerd. Uit de resultaten bleek dat de MKA vooral zichtbaar is op lage temperaturen gekenmerkt door een draaisymmetrie van $90°$ ($\cos(4\theta)$). Door het verhogen van de temperatuur verlaagt de symmetrie van de weerstandfluctuaties naar een draaisymmetrie van $180°$ ($\cos(2\theta)$). Verdere verhoging van de temperatuur tot boven de Curie temperatuur leid tot het verdwijnen van enige vorm van symmetrie. Uit de dikteafhankelijke resultaten bleek dat een dunne laag van 14 u.c. de ideale dikte was om de MKA te bestuderen.

Daarom hebben we meerdere dunne lagen LSMO met een dikte van ongeveer 14 u.c. gegroeid met een verschillende mate van kristaldeformatie. In deze lagen kunnen we de effectieve MKA-afhankelijkheid van kristaldeformaties door samenpersing onderzoeken. Dit onderzoek hebben we gedaan door de lagen één voor één te roteren in een magneetveld en de weerstandfluctuaties te meten bij een gelijkstroom van 5 μA. De rotatie draait het sample uit het platte vlak zodat de loodrechte magnetische anisotropie (LMA) gemeten kan worden. In het sample met de groot-

ste LSMO kristaldeformatie (1.8%) is de LMA zichtbaar van 10 K tot 80 K. Uit de resultaten blijkt dat een deformatie van de kristalstructuur bevorderlijk is voor de LMA.

De resultaten gepresenteerd in deze thesis versterken het algemene beeld over hoe LSMO zich gedraagt onder kristaldeformaties door samendrukking. De dunne lagen laten het belang van de MKA als variabele parameter zien om de gewenste anisotropie in een LSMO te creëren.

Summary

In the last decades, electronic devices have spread across every aspect of our lives, improving the quality of life and control over our environment. Developments in, among others, the semiconductor industry have made this possible by increasing the performance of electronic devices. This is largely contributed to the continued down-scaling in transistors size roughly resulting in the doubling of the number of transistors per square meter every two years, which is known as Moore's law. Not only transistors but also logic memory has decreased in size, in part due to the developments in the field of spintronics, which utilizes the spin of the electron as well as electron charge. The down-scaling of stable magnetic domains reached a point where only a few magnetic domains of several nanometers are still present in the area where a logic bit is stored.

Increasing the logic density is increasingly difficult while utilizing the down-scaling approach. Therefore other options like the re-engineering of the magnetic memory is one of the proposed options. A candidate for improved memory is the skyrmion racetrack memory. Utilizing the topological protection of a skyrmion is an advantage in multiple aspects of the design. Firstly, a skyrmion is predicted to be more energetically stable, per unit of volume, compared to a single domain counterpart. Secondly, skyrmions can be moved with low charge current densities or spin currents. Thirdly, due to their topological protection, skyrmions naturally repel each other and steer clear of magnetic defects.

To use skyrmions in an application, the material hosting the skyrmion must be thin, as we want a high-density magnetic logic system. An added advantage of a thin film is the intrinsic symmetry breaking which generates an interfacial Dzyaloshinskii–Moriya interaction, which can be used for stabilizing skyrmions. We investigated the properties of $La_{0.67}Sr_{0.33}MnO_3$ (LSMO) to see if the material can be made to house skyrmions at room temperature.

To expand our knowledge with regards to to stabilize skyrmions in LSMO, we investigated the magneotransport properties of LSMO. In chapter 3 we report our findings with respect to the magnetic and electronic properties of a compressively

strained thin film of LSMO grown on $LaAlO_3$ (LAO). An interesting finding is the observation of two magnetic phases below Curie temperature compared to one phase in bulk LSMO, which indicates that LSMO's magnetic anisotropy can be fine-tuned. The phase present below 130 K is believed to be a coexistence of two phases at low magnetic fields (up to 50 mT). We observed the second phase not only in the magnetic but also the charge transport experiments, showing the strong connection between magnetism and charge transport in LSMO.

To stabilize skyrmions we need to fine tune the MCA with strain. Therefore, we investigated the ideal thickness to observe the MCA in chapter 4, in which we perform magnetotransport measurements utilizing the double exchange mechanism to study the thickness dependence of the MCA in compressively strained thin films of LSMO. we report on strain-engineered $La_{0.67}Sr_{0.33}MnO_3$ thin films grown on $LaAlO_3$ which show different angle-dependent magnetoresistance properties compared to their bulk analogs. Upon increasing temperature, a symmetry change from four-fold ($\cos(4\theta)$) to two-fold ($\cos(2\theta)$) is observed in the angle-dependent resistance measurements. By increasing the temperature we observe three distinct temperature-dependent phases. The four-fold symmetric signal originates from magnetocrystalline anisotropy, whereas the two-fold symmetric signal is believed to be the conventional anisotropic magnetoresistance.

Based on the temperature-dependent observations, we conclude that the MCA is dominant at low temperatures. Increasing the temperature results in a reduced effective anisotropy due to an increased thermal energy, which will result in a disappearance of the effective anisotropy at the Curie temperature. Secondly, we found that decreasing the thickness increased the MCA, which we connect to the decrease in conductivity which results in an increase in hopping energy. The increase in hopping energy allows us to better observe the MCA energy difference between a magnetic easy and hard axes.

In the last chapter, we grew several films of 14 and 15 u.c. as we found this thickness to be the optimal to observe changes in the MCA. In these samples the perpendicular magnetic anisotropy of LSMO is investigated while varying the strain in order to find the ideal balance of energy terms for skyrmions. Once again we utilize magnetotransport properties to investigate the out-of-plane anisotropy at various temperatures. In a similar fashion to the in-plane rotation, we rotated a constant magnetic field around the Hall bar in the yz-plane, while applying a direct current of 5 μA in the x-direction. The results indicate a positive correlation between the out-of-plane (oop) crystallographic strain and the presence of perpendicular magnetic anisotropy (PMA). A larger oop crystallographic strain resulted in the observation

of PMA at higher temperatures. For the highest (1.8%) oop strained Hall bar, a transition from PMA to an in-plane easy-axis was observed at 80 K. To increase the transition temperature at which the magnetic axis falls back in-plane, an increase in oop strain utilizing a different substrate is necessary.

Our results qualitatively reinforce the general understanding of the behavior of doped manganites, by systematically studying the temperature dependence of the anisotropy via magnetotransport measurements. The studied samples in this thesis highlight the utility of the effective magnetocrystalline anisotropy as a tool to control the desired anisotropy in crystalline thin films of $La_{0.67}Sr_{0.33}MnO_3$.

Acknowledgements

The acknowledgment section is probably the most read part of a thesis, or at least I tend to read this section to see who contributed or made a lasting impression during the four years of being a Ph.D. candidate. Now reaching the end myself, I realized that writing the acknowledgments is difficult. Therefore I like to keep it short and do my best to thank everybody in person. First of all, I want to thank my family for their unwavering support and guidance throughout my entire education. They made me the person I am today and cheered me up when times were tough. Without them, this endeavor would not have been possible. I realize how fortunate I am with you all around me.

Besides my family, there are plenty of colleagues to thank. Starting with my supervisor *Tamalika Banerjee*. I am grateful for the opportunities to collaborate with others and perform the research presented in this thesis. I hope that many exciting breakthroughs for you may follow. Though we did not observe skyrmions in LSMO, I think we came a long way. Hopefully someday skyrmions will be observed in LSMO with the help of our work.

Maxim Mostovoy, thank you for being my co-promotor and the discussions we had during skyrmion meetings. Your questions and suggestions motivated me to push forward and investigate from multiple angles to exclude other theories and hypotheses.

Furthermore, I would like to thank the reading committee for giving usefull feedback on my thesis. Prof. J. Santamaria Sánchez-Barriga, Prof. A.J.H.M. Rijnders, and Prof. B.J. van Wees your suggestions and warm words are really appreciated.

Graeme R. Blake thank you for guiding me during my master's and part of my Ph.D., you taught me the value and principles of solid science and dedication. The patience with which you listened to all my ideas and taking them for a positive spin to help me forward is remarkable. The time we collaborated was a true pleasure from my side, and I thank you for your guidance throughout these years. I wish you all the best.

Furthermore, I like to thank *Mallikarjuna Gurram* for his guidance in the last part

of my Ph.D. track. It is always good to have feedback from somebody that is somewhat out of your field of expertise to keep the scientific research and knowledge relevant for a larger audience.

I have supervised several students: *Job J.L. van Rijn, Bart Zillen, Jip van Ham, Andrei Frantiu, and Hugo Potgieter* a big thanks for the fun times and the questions/ scientific discussions we had. The passion and dedication you all have shown for your research topic is remarkable. Listening to and discussing all the new ideas and theories you had, taught me a lot and was a true pleasure. All the best with your future careers.

Last but not least, I like to thank the entire FND group for all the fun times we had together. *Alexey, Anna, Arijit, Arjun, Azminul, Bart van Wees, Boxuan, Carmem, Christian, Eswar, Frank, Freddie, Geert, Gert-Jan, Hans, Jakko, Jantje, Jing, Job, Johan Holstein, Joop, Juan, Julian, Kumar, Lei, Ludo, Marcos Guimaraes, Nienke, Obed, Pep, Ping, Rafael, Roald, Sander, Si (Crystal), Sytze, Talieh, Tian, Tom Schouten, Xiangyang, and Xu*: it was a true pleasure to work with you all. In particular, I would like to thank *Eric* for guiding me during my Bachelor and Master thesis. You have been a great mentor. Thank you for your advice and guidance during the start of my career. *Martijn*, I hope you are happy in Norway. You are truly missed in the Groningen nightlife. *Siddharta* it was always fun to talk to you. I hope you find a new squash buddy in Veldhoven. *Anouk, Dennis, Feitze, Jan, Sanne, Silvia* and *Tom Bosma*, it is nice to have good colleagues, but being friends as well makes the work experience way better. All the best to you, and I hope to keep seeing you regularly.

<div align="right">

Arjan A. Burema
Groningen
August 31, 2021

</div>

Curriculum Vitae

Arjan Auke Burema

17th of March 1994   Born in Hoogeveen, The Netherlands

Education

2017 - 2021   Ph.D. research in the group of Spintronics of Functional Materials,
at the Zernike Institute for Advanced Materials,
University of Groningen, the Netherlands,
under the supervision of Prof. Dr. T. Banerjee. Research project:
"*Angle-dependent magnetoresistance in epitaxially strain-engineered thin films.*"

2015 - 2015   Master of Science, Top Master Programme in Nanoscience
at the University of Groningen
Thesis in the group of Prof. Dr. T. Banerjee. Research project:
"*Electronic characterization of an Au/Bi$_2$Se$_3$ interface*"

2012 - 2015   Bachelor of Science, Bachelor Physics at the University of Groningen

List of Publications

A.A. Burema, **T. Banerjee**, *Temperature-dependent periodicity halving of the in-plane angular in La0.67Sr0.33MnO3 thin films on LaAlO3*, Appl. Phys. Lett. 119 (2021)

J. Zhang*, A.A. Burema*, J. Chen*, J. Hu, C. Guo, H. Wang, N. Li, B. Wei, X. Han, T. Banerjee, and H. Yu, *Surface anisotropy induced spin wave nonreciprocity in epitaxial LSMO film on SrTiO3 substrate*, Appl. Phys. Lett. 117 (2020) (*equal contribution)

P-Y Pichon, P Berneron, J Levinsky, A. A. Burema, G. R. Blake, D. Berthebaud, S. Gascoin, F. Gascoin, S. Hebert, J. Amtsfeld, T. Hommels, M. Huijben, J. de Boor, E. Müller, C. Navone, and A. Schönecker, *Stability and thermoelectric performance of doped higher manganese silicide materials solidified by RGS (ribbon growth on substrate) synthesis* J. Alloys Compd. 832 (2020)

A.A. Burema*, J.J.L. van Rijn*, and T. Banerjee, *Temperature dependence of the magnetization of La0.67Sr0.33MnO3 thin films on LaAlO3*, J. Vac. Sci. Technol. 37 (2019) (*equal contribution)

A.A. Burema, J.J.L. van Rijn, and T. Banerjee, *Temperature-dependent out-of-plane anisotropy in compressively strained $La_{0.67}Sr_{0.33}MnO_3$ thin films*, manuscript under review by J. Magn. Magn. Mater